Die approbierte Originalversion dieser Dissertation ist an der Hauptbibliothek der Technischen Universität Wien aufgestellt (http://www.ub.tuwien.ac.at).

The approved original version of this thesis is available at the main library of the Vienna University of Technology (http://www.ub.tuwien.ac.at/englweb/).

DISSERTATION

Methods of Multi Nuclear Magnetic Resonance Spectroscopy for Metabolic Research

ausgeführt zum Zwecke der Erlangung des akademischen Grades des Doktors der technischen Wissenschaften unter der Leitung von

Univ. Prof. Dipl. Ing. Dr. Gerald Badurek

E 141, Atominstitut der Österreichischen Universitäten

und

Univ. Prof. Dipl. Ing. Dr. Ewald Moser

Medizinische Universität Wien, Zentrum für Biomedizinische Technik und Physik

eingereicht an der

Technischen Universität Wien

Fakultät für Physik

von

Albrecht I. Schmid

Martrikelnummer: 9325064

Paletzgasse 22-24/35, 1160 Wien

Wien am 10.9.2007

Zusammenfassung

Kernspinresonanz (NMR[1]) ist ein etabliertes Analyseverfahren zur Untersuchung verschiedenster Materialien, insbesondere zur Untersuchung von organischen Substanzen und Geweben. In-vivo NMR Spektroskopie hat in den letzten Jahrzehnten immer mehr an Bedeutung gewonnen. Dabei ist Protonenspektroskopie das am häufigsten verwendete Verfahren. Protonen haben das größte gyromagnetische Verhältnis und sind reichlich in allen Geweben und Organen vorhanden.

Für die Untersuchung des Energiestoffwechsels sind jedoch andere Isotope, insbesondere ^{31}P und ^{13}C von mindestens gleich großer Bedeutung. Dabei erlaubt Phosphorspektroskopie die quantitative Bestimmung der energiereichen Phosphate wie Adenosintriphosphat (ATP) oder Kreatinphosphat (PCr). ^{13}C-Spektroskopie hingegen ermöglicht die Anwendung isotopenangereicherter Substrate, deren Verstoffwechselung verfolgt werden kann.

Die vorliegende Arbeit besteht aus drei Teilen. Der erste Teil enthält eine Zusammenfassung des notwendigen technischen Hintergrunds und erläutert die Motivation für die im Weiteren beschriebenen Experimente aus physiologischer Sicht.

Nach einer Einführung in die Grundlagen der Kernspinresonanz folgt ein Kapitel über Radiofrequenzpulse, insbesondere über B_1-unabhängige, sogenannte adiabatische Pulse. Das nächste Kapitel gibt einen Überblick über die Relevanz der Multikernspektroskopie für die physiologische Forschung. Diese stellt eine einzigartige Möglichkeit zur nichtinvasiven Beobachtung des menschlichen Stoffwechsels dar. Die zentralen Elemente im Verständnis unserer Energieversorgung sind die Bestimmung der Aktivität des Zitronensäurezyklus (TCA-Zyklus) und der Rate der oxidativen Phosphorilierung. Der erste Teil wird mit der Beschreibung des experimentellen Aufbaus abgeschlossen.

Das Ziel des zweiten Teils ist es, zu untersuchen, wie man die Messung des schwachen ^{13}C-Signals mittels spektraler Aufbereitung[2] verbessern kann. Es gibt zahlreiche etablierte Verfahren der hochauflösenden in-vitro Kernspinresonanzspektroskopie, welche routinemäßig in der analytischen Chemie eingesetzt werden. Es stellt sich nun die Frage, in welchem Ausmaßdiese Verfahren für die in-vivo Messung am Menschen, wo die experimentellen Bedingungen schwieriger sind und technische Begerenzungen sowie Sicherheitsregelungen eingehalten werden müssen. Insbesondere sind die verfügbaren Spitzen- und anwendbaren Gesamtleistungen der Radiofrequenzpulse pro Zeiteinheit stark begrenzt. Eine andere Herausforderung stellt die inhomogene Feldverteilung von Oberflächenspulen dar. Diese Radiofrequenzspulen werden wegen ihrer hohen Empfindlichkeit, ihrer Einfachheit und ihrer Flexibiltät gerne eingesetzt.

[1] nuclear magnetic resonance
[2] spectral editing

Das Experiment, welches in Kapitel 7 vorgestellt wird, ist die Implementierung des refokusierten INEPT Experiments mittels B_1-unempfindlicher Radiofrequenzpulse. Der Vorteil dieser Messsequenz gegenüber direkter Messung des ^{13}C-Signals ist nicht nur der Gewinn an Signalstärke, sondern auch eine dramatische Verbesserung der Lokalisierungsmöglichkeiten, da die Protonenmagnetisierung dazu verwendet werden kann. Des Weiteren ist die T_1 Zeit der Protonen kürzer und es entfällt die Ungenauigkeit durch den schwer quantitativ messbaren Overhausereffekt.

Glutamatbestimmung im Zuge der selektiven Isotopenanreicherung durch Verstoffwechselung von ^{13}C isotopenmarkierten Substraten ist der Schlüssel zur Bestimmung der TCA-Zyklusaktivität. Mittels des vorgestellten vollständig adiabatischen refokusierten INEPT-Experiments sollte das Glutamatsignal wesentlich besser quantifiziert werden können.

Der dritte Teil dieser Arbeit konzentriert sich auf die Bestimmung der oxidativen Phosphorilierung in Form von ATP Synthese, sowohl im Skelettmuskel als auch in der Leber. Zu diesem Zwecke ist das ^{31}P Sättigungstransferexperiment an die speziellen in-vivo Gegebenheiten angepaßt worden. Im Rahmen der vorliegenden Arbeit ist ein robustes Messprotokoll entwickelt worden, das mittlerweile in mehr als hundert Probanden zur Bestimmung der muskulären ATP Synthese erfolgreich eingesetzt wurde. Ein Teil der Ergebnisse dieser Messungen ist bereits publiziert worden. Die wichtigsten Ergebnisse dieser Experimente werden in Kapitel 10 zusammengefaßt.

Basierend auf diesen Experimenten wurde ein lokalisiertes Sättigungstransferexperiment entwickelt, welches sich für die Messung der hepatischen ATP Synthese eignet. Bisherige Experimente am Skelettmuskel oder im Hirn verwendeten keine Lokalisierung, die über die räumlich begrenzte Empfindlichkeit der Spule hinausgeht. Dieser Ansatz funktioniert hinreichend gut im Skelettmuskel, ist aber für die Messung an der Leber unzureichend. Die Leber unterscheidet sich in ihren physiologischen wie magnetischen Eigenschaften drastisch von anderen Geweben, unter anderem durch ihren hohen Gehalt an paramagnetischen Substanzen, was zu einer bedeutenden Verkürzung der Relaxationszeiten führt. Auf Grund der Tatsache, dass der Magnetisierungstransfer auf Signaldifferenzen von zwei Experimenten beruht, sind die Anforderungen an das Signalrauschverhältnis hoch. Die Herausforderung bestand darin, ein Experiment zu entwickeln und zu testen, das den Anforderungen gerecht wird und die Messzeit in einem für die meisten Menschen erträglichem Ausmaß bleibt. Die ersten jemals in-vivo gemessenen Ergebnisse hepatischer ATP Syntheseraten befinden sich gegenwärtig in Druck und werden in Kapitel 12 präsentiert.

Zusammenfassend bieten die vorgestellten Experimente eine solide Basis für weiterführende klinische Studien, welche das Verständnis des menschlichen Energiestoffwechsels erweitern werden. Die damit verbundenen neuen Erkenntnisse werden helfen, zukünftig die Diagnose und Therapie verbreiteter Störungen wie Insulinresistenz, Diabetes mellitus, diffuse Lebererkrankungen sowie Herzkreislauferkrankungen zu verbessern.

Abstract

Nuclear magnetic resonance (NMR) is an established technique for the investigation of various kinds of materials, especially organic substances and tissues. In-vivo NMR spectroscopy has become increasingly important over the last decade. In most cases proton NMR spectroscopy is used in-vivo for its high gyromagnetic ratio and abundant presence in all organic molecules.

For the study of energy metabolism, however, other nuclei, especially phosphorus (^{31}P), which shows signals of the high energy phosphates like adenosine-triphosphate (ATP) and phosphocreatine, and carbon (^{13}C) spectroscopy, which allows for the detection of the incorporation of isotope-labelled substrates, are of great importance to metabolic research.

This work is composed of three parts. The first part supplies a summary of the technical background as well as a physiological motivation for the experiments that will be described in in the second and the third part.

After an introduction the basics of nuclear magnetic resonance are summarised. Then radiofrequency pulses, especially B_1 independent pulses or adiabatic RF pulses are explained. It follows a chapter about the physiological relevance of multnuclear NMR spectroscopy, which offers a unique possibility to study human energy metabolism non-invasively. Measuring the activity of the tricarboxylic acid (TCA) cycle and the rates of oxidative phosphorilation are the keys to understanding the backbone of our energy supply. This part is concluded by a description of the experimental setup.

The aim of the second part of this work is to investigate the possibility of increasing the signal of the low intensity ^{13}C nucleus by spectral editing techniques. There are many established procedures from in-vitro high resolution NMR, which are frequently used in analytical chemistry. The question is now to what extent they can be transferred to human in-vivo application where there are severe limits on the available peak and applicable total radiofrequency power per unit time. Also the transmitted high frequency field of the surface coils is inherently inhomogeneous. These coils are used because they have high sensitivity, are simple to construct and are very flexible in their application.

The experiment presented in Chapter 7 is an implementation of the refocused INEPT experiment with B_1 insensitive radiofrequency pulses. The advantage of this sequence over direct detection of ^{13}C signal is not only the sensitivity gain but also a dramatic improvement in the localisation capabilities on the proton channel. Further, protons have significantly shorter T_1 relaxation times, and no uncertainty of the nuclear Overhauser effect has to be taken into account.

Glutamate detection after ^{13}C enriched label incorporation is the key to TCA cycle measurements. With the presented fully adiabatic polarisation transfer sequence the

glutamate signal should be quantifiable significantly better compared to other experiments.

The third part of this work is focused on measuring oxidative phosphorilation in the form of ATP synthesis both in human skeletal muscle and liver. To this end, the ^{31}P magnetisation transfer experiment has been adapted to the specific in-vivo needs and a robust measurement protocol has been developed as part of this work. Meanwhile, in more than a hundred subjects muscle ATP synthesis has been measured successfully, some of the results are already published. The most important results of these experiments will be summarised in Chapter 10.

Based on this experience, it was the goal to develop a localised ^{31}P saturation transfer experiment suitable for the application to the human liver. Experiments performed in other tissues like skeletal muscle or in the brain did not use any localisation other than that of the sensitivity profile of the coil. This approach works well in skeletal muscle, it definitely is inadequate for the application to human liver. The liver has significantly different properties than other tissues because of its high paramagnetic content, resulting in relatively short relaxation times. Since magnetisation transfer relies on the change, or the difference, of the signal from two different experiments, the requirements on signal to noise ratio are high. The challenge was to design and test an experiment that meets those requirements within a tolerable measurement duration for most people. The first results of hepatic ATP synthesis ever measured in-vivo are currently in press and discussed in Chapter 12.

In conclusion, the presented experiments form a solid basis for on-going clinical research studies. These will lead to a significant gain of information accompanied by a better understanding of human metabolism. In consequence, progress in diagnosis and therapy of various metabolic disorders including insulin resistance, diabetes mellitus, diffuse liver disease or cardiovascular diseases can be expected in the future.

Contents

Zusammenfassung 3

Abstract 5

Introduction 11

I. Technical Background 15

1. Nuclear Magnetic Resonance 17
- 1.1. Spins and Magnetic Moments . . . 17
  - 1.1.1. Boltzmann Statistics . . . 18
- 1.2. Spin Motion in a Magnetic Field . . . 19
- 1.3. Chemical Shift . . . 20
- 1.4. High Frequency Electromagnetic Fields . . . 20
- 1.5. Relaxation Phenomena . . . 24
  - 1.5.1. Relaxation Pathways . . . 26
- 1.6. Bloch Equations . . . 27

2. Adiabatic Pulses 29
- 2.1. Basic RF pulses . . . 29
- 2.2. Adiabatic Radiofrequency Pulses . . . 31
- 2.3. Theory . . . 31
  - 2.3.1. The effective field . . . 31
  - 2.3.2. Adiabatic Passage Principle and the Adiabatic Condition . . . 33
- 2.4. Characteristics of adiabatic pulses . . . 33
- 2.5. Excitation and inversion pulses . . . 34
- 2.6. Plane rotation pulses (BIR-4) . . . 36
- 2.7. Modulation functions . . . 40

3. Human Energy Metabolism 43
- 3.1. Skeletal Muscle MRS . . . 45
- 3.2. In-vivo MRS in investigating hepatobilary disease . . . 46
- 3.3. From Nuclear Spin to Metabolic Fluxes . . . 47

4. Experiments **51**
4.1. Hardware Setup . . . 51
4.2. Research on Human Subjects . . . 52
4.3. Implementation and Pulse Programming . . . 52
4.3.1. The Structure of Acquisition in ParaVision . . . 53
4.4. Localisation and the X–nuclei . . . 54
4.4.1. PRESS and STEAM . . . 56
4.4.2. ISIS . . . 57
4.4.3. CSI . . . 57

II. ^{13}C Spectroscopy and Coupled Spins 59

5. ^{13}C Spectroscopy **61**
5.1. Coupled Spins . . . 64
5.2. Nuclear Overhauser Effect . . . 65

6. Heteronuclear Decoupling **67**
6.1. Continuous Wave Decoupling . . . 67
6.2. Composite Pulse Decoupling . . . 69
6.3. Magic Cycles and Supercycles . . . 69
6.4. WALTZ . . . 70
6.5. Adiabatic Decoupling . . . 70

7. Spectral Editing **73**
7.1. Principles of Spectral Editing . . . 73
7.2. Spectral editing methods . . . 74
7.2.1. POCE . . . 74
7.2.2. INEPT . . . 74
7.2.3. DEPT . . . 77
7.3. Fully adiabatic INEPT . . . 80
7.4. The Pulse Sequence . . . 80
7.5. Results . . . 82
7.6. Conclusions . . . 82

III. Chemical Exchange and Energy Metabolism 85

8. The in-vivo ^{31}P Saturation Transfer Experiment **87**
8.1. Theory of Magnetisation Transfer . . . 87
8.2. General Remarks on the Experimental Implementation – ATP Synthesis 88
8.3. Muscle ATP Synthesis . . . 88
8.3.1. Muscle ^{31}P Spectroscopy of the Lower Leg . . . 90
8.3.2. The Pulse Programs . . . 90

8.4. Liver Spectroscopy and ATP Synthesis 93
8.4.1. The Pulse Program 95
8.4.2. ^{31}P Spectra from Human Liver 99

9. Quantification of ^{31}P Spectra **101**
9.1. Quantification of Muscle Spectra 101
9.2. Quantification of Liver Spectra 103

10. Skeletal Muscle ATP Synthesis Rates **107**

11. Hepatic ^{31}P T_1 Relaxation Times **111**

12. Hepatic Rates of ATP Synthesis **113**
12.1. Discussion 113

Summary and Outlook **117**

Bibliography **119**

List of Tables **131**

List of Figures **133**

13. Danksagung **139**

Danksagung **139**

14. Lebenslauf **141**

Lebenslauf **141**

Introduction

Nuclear magnetic resonance (NMR) is based on the observations first made by Bloch in 1946 [1]. It has become increasingly popular over the last decades. There are two fundamentally different ways of using NMR, imaging and spectroscopy. NMR is a widely used technique in analytical chemistry, it provides a wealth of information non-invasively which is difficult to obtain otherwise.

Spectroscopy is used for about fifty years and magnetic resonance imaging (MRI) also has a tradition of more than thirty years by now. Talking about in-vivo NMR in humans, the primary association and general assumption is that it is about imaging, relatively few people know about or even work with in-vivo NMR spectroscopy (MRS).

In-vivo MRS has been performed over decades by a relatively small group of research centres and revealed important insights into energy metabolism, amino acids, intracellular pH or reaction fluxes. In-vivo MRS is a well established method in basic and clinical research in animal models, especially in cancer research and drug design, metabolic research and the investigation of brain functionality.

With the advance to higher static magnetic fields and the wider availability of whole body human scanners more studies are carried out on humans. Especially investigation of energy metabolism can take advantage of NMR. For example, a relatively simple but highly relevant application is the determination of tissue or intracellular fat content by proton MRS. This is highly relevant for the detection and understanding of disorders like insulin resistance, diabetes mellitus, obesity or cardiovascular diseases.

There are, however, several inherent problems associated to spectroscopy like low sensitivity and high demands on magnetic field homogeneity, water suppression (for proton MRS) and, therefore, relatively low spatial and temporal resolution and long measurement times, probing patient compliance. This has limited a widespread clinical application of in-vivo MRS.

Another issue concerning the clinical application is that spectroscopy is a quantitative technique which is not straight forward, difficult to fully automate or standardise. Unlike diagnostic imaging, where contrast between lesion and healthy tissue is simply "seen", the information contained in spectra is not so obvious and more sophisticated techniques are required to retrieve it. Integrating the area under the peak is typically not accurate and reliable enough for the often artifact-rich in-vivo spectra, containing broad-line background signals and overlapping resonances. The properties of in-vivo MRS demand a highly qualified, experienced operator to fully take advantage of its potential.

The focus of this work is, however, not on proton spectroscopy but rather on techniques specific to ^{31}P or ^{13}C spectroscopy. Phosphorus spectra show directly the high energy metabolites like adenosine triphosphate (ATP), phosphocreatine (PCr) and inorganic phosphate (Pi). ATP is the immediate source of about any energy demanding process

in the body and there is undertaken any effort to maintain its levels.

Carbon spectroscopy, which is the central issue in the second part, is distinct from the other nuclei. It has a relatively low gyromagnetic ratio, only about one fourth of that of the proton, and a natural abundance of about 1.1 %. This leads to a very low natural signal intensity. This limits natural abundance ^{13}C MRS to specific applications like glycogen detection. ^{13}C labelled substrate administration, however, allows for the following of metabolic pathways and quantitative monitoring of metabolic rates of, for example, glucose oxidation, or its derivative pyruvate in the citric acid cycle.

Another possibility to improve the signal intensity is by spectral editing. Hereby the fact that many carbon spins are coupled to proton spins is used to transfer sensitive proton magnetisation by entangling them to ^{13}C nuclear spins to the insensitive carbon spin.

An adaptation of a hetero-nuclear polarisation transfer sequence for the use with simple loop coils and maximal sensitivity is one of the main goals of this work. The advantage is the combination of the insensitivity to variations in the transmitting radiofrequency field strength of surface coils and their high detection sensitivity.

The third part of the work will be concerned with localised magnetisation transfer sequences and their application to skeletal muscle and especially human liver tissue.

The methods developed in the context of this work should provide the technical basis to further investigate human tissue energy metabolism in-vivo as a whole. Established proton spectroscopy methods for the detection of ectopic fat content, especially liver and muscle cells, phosphorus magnetisation transfer experiments to provide rates of ATP synthesis and creatine kinase activity. Especially liver ATP synthesis has not been measured in-vivo so far. ^{13}C spectroscopy is applied for glycogen detection and for monitoring the citric acid cycle.

Part one (Technical Background) starting with the next chapter will present the technical background for all of the other parts of this work.

Chapter 1 gives a short introduction into NMR.

Chapter 2 will provide some information on radiofrequency pulses, especially on the so called adiabatic pulses since they have been frequently applied in the experiments this work is based on.

Chapter 3 provides a short review of the role of in-vivo MRS in metabolic research, especially in skeletal muscle and liver. The purpose is to provide a link between the technical aspects of this work and the clinical background. At the end of the chapter it is outlined what was the motivation behind the experiments described in the remainder of the work.

Chapter 4 will give an introduction to the scanner hard- and software, at least the relevant parts of it. Further, the common issues of studies involving in-vivo experiments with humans are discussed, as well as common techniques of in-vivo MRS are summarised.

Part two (^{13}C Spectroscopy and Coupled Spins) of the present work concentrates on the developed hetero-nuclear polarisation transfer sequence (INEPT).

Chapter 5 will describe basic principles and applications of ^{13}C spectroscopy and to heteronuclear coupled spins, their advantages and problems.

Chapter 6 reviews the different techniques of proton decoupling.

Chapter 7 gives an introduction to spectral editing, especially heteronuclear polarisation transfer. The second half of the chapter will discuss the developed fully adiabatic INEPT sequence.

Part three (Chemical Exchange and Energy Metabolism) deals with localised phosphorus spectroscopy, especially for dynamic measurements like magnetisation transfer.

Chapter 8 introduces the theory behind the detection of magnetisation transfer in the implementation of saturation transfer and its translation into experimentally accessible parameters. It also describes the experimental procedure used for the measurement of the saturation transfer and T_1 relaxation times measurements. Signal localisation is discussed and an improved acquisition scheme is introduced.

Chapter 9 deals with the problems of the quantification of phosphorus spectra acquired from skeletal muscle and liver.

Chapter 10 summarises the results of the measurement of skeletal muscle ATP synthesis.

Chapter 11 discusses the hepatic T_1 relaxation times measured at 3 T.

Chapter 12 discusses the results of the saturation transfer experiment and the calculated hepatic ATP synthesis rates, both in the context of technical issues and clinical relevance.

The work is concluded with a brief summary of the presented results and an outlook on where to continue with future research work.

Part I.

Technical Background

1. Nuclear Magnetic Resonance

1.1. Spins and Magnetic Moments

Elements and isotopes are characterised by the number of protons Z and neutrons A in their nucleus. Both neutron and proton have a spin $\boldsymbol{I} = 1/2$. Nuclei may have an integer (including 0) or half integer angular momentum or spin $\boldsymbol{I}$. Table 1.1 lists the properties of some nuclei. The angular momentum is related to a magnetic moment $\boldsymbol{\mu}$

$$\boldsymbol{\mu} = \gamma \boldsymbol{I} = g_I \mu_N \frac{\boldsymbol{I}}{\hbar}. \tag{1.1}$$

A link between the mechanical and electromagnetic properties of the nucleus is the *gyromagnetic ratio* γ and g_I is the *nuclear g-factor* which corrects the classically expected values for quantum mechanical and relativistic effects. μ_N is the nuclear magneton

$$\begin{aligned} \mu_N &= \frac{m_e}{m_p}\mu_B \\ \mu_B &= \frac{e\hbar}{2m_e}, \end{aligned} \tag{1.2}$$

where m_e and m_p are the masses of the electron and the proton, respectively. Both the absolute value $|\boldsymbol{I}|$ and the component $\boldsymbol{I}_z$ parallel to an external static field are quantised:

$$\begin{aligned} |\boldsymbol{I}| &= \sqrt{I(I+1)}\hbar \qquad I = 0, \frac{1}{2}, 1, \frac{3}{2} \ldots \\ I_z &= m_z \hbar \qquad\qquad m_z = -I, -I+1, -I+2, \ldots, I-1, I \end{aligned} \tag{1.3}$$

Hence the magnetic moment is quantised as well and given by

$$\mu = \gamma \hbar I. \tag{1.4}$$

Table 1.1.: Properties of some nuclei.

Z	A	I	${}^A_Z$Nucleus
even	even	0	${}^{12}_{6}$C, ${}^{16}_{8}$O
odd	odd	$\frac{1}{2}, \frac{3}{2}, \frac{5}{2}, \ldots$	${}^{1}_{1}$H, ${}^{15}_{7}$N, ${}^{19}_{9}$F, ${}^{31}_{15}$P
even	odd	$\frac{1}{2}, \frac{3}{2}, \frac{5}{2}, \ldots$	${}^{13}_{6}$C, ${}^{17}_{8}$O
odd	even	$1, 2, 3, \ldots$	${}^{2}_{1}$H, ${}^{14}_{7}$N

The orientation of the nuclear spins is random, in general. In an external magnetic field, however, only $2I+1$ discrete angles with the direction of the magnetic field $\boldsymbol{B}_0$ are possible. For the proton, which is the most widely used nucleus in magnetic resonance imaging and spectroscopy there are two possible orientations.

The potential energy of a dipole $\boldsymbol{\mu}$ in a magnetic field $\boldsymbol{B}_0$ is given by

$$\Delta E = -\boldsymbol{\mu}\boldsymbol{B}_0. \tag{1.5}$$

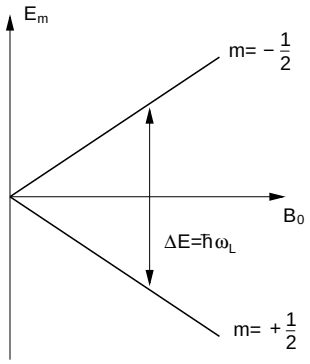

Figure 1.1.: The possible orientations of a spin $I = \frac{1}{2}$ in an external magnetic field.

The different orientations with respect to the z-axis, B_0 per definitionem points into z-direction, correspond to discrete energy eigenvalues

$$E_m = -\gamma\hbar B_0 m_I \quad m_I = -I, -I+1, \ldots I-1, I \tag{1.6}$$

with m_I being one of the $2I+1$ possible eigenvalues of μ_z. For a nucleus with $I = \frac{1}{2}$ two levels are allowed. These levels are separated by an energy gap proportional to B_0:

$$\Delta E = \gamma\hbar B_0. \tag{1.7}$$

Transitions between two levels are accompanied by absorption or emission of photons with energy $\hbar\omega_0 = \Delta E$. The irradiation of an electromagnetic field of frequency ω_0 causes the spins to leave their equilibrium state and acquire a state of higher energy. As the spins return to their lower energy states they emit photons of the same frequency ω_0. This *resonance* phenomenon is the basic of nuclear magnetic resonance.

1.1.1. Boltzmann Statistics

In thermal equilibrium the populations of the two energy levels of a spin system with $I = \frac{1}{2}$ is given by their Boltzmann statistics

$$\frac{n_{-\frac{1}{2}}}{n_{\frac{1}{2}}} = \exp\left(-\frac{\gamma\hbar B_0}{k_\mathrm{B}T}\right). \tag{1.8}$$

$k_\mathrm{B} = 1.3807 \cdot 10^{-23}\,\mathrm{J/K}$ is the Boltzmann constant. The state of lower energy is more populated than the state of higher energy. The resulting net magnetisation of the macroscopic spin system at room temperature and typical field strengths on the order of $B_0 = 1\,\mathrm{T}$ is, however, very small compared to the thermal energy $k_\mathrm{B}T$. In other words, only a very small fraction of the spins contribute to the detectable signal which is given by

$$\frac{n_{-\frac{1}{2}}}{n_{\frac{1}{2}}} \approx \frac{1}{10^5}. \tag{1.9}$$

Given the large number of nuclei usually encountered in the sample of an NMR experiment this still leads to a detectable net magnetisation. Inserting $N = n_{-\frac{1}{2}} + n_{\frac{1}{2}}$ and $\Delta n = n_{-\frac{1}{2}} - n_{\frac{1}{2}}$ into Eq. 1.8 yields for $I = \frac{1}{2}$

$$\Delta n = N \cdot \tanh\left(\frac{\gamma\hbar B_0}{2k_\mathrm{B}T}\right) \approx \frac{N\gamma\hbar B_0}{2k_\mathrm{B}T} \tag{1.10}$$

and a total magnetisation:

$$M_0 = \Delta n \cdot \mu \approx \frac{N\mu\gamma\hbar B_0}{2k_\mathrm{B}T}. \tag{1.11}$$

1.2. Spin Motion in a Magnetic Field

A static magnetic field

$$\boldsymbol{B}_0 = \begin{pmatrix} 0 \\ 0 \\ B_0 \end{pmatrix} \tag{1.12}$$

exerts a torque on the magnetic moment

$$\boldsymbol{T} = \boldsymbol{\mu} \times \boldsymbol{B}_0 \tag{1.13}$$

which causes a change in the angular momentum

$$\frac{\mathrm{d}\boldsymbol{I}}{\mathrm{d}t} = \boldsymbol{T} = \boldsymbol{\mu} \times \boldsymbol{B}_0 \tag{1.14}$$

and using (1.1)

$$\frac{\mathrm{d}\boldsymbol{\mu}}{\mathrm{d}t} = \boldsymbol{\mu} \times \gamma\boldsymbol{B}_0 = \boldsymbol{\omega}_0 \times \boldsymbol{\mu}. \tag{1.15}$$

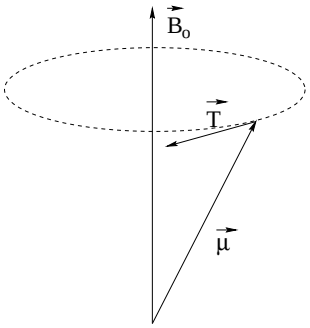

Figure 1.2.: Torque on a magnetic moment in an external magnetic field.

The frequency $\boldsymbol{\omega}_0 = -\gamma\boldsymbol{B}_0$ is the *Larmor frequency*. It is the frequency at which the magnetic moment $\boldsymbol{\mu}$ precesses about the direction of the magnetic field B_0. Equation (1.15) is a system of three differential equations

$$\begin{aligned} \dot{\mu}_x &= \omega_0\mu_y \\ \dot{\mu}_y &= \omega_0\mu_x \\ \dot{\mu}_z &= 0, \end{aligned} \tag{1.16}$$

with a solution for the magnetic moment of the form

$$\boldsymbol{\mu} = \begin{pmatrix} \mu_{xy}\cos\,\omega_0 t \\ \mu_{xy}\sin\,\omega_0 t \\ \mu_z \end{pmatrix}. \tag{1.17}$$

The macroscopic magnetisation vector $\boldsymbol{M}$, which can be expressed as the sum of several individual magnetic moments,

$$\boldsymbol{M} = \sum_i \boldsymbol{\mu}_i, \tag{1.18}$$

follow the same equations of motion as single magnetic moments

$$\frac{\mathrm{d}\boldsymbol{M}}{\mathrm{d}t} = \boldsymbol{\omega}_0 \times \boldsymbol{M} = -\gamma \begin{pmatrix} 0 \\ 0 \\ B_0 \end{pmatrix} \times \boldsymbol{M} \tag{1.19}$$

with equal solutions

$$\boldsymbol{M} = \begin{pmatrix} M_{xy} \cos\, \omega_0 t \\ M_{xy} \sin\, \omega_0 t \\ M_z \end{pmatrix}. \tag{1.20}$$

1.3. Chemical Shift

The *chemical shift* describes the influence of the effective magnetic field including shielding effects of the electrons on the nucleus. The resonance frequency not only depends on the gyromagnetic ratio of the isotope and $\boldsymbol{B}_0$, but also on the local effective field. If it would magnetic resonance spectroscopy would be of very limit usage since all molecules with the same isotope would resonate at the same frequency. The magnetic field at the site of the nucleus strongly depends on the chemical environment of the molecule. The nature of this influence is the shielding or screening of the $\boldsymbol{B}_0$ field by electrons. It is referred to as the *chemical shift*. The electrons precess about the $\boldsymbol{B}_0$ field in the opposite direction than the nuclei. Their moving charge induces a magnetic moment that reduces the static magnetic field.

$$\mathbf{B} = \boldsymbol{B_0}(\mathbf{1} - \sigma) \tag{1.21}$$

σ is the shielding. The shielding is not necessarily homogeneous so σ is, in general, a 3×3 tensor. If their is, however, sufficient nuclear tumbling, the anisotropy is averaged and it can be described by its trace. In this case it is a dimensionless constant usually given in ppm. The corresponding Larmor frequency is given by

$$\boldsymbol{\omega}_0 = \gamma \boldsymbol{B}_0 (1 - \sigma). \tag{1.22}$$

The presentation of chemical shifts in ppm has the advantage that it is independent of the static magnetic field. Common reference signals for the chemical shift are tetramethylsilane (TMS) which defines 0 ppm in proton and ^{13}C spectroscopy. Since it is not encountered in-vivo, internal reference signals are often used, instead. The chemical shift phosphocreatine (PCr) is defined as 0 ppm in ^{31}P MRS.

1.4. High Frequency Electromagnetic Fields

The application of electromagnetic fields perpendicular to the static magnetic field and a frequency ω, where the frequency is in the range of radio waves, therefore this field

$\boldsymbol{B_1}$ is called *radiofrequency (RF) field*,

$$\boldsymbol{B}_1 = \begin{pmatrix} B_1 \cos \omega t \\ B_1 \sin \omega t \\ 0 \end{pmatrix}, \tag{1.23}$$

results in a modification of the equation of motion (Eq. (1.18)):

$$\frac{\mathrm{d}\boldsymbol{M}}{\mathrm{d}t} = -\gamma \boldsymbol{B} \times \boldsymbol{M} \quad \text{with} \quad \boldsymbol{B} = \begin{pmatrix} B_1 \cos \omega t \\ B_1 \sin \omega t \\ B_0 \end{pmatrix}. \tag{1.24}$$

Introduction of a rotating frame of reference, where the coordinates $(e_{x'}, e_{y'}, e_{z'})$ rotate with the RF field about the $\boldsymbol{z} = \boldsymbol{z}'$-axis simplifies the problem:

$$\frac{\mathrm{d}\boldsymbol{M'}}{\mathrm{d}t} = -\gamma \boldsymbol{B'} \times \boldsymbol{M'} = \boldsymbol{\omega'} \times \boldsymbol{M'}, \tag{1.25}$$

where $\boldsymbol{B'}$ is $\boldsymbol{B}$ as seen from the rotating frame. The transformation matrix from the resting frame of reference to the rotating frame is

$$\mathsf{R} = \begin{pmatrix} \cos \omega t & \sin \omega t & 0 \\ -\sin \omega t & \cos \omega t & 0 \\ 0 & 0 & 1 \end{pmatrix}, \tag{1.26}$$

The field becomes

$$\boldsymbol{B'} = \mathsf{R}\boldsymbol{B} = \begin{pmatrix} B_1 \\ 0 \\ B_0 \end{pmatrix}. \tag{1.27}$$

The derivative with respect to time needs also be transformed

$$\frac{\mathrm{d}\boldsymbol{A}}{\mathrm{d}t} = \frac{\mathrm{d}'\boldsymbol{A}}{\mathrm{d}t} + \boldsymbol{\omega} \times \boldsymbol{A}. \tag{1.28}$$

The variation with time seen from the resting frame is the variation with time in the rotating frame combined with the rotation of the rotating frame. The vector in the rotating frame is the sum of the vector pointing to the origin of the rotating frame and the vector within the rotating frame

$$\begin{aligned} \boldsymbol{M} &= \boldsymbol{r}_{OO'} + \boldsymbol{M'} \\ \frac{\mathrm{d}\boldsymbol{M}}{\mathrm{d}t} &= \frac{\mathrm{d}\boldsymbol{r}_{OO'}}{\mathrm{d}t} + \frac{\mathrm{d}\boldsymbol{M'}}{\mathrm{d}t} = \frac{\mathrm{d}\boldsymbol{M'}}{\mathrm{d}t}. \end{aligned} \tag{1.29}$$

If we let the origins of the two frames coincide, the vector $\boldsymbol{r}_{OO'}$ and its time derivative $\frac{\mathrm{d}\boldsymbol{r}_{OO'}}{\mathrm{d}t}$ become zero. This results in

$$\frac{\mathrm{d}\boldsymbol{M'}}{\mathrm{d}t} = \frac{\mathrm{d}\boldsymbol{M}}{\mathrm{d}t} = \frac{\mathrm{d}'\boldsymbol{M}'}{\mathrm{d}t} + \boldsymbol{\omega} \times \boldsymbol{M'}. \tag{1.30}$$

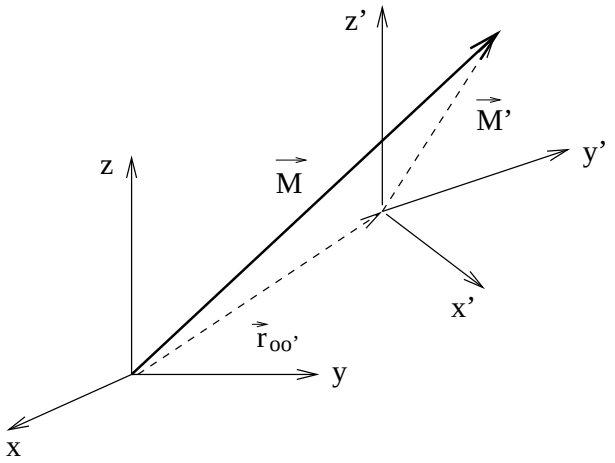

Figure 1.3.: Magnetisation in two frames of reference. The coordinates x, y, and z denote the resting frame, the primed coordinates denote the moving frame.

With the help of equations (1.25) and (1.29) for the term on the left side one gets

$$-\gamma \boldsymbol{B'} \times \boldsymbol{M'} = \frac{\mathrm{d}'\boldsymbol{M'}}{\mathrm{d}t} + \boldsymbol{\omega} \times \boldsymbol{M'}. \tag{1.31}$$

which can be rewritten as

$$\frac{\mathrm{d}'\boldsymbol{M'}}{\mathrm{d}t} = \begin{pmatrix} \omega M'_y \\ -\omega M'_x \\ 0 \end{pmatrix} + \begin{pmatrix} \gamma B_0 M'_y \\ -\gamma B_0 M'_x + \gamma B_1 M'_z \\ -\gamma B_1 M'_y \end{pmatrix} = -\gamma \begin{pmatrix} B_1 \\ 0 \\ B_0 + \frac{\omega}{\gamma} \end{pmatrix} \times \begin{pmatrix} M'_x \\ M'_y \\ M'_z \end{pmatrix} \tag{1.32}$$

This equation is very similar to Eq. (1.18). Only the $\boldsymbol{B''}$-field has an additional component B_1. It describes the precession of the magnetisation about an effective field

$$\boldsymbol{B''} = \begin{pmatrix} B_1 \\ 0 \\ B_0 - \frac{\omega}{\gamma} \end{pmatrix} \tag{1.33}$$

with an effective frequency

$$\omega'' = \gamma |\boldsymbol{B''}| = \sqrt{(\omega_0 - \omega)^2 + \omega_1^2}. \tag{1.34}$$

Equation (1.32) is a system of three differential equations:

$$\begin{aligned} \dot{M}'_x &= -(\omega_0 - \omega) M'_y \\ \dot{M}'_y &= -M'_z \omega_1 + (\omega_0 - \omega) M'_x \\ \dot{M}'_z &= \omega_1 M'_y. \end{aligned} \tag{1.35}$$

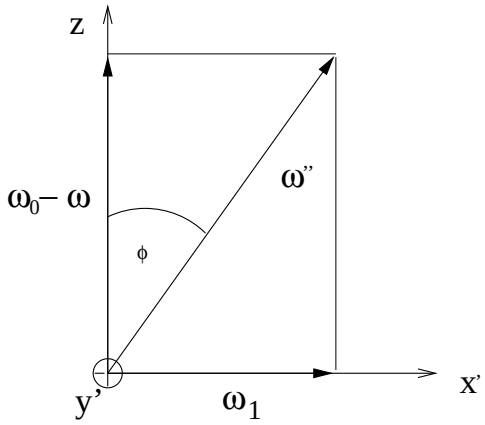

Figure 1.4.: Axis of precession in the rotating frame.

The solution of this system of equations is analogous to the solution of equations (1.16) if it is rotated about the y'-axis by an angle α that is given by ω_1 and ω'' (Fig. 1.4). Then the solution becomes:

$$\begin{pmatrix} M''_{xy}\cos\,\omega''t \\ M''_{xy}\sin\,\omega''t \\ M''_z \end{pmatrix}. \tag{1.36}$$

If this is rotated back by the angle α and the result transformed back into the resting frame one obtains $\boldsymbol{M}(t)$.

$$\begin{aligned}\begin{pmatrix} M_x \\ M_y \\ M_z \end{pmatrix} &= \begin{pmatrix} \cos\,\omega t & -\sin\omega t & 0 \\ \sin\omega t & \cos\omega t & 0 \\ 0 & 0 & 1 \end{pmatrix} \begin{pmatrix} \cos\alpha & 0 & \sin\alpha \\ 0 & 1 & 0 \\ -\sin\,\alpha & 0 & \cos\alpha \end{pmatrix} \begin{pmatrix} M''_{xy}\cos\,\omega''t \\ M''_{xy}\sin\,\omega''t \\ M_z \end{pmatrix} \\ &= \begin{pmatrix} \frac{1}{\omega''}\left[(\omega_0-\omega)\,M''_{xy}\cos\omega''t\,\cos\omega t+\omega_1 M''_z\cos\omega t\right]-M''_{xy}\sin\omega''t\,\sin\omega t \\ \frac{1}{\omega''}\left[(\omega_0-\omega)\,M''_{xy}\cos\omega''t\,\sin\omega t+\omega_1 M''_z\sin\omega t\right]+M''_{xy}\sin\omega''t\,\cos\omega t \\ \frac{1}{\omega''}\left[(\omega_0-\omega)\,M''_z-\omega_1 M''_{xy}\cos\,\omega''t\right] \end{pmatrix}\end{aligned}$$

where

$$\omega_0 = -\gamma B_0 \qquad\qquad \omega_1 = -\gamma B_1. \tag{1.37}$$

From the form of the effective Larmor frequency it becomes clear that if $\omega_0 = \omega$ or

$$\omega_0 - \omega = \Delta\omega = 0 \tag{1.38}$$

the effective field will have the form

$$\begin{pmatrix} B_1 \\ 0 \\ 0 \end{pmatrix}. \tag{1.39}$$

The precessing motion of $\boldsymbol{M'}$ with the frequency ω_1 becomes a simple inclination by an angle

$$\phi(t) = \omega_1 t = -\gamma B_1 t \tag{1.40}$$

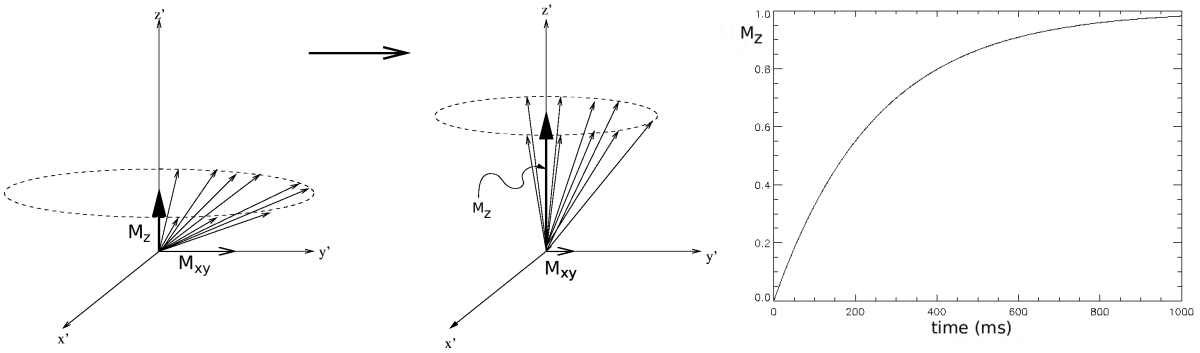

Figure 1.5.: Spin-lattice relaxation: Return of magnetisation from the xy - plane towards M_z. At the same time spin-spin relaxation takes place. This is indicated by a dephasing of the spins. The increase of M_z after the external magnetic field is applied is shown in the right panel.

around an axis in the $x'y'$-plane. Choosing the proper amplitude and/or the duration of B_1, the magnetisation will be flipped by a certain angle, e.g.

$$\begin{aligned} B_1 \Delta t &= -\frac{\pi}{2\gamma} \rightarrow \phi = \frac{\pi}{2} \\ B_1 \Delta t &= -\frac{\pi}{\gamma} \rightarrow \phi = \pi. \end{aligned} \tag{1.41}$$

1.5. Relaxation Phenomena

The interaction of spins with their environment leads to a spontaneous return to the thermal equilibrium. After application of radiofrequency fields, that nutate the spins away from the direction of the B_0 field, the spins are on a higher energy level and therefore return to their initial orientation. The characteristic time of this process is called the spin-lattice relaxation time or T_1 time. Maxwell's theorem of relaxation states that a system returns the faster towards equilibrium the larger the deviation from the equilibrium. In mathematical terms this becomes a first order linear differential equation

$$\frac{\mathrm{d}M_z}{\mathrm{d}t} = -\frac{M_z - M_0}{T_1}, \tag{1.42}$$

where M_z is the magnetisation along the z-axis at time t after excitation and M_0 is the equilibrium z-magnetisation. This equation is solved by

$$M_z(t) = M_0 \left(1 - \mathrm{e}^{-\frac{t}{T_1}}\right) + M_z(0_+) \cdot \mathrm{e}^{-\frac{t}{T_1}}, \tag{1.43}$$

where $M_z(0_+)$ is the z-magnetisation immediately after the RF-pulse. The time constant T_1 is called longitudinal or spin-lattice relaxation time (Fig. 1.5).

Typical T_1-values of human tissues are given in Tab. 1.2 [2]. Solid insulators or bones can have relaxation times of up to 1000 s and metals in the range of ms. The other type

Table 1.2.: Spin-lattice relaxation times and spin-spin relaxation times of several tissues at a field strength of 3 T. Note that T_2 is always shorter than T_1. Brain data reproduced from [3], muscle data from [4]; TMA: trimethylamonium resonance, IMCL: intramyocellular lipids, EMCL: extracellular lipids.

Tissue	$T_1(ms)$	$T_2(ms)$
Frontal grey matter	1322±34	110±4
Parasagittal frontal grey matter	1392±27	104±2
Insular grey matter	1356±33	102±2
Parietal grey matter	1276±33	112±4
Parasagittal occipital grey matter	1356±29	98±3
Occipital grey matter	1283±37	132±9
Frontal white matter	838±18	74±1
Parietal white matter	827±19	80±1
Occipital white matter	832±18	84±1
Soleus muscle	1377±37	31.3±1.2
Tibialis anterior muscle	1387±12	28.4±0.7
Soleus creatine (CH_3)	1000±70	115±13
Tibialis anterior creatine (CH_3)	1096±76	132±17
Soleus TMA	1010±59	119±15
Tibialis anterior TMA	945±65	78.6±5.1
Soleus IMCL	369±39	89.4±6.0
Tibialis anterior IMCL	413±22	90.9±7.0
Soleus EMCL	369±42	77.6±6.4
Tibialis anterior EMCL	420±37	77.5±3.6

of relaxation is the so called transversal or spin-spin relaxation. After the equilibrium z-magnetisation is transferred to the transversal plane, the spins are all aligned to one axis. They continue to precess about the $\boldsymbol{B_0}$ field. Over time, small microscopic differences in the Larmor frequency cause the spins to fan out and the coherences of them are lost. The characteristic time is also called T_2 time.

$$M_{xy}(t) = M_{xy}(t=0)\mathrm{e}^{-\frac{t}{T_2}}. \tag{1.44}$$

Figure 1.6 shows spin-spin relaxation seen from the rotating frame. Spin-lattice relaxation and spin-spin relaxation occur independently. The former is due to an energy exchange with the lattice and the latter is a mere signal loss due to a randomisation of spin orientations. The differences in relaxation times T_1 and T_2 between different tissue types give rise to image contrast in anatomical MRI.

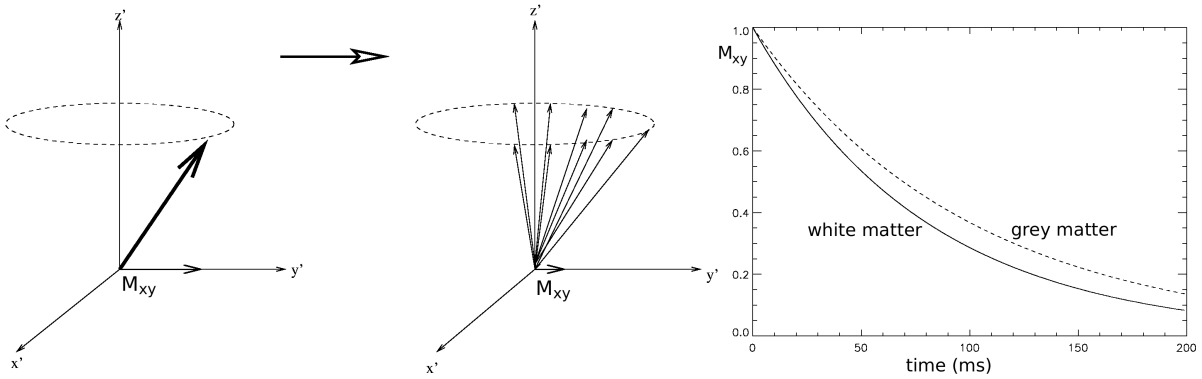

Figure 1.6.: The spins experience different local field strengths that causes the transversal magnetisation M_{xy} to decreases. The relaxation rate depends on the spin's environment, giving rise to contrast (right).

1.5.1. Relaxation Pathways

The most important relaxation pathway is often the dipole-dipole interactions. as explained by the theory introduced by Bloembergen, Purcell and Pound (BPP-theory) [5]. The resulting relaxation times are given by equations (1.46) and (1.46):

$$\frac{1}{T_1} = \frac{3}{10}\frac{\gamma^4\hbar^2}{4\pi^2 r^6}\left(\frac{\tau_c}{1+\omega_0^2\tau_c^2}+\frac{4\tau_c}{1+4\omega_0^2\tau_c^2}\right) \tag{1.45}$$

$$\frac{1}{T_2} = \frac{3}{20}\frac{\gamma^4\hbar^2}{4\pi^2 r^6}\left(3\tau_c+\frac{5\tau_c}{1+\omega_0^2\tau_c^2}+\frac{2\tau_c}{1+4\omega_0^2\tau_c^2}\right), \tag{1.46}$$

where τ_c is the molecular correlation time. In the *extreme narrowing limit* ($\omega_0\tau_c \ll 1$), where the molecular tumbling is very fast, equations (1.46) and (1.46) become

$$\frac{1}{T_1} = \frac{1}{T_2} = \frac{3}{2}\frac{\gamma^4\hbar^2}{4\pi^2 r^6}\tau_c. \tag{1.47}$$

In fluids, where the major part of the molecules is highly mobile, T_2 relaxation times can be very long. In large bound molecules, on the contrary, the mobility is very restricted, τ_c is very short, resulting in broad undetectable lines with very short T_2 times.

There are, however, other interactions that lead to relaxation:

- Magnetic dipole-dipole interactions.
- Electric quadrupole interactions.
- Chemical shift anisotropy.
- Spin rotation interactions.
- Scalar interactions.

Nuclei with spin $I > 1/2$ possess an electric quadrupole moment which interacts with local electric field gradients. Fluctuation in this interaction, as caused by molecular motion, will induce relaxation. For many nuclei with a quadrupolar moment like ^{23}Na or ^{39}K this is the predominant relaxation pathway, making their T_1 relaxation times in the order of ms.

The shielding effect of the electrons represented by the chemical shift is, as stated above, actually a 3×3 tensor. Although the observed signal may not be effected by chemical shift anisotropy, the nucleus will, nevertheless, experience fluctuations in the local magnetic field which provide yet another pathway for relaxation.

$$\frac{1}{T_1} = \frac{1}{15}\omega_0^2(\sigma_\parallel - \sigma_\perp)^2 \frac{2\tau_c}{1+\omega_0^2\tau_c^2} \tag{1.48}$$

$$\frac{1}{T_2} = \frac{1}{90}\omega_0^2(\sigma_\parallel - \sigma_\perp)^2 \left[\frac{6\tau_c}{1+\omega_0^2\tau_c^2} + 8\tau_c\right], \tag{1.49}$$

In the extreme narrowing limit equations (1.49) and (1.49) reduce to

$$\frac{1}{T_1} = \frac{2}{15}\omega_0^2(\sigma_\parallel - \sigma_\perp)^2\tau_c \tag{1.50}$$

$$\frac{1}{T_2} = \frac{7}{45}\omega_0^2(\sigma_\parallel - \sigma_\perp)^2\tau_c. \tag{1.51}$$

The relaxation rates of chemical shift anisotropy increase quadratically with B_0. Therefore, it can be expected that it contributes more to relaxation rates when increasing the static magnetic field strength.

Spin rotation relaxation occurs if coherent molecular motion is coupled to the nuclear spin and this coupling is interrupted by (e.g. by collisions). It has little importance in in-vivo MRS [6].

Scalar coupling, which will be discussed in more detail in part two of this work, is a coupling between spins independent of the static magnetic field. If for some reason the coupling constant or the spin population of one spin becomes time dependent, it leads to relaxation of the coupled spin.

1.6. Bloch Equations

Introducing the effects of relaxation into equation (1.15) results in the Bloch equations

$$\begin{aligned}
\frac{\mathrm{d}M_x}{\mathrm{d}t} &= \gamma(M_yB_z - M_zB_y) - \frac{M_x}{T_2} \\
\frac{\mathrm{d}M_y}{\mathrm{d}t} &= \gamma(M_zB_x - M_xB_z) - \frac{M_y}{T_2} \\
\frac{\mathrm{d}M_z}{\mathrm{d}t} &= \gamma(M_xB_y - M_yB_x) - \frac{M_z - M_0}{T_1},
\end{aligned} \tag{1.52}$$

which in the rotating frame become

$$\begin{aligned}
\frac{\mathrm{d}M_{x'}}{\mathrm{d}t} &= -\frac{1}{T_2}M_{x'} - \Delta\omega M_{y'} \\
\frac{\mathrm{d}M_{y'}}{\mathrm{d}t} &= \Delta\omega M_{x'} - \frac{1}{T_2}M_{y'} - \omega_1 M_{z'} \\
\frac{\mathrm{d}M_{z'}}{\mathrm{d}t} &= \omega_1 M_{y'} - \frac{1}{T_1}\left(M_{z'} - M_0\right). \qquad (1.53)
\end{aligned}$$

The Bloch equations describe the classical motion of spins under the influence of relaxation processes.

2. Adiabatic Pulses

In textbooks the magnetisation always directs to either x, y, or z-direction, pulses are either 90 ° or 180 °, and the field is homogeneous. Under these conditions, many sophisticated experiments work nicely. Ideal conditions, however, are most likely not to be encountered in real world applications, especially not in in-vivo experiments.

An important issue, even in very simple experiments, is to apply a well defined flip angle of the radiofrequency pulse across the region of interest. On the other hand, because high sensitivity is important, or nothing else is available, a surface coil will be used. With its inhomogeneous field distribution a defined flip angle over a larger area appears something impossible.

Figure 2.1 shows the distribution of the B_1 field of different coils. The field varies drastically across the sensitive volume of the surface coil. When adiabatic excitation pulses are used, the sensitive volume of the coil can be increased significantly.

2.1. Basic RF pulses

In general, a radiofrequency pulse represents a magnetic field of strength $\boldsymbol{B}_1(t)$ applied for a limited period of time, hence the name pulse. The shape, amplitude and phase, and the direction of the field determine the way the pulse acts on the magnetisation. We talk about basic RF pulses if only the amplitude is modulated over time. The flip angle produced by a basic RF pulse can be calculated as

$$\theta = \gamma \int_0^T B_1(t). \tag{2.1}$$

The simplest RF pulse is the square or block pulse. Here, $\boldsymbol{B}_1(t)$ is on for $0 \leq t < T$, and zero otherwise. For a block pulse of duration T the on-resonance flip angle θ is easy to calculate:

$$\theta = \gamma B_1 T. \tag{2.2}$$

It is a very efficient way in terms of applied power and duration to achieve a non-selective manipulation of spins.

It is frequently used in simple pulse-acquire experiments, for magnetisation transfer or sometimes for 3D-image excitation. Also, it is used as the basic building block of composite pulses and decoupling experiments.

An important characteristic of a radiofrequency pulse is its off-resonance behaviour, or the pulse profile. It describes the nutation of spins with a frequency offset $\Delta\omega$. The profile of the square pulse is not well defined. Unless $\gamma B_1 \gg \Delta\omega$, the pulse will not produce the desired flip angle.

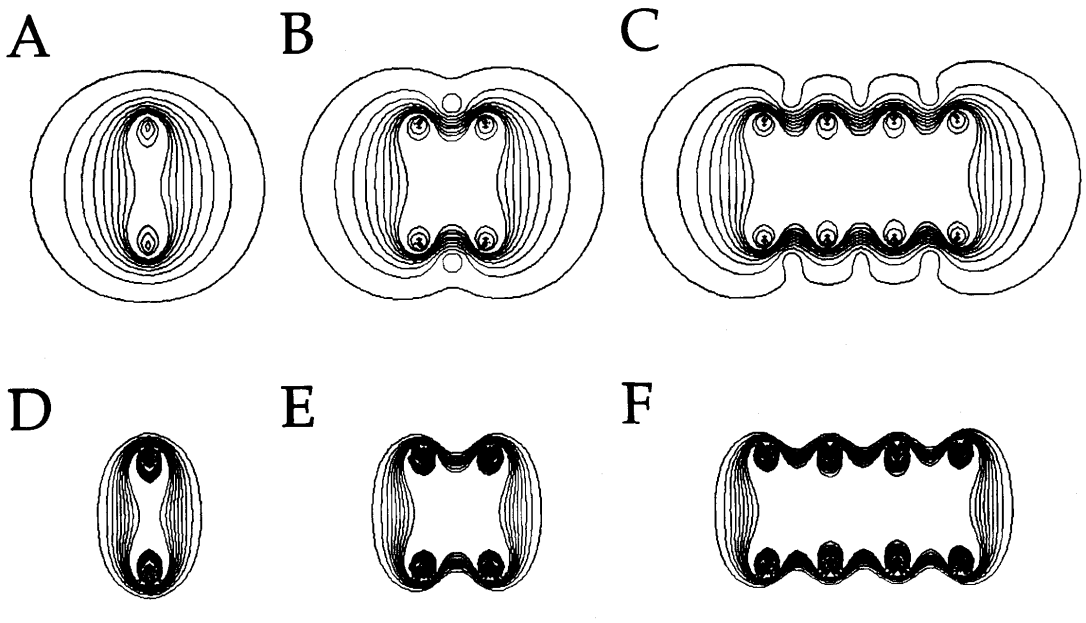

Figure 2.1.: Magnetic field distribution of (A/D) a single-turn surface coil, (B/E) a two-turn solenoidal coil (Helmholtz coil3 and (C/F) a four-turn solenoidal coil. for the coils in (B) and (C), the winding separation equals half the diameter. The B_1 distribution of (A-C) corresponds to the sensitivity following homogeneous (i.e. B_1 insensitive) excitation, for instance with adiabatic RF pulses. (D-F) show the sensitivity profiles of the coils following a 9O° excitation with a conventional square RF pulse. The B_1 dependence of the nutation angle significantly reduces the sensitive volumes of the coils. Reproduced from [6].

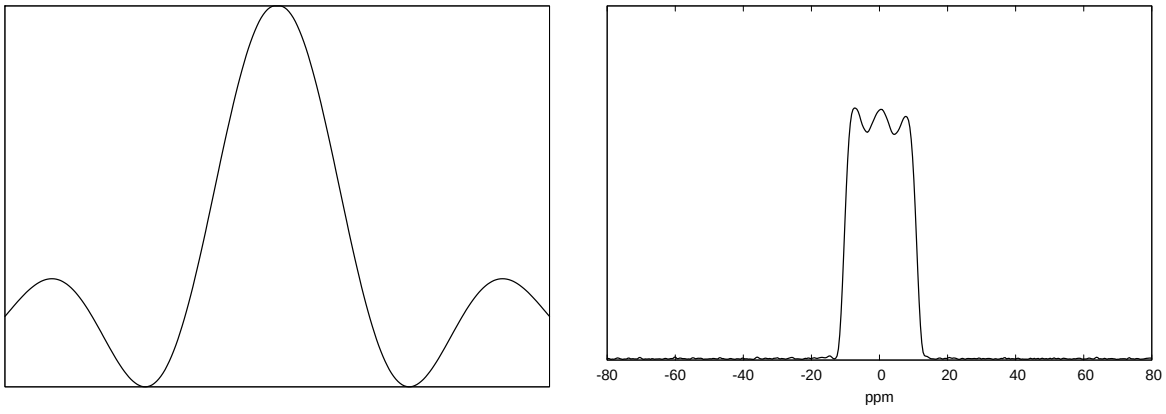

Figure 2.2.: Amplitude (left) and excitation profile (right) of a 2 ms three-lobe sinc pulse. The basic frequency was 125.7 MHz.

Another, very popular, pulse is the so called sinc pulse. The sinc function is

$$\mathrm{sinc}(t) = \sin(t)/t. \tag{2.3}$$

Typically, a cut-off of three or five lobes is chosen. The sinc pulse's profile is basically frequency selective, besides small side lobes and overshoots and therefore commonly used in slice-selection in combination with gradients, either for excitation or refocusing. The sinc pulse and its profile are displayed in Figure 2.2.

There are other pulses like Gaussian, Hermite, etc., with their specific characteristics, but all these pulses have in common that it is solely an amplitude modulation of the basic RF-frequency.

2.2. Adiabatic Radiofrequency Pulses

The question behind adiabatic pulses is: Are there radiofrequency pulses that can achieve excitation, inversion or refocusing of magnetisation independent of the local B_1 field strength?

These cannot be pulses that follow equation (2.1). Unlike basic RF pulses, adiabatic pulses, adiabatic pulses exhibit also a frequency modulation, or a variation of phase, depending on the implementation. Adiabatic pulses perform their desired action (90 °, 180 °, etc.) independent of the local B_1 field strength, as long as it is above a certain threshold. It should be stated that there is also a maximal field strength.

Unlike regular RF pulses, adiabatic pulses are designed for one specific flip angle, it is not possible to change an excitation (90 °) pulse to an inversion (180 °) pulse by increasing its amplitude or altering its duration.

2.3. Theory

2.3.1. The effective field

The way, adiabatic pulse work are best explained using an effective magnetic field. If not stated otherwise, let us assume, without loss of generalisation, that the initial orientation of the B_1-field is along the x-direction.

A pulse of time dependent amplitude $A(t)$ and a carrier frequency $\omega_{RF}(t)$

$$B_1(t) = A(t)e^{-i\omega_{RF}(t)t)} \tag{2.4}$$

In a rotating – time dependent – frame of reference of angular frequency $\omega_{RF}(t)$, $B_1(t)$ can be decomposed into two orthogonal components. The transverse component of the initial B_1 field is set along the $\boldsymbol{x}$ axis,

$$B_x(t) = A(t). \tag{2.5}$$

The longitudinal component B_z in the rotating frame representation reads

$$B_z(t) = \frac{1}{\gamma}[\omega - \omega_{RF}(t)] = B_0 - \frac{\omega_{RF}(t)}{\gamma}, \tag{2.6}$$

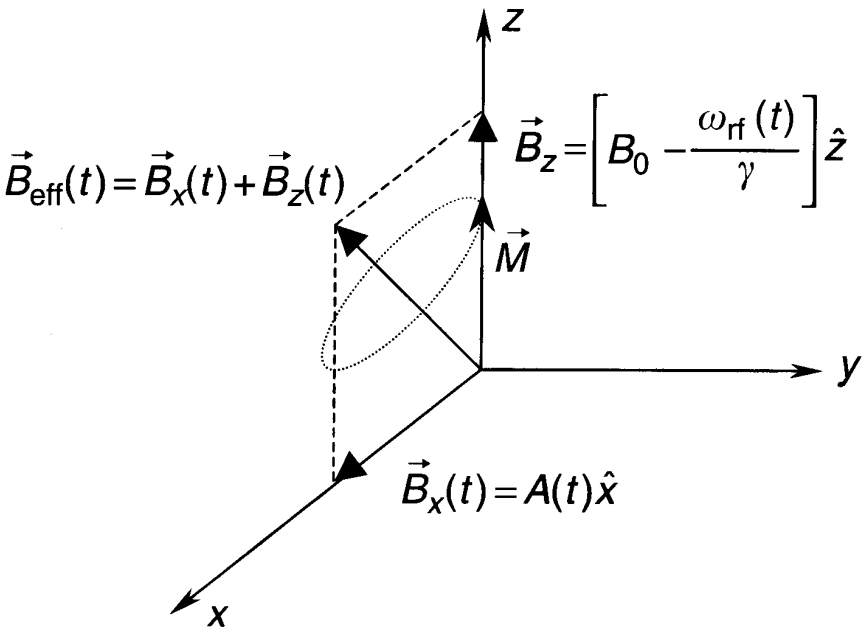

Figure 2.3.: The relationship between the applied B_1 field with amplitude $A(t)$ and frequency $\omega_{RF}(t)$ modulations, the effective magnetic field $\boldsymbol{B}_{eff}$, and the magnetisation $\boldsymbol{M}$ in the rotating reference frame. The magnetisation vector precesses about the effective field and traces a cone, as indicated by the dotted path. Reproduced from [7]

where ω is the Larmor frequency of the static magnetic field B_0.

Taking together (2.5) and (2.6), the amplitude and direction of the effective field B_{eff} are

$$B_{eff}(t) = \sqrt{B_x^2(t) + B_z^2(t)} \tag{2.7}$$

$$\psi(t) = \arctan\left(\frac{B_x(t)}{B_z(t)}\right). \tag{2.8}$$

The effective field is in the transverse plane if $\omega_{RF} = \omega$ or on-resonance. In this case, the effective field coincides with the B_1-field. Otherwise it is tilted to the longitudinal axis.

The magnetisation precesses around the effective field as it precesses about the static B_1-field in the absence of radiofrequency irradiation. This description will help greatly to simplify the interpretation of the interaction of the magnetisation and the radiofrequency pulse. The relationship between $\boldsymbol{B}_1$, $\boldsymbol{B}_{eff}$ and the magnetisation $\boldsymbol{M}$ is also illustrated in 2.3

2.3.2. Adiabatic Passage Principle and the Adiabatic Condition

The *adiabatic passage principle* says that the magnetisation vector follows the direction of the effective field (Figure 2.3 as long as it does not change much during one period of precession. In other words,

$$\dot{\psi} = \left| \frac{d\psi}{dt} \right| \ll \gamma B_{eff}. \tag{2.9}$$

This is known as the *adiabatic condition*. A useful definition is the adiabatic factor η:

$$\eta = \gamma \frac{B_{eff}}{|\dot{\psi}|}, \tag{2.10}$$

With this definition the adiabatic condition (2.9) can be rewritten As

$$\eta \gg 1. \tag{2.11}$$

This means that if η is sufficiently large

- magnetisation initially parallel to the effective field will stay collinear with it, whereas
- a magnetisation initially orthogonal will precess about $\boldsymbol{B}_1$ in a plane normal to $\boldsymbol{B}_{eff}$.

$$\beta = \gamma \int \boldsymbol{B}_{eff}(t)dt = \gamma \int \sqrt{\boldsymbol{B}_1^2 + \left(\frac{\omega - \omega_{RF}(t)}{\gamma} \right)^2} \tag{2.12}$$

The latter will become especially important for plane rotating pulses.

The trajectory of the magnetisation following the effective field for different values of η is illustrated in Figure 6.2.

2.4. Characteristics of adiabatic pulses

There are some important differences between conventional and adiabatic radiofrequency pulses.

1. Adiabatic pulses require both amplitude and frequency (or phase) modulation, whereas basic RF pulses are usually only amplitude modulated.
2. Adiabatic pulses do not obey (2.1), they can generate a uniform flip angle in the presence of significant B_1 variations.
3. At the end of adiabatic excitation, the magnetisation vector points into the same direction as the $\boldsymbol{B}_1$ field.
4. To satisfy the adiabatic condition, usually considerably larger B_1 amplitudes are required compared to conventional pulses. Further, the pulse duration can be much longer, increasing the sensitivity to off resonance, flow and relaxation effects.

.

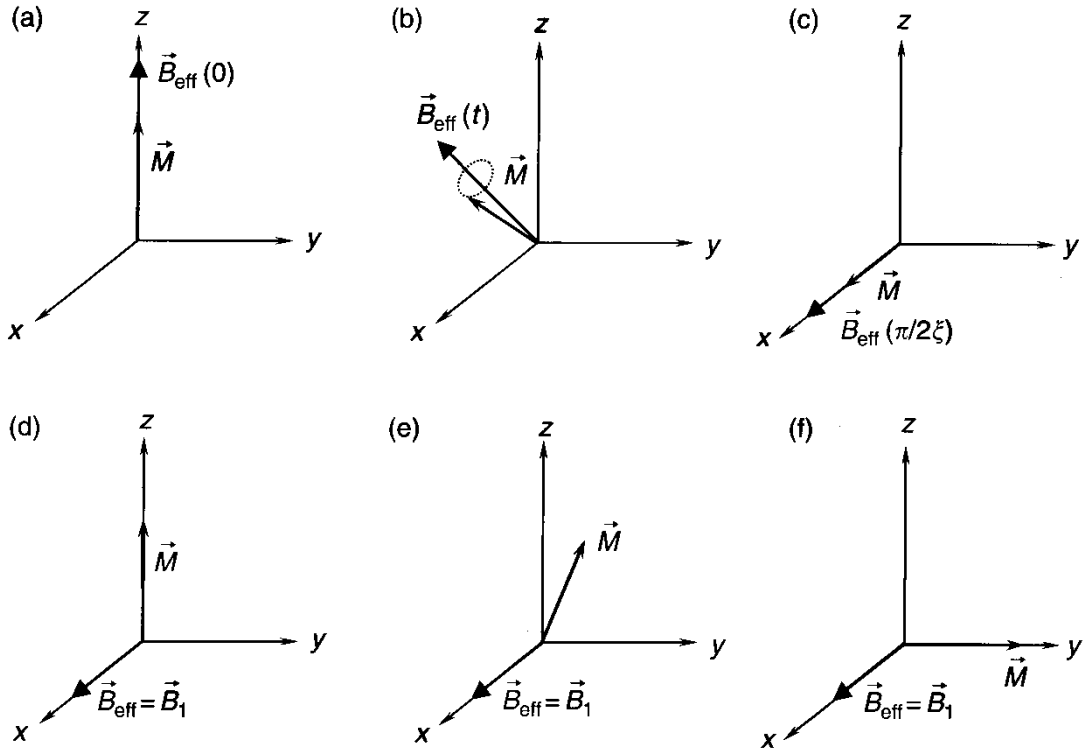

Figure 2.4.: (a-c) The adiabatic excitation process and (d-f) the non-adiabatic excitation process. The figures in each row show the magnetisation vector $\boldsymbol{M}$, the effective magnetic field $\boldsymbol{B}_{eff}$, and the applied RF field $\boldsymbol{B}_1$ throughout the course of an excitation pulse. (a) Beginning of an adiabatic pulse; (b) during the adiabatic pulse, showing the magnetisation precessing in a tight cone about the effective field; and (c) the end of the adiabatic pulse. (d) Beginning of a non-adiabatic pulse, (e) during the non-adiabatic pulse (assuming the spins are on-resonance), and (f) the end of the non-adiabatic pulse. Reproduced from [7].

2.5. Excitation and inversion pulses

Adiabatic pulses are very suitable for B_1 independent excitation and inversion, or the transformations $\boldsymbol{z} \rightarrow \boldsymbol{x}$ (or $\boldsymbol{y}$) and $\boldsymbol{z} \rightarrow -\boldsymbol{z}$.

Let us consider a pulse defined by the following modulation functions:

$$A(t) = B_x(0)\sin(\xi t) \tag{2.13}$$

$$\omega_{RF}(t) = \omega - \gamma B_z(0)\cos(\xi t) \tag{2.14}$$

ξ is the modulation frequency, B_x and B_z are time independent components of the magnetic field.

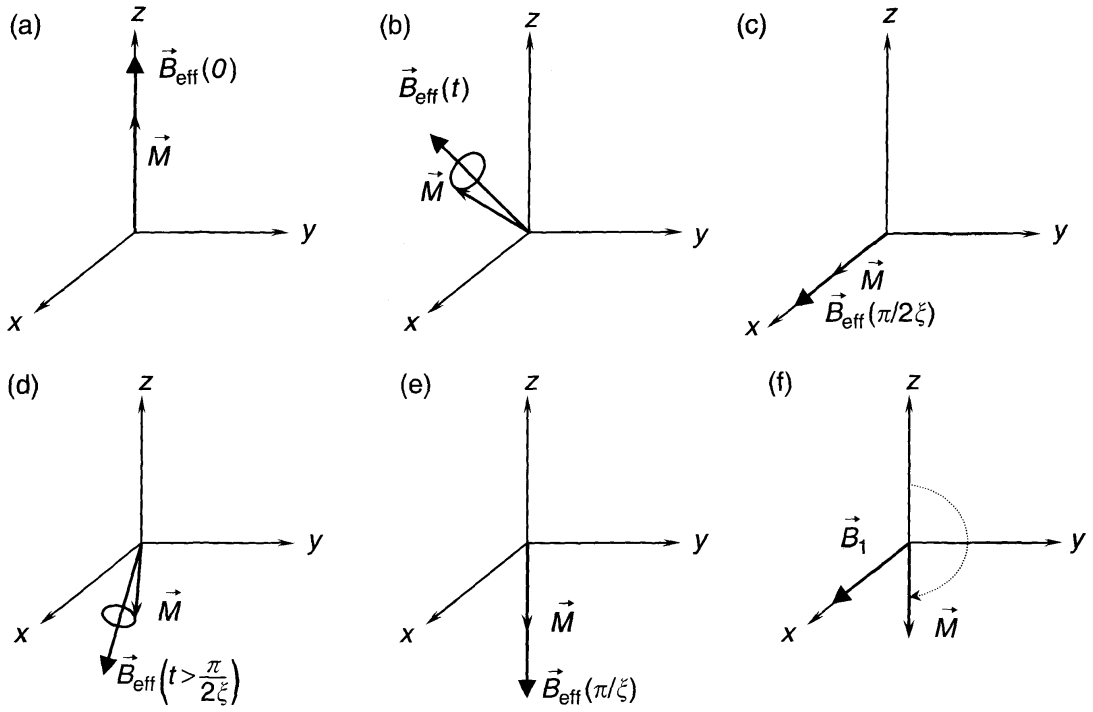

Figure 2.5.: The inversion processes in (a-e) an adiabatic pulse and (f) a non-adiabatic pulse. (a) Beginning of the adiabatic inversion pulse; (b) during the first half of the adiabatic pulse, showing the magnetisation precessing in a tight cone about the effective field (the size of the cone is exaggerated for better visualisation); (c) at the mid-point of the adiabatic pulse; (d) during the second half of the adiabatic pulse; (e) at the end of the adiabatic pulse. (f) The trajectory of the magnetisation $\boldsymbol{M}$ of non-adiabatic pulse. Note that for adiabatic inversion, the magnetisation vector $\boldsymbol{M}$ is approximately parallel to the effective field $\boldsymbol{B}_{eff}$ during the pulse, whereas for non-adiabatic inversion $\boldsymbol{M}$ is perpendicular to the applied $\boldsymbol{B}_1$ field. Reproduced from [7]

Using equations (2.5) – (2.8), the amplitude and direction of the effective field are given by

$$B_{eff} = \sqrt{(B_x(0)\sin(\xi t))^2 + (B_z(0)\cos(\xi t)^2} \tag{2.15}$$

$$\psi = \arctan\left(\frac{B_x(0)\sin(\xi t)}{B_z(0)\cos(\xi t)}\right), \tag{2.16}$$

respectively. At the beginning of the pulse ψ is close to 0 and the effective filed is aligned with the $\boldsymbol{z}$ axis and the longitudinal magnetisation. If the adiabatic condition is satisfied, which can be achieved by choosing a sufficiently low modulation frequency ξ or a strong effective field, the adiabatic passage principle dictates that the magnetisation vector will follow the direction of the effective field $\boldsymbol{B}_{eff}$ during the course of the pulse.

Figure 2.4 illustrates how the field and magnetisation vectors propagate throughout an adiabatic as well as during a conventional RF pulse.

At time point $t = \pi/(2\xi)$, $\boldsymbol{B}_{eff}$ has rotated from the $\boldsymbol{z}$ axis to the $\boldsymbol{x}$ axis, and so has the magnetisation. If the RF pulse is terminated at this point, one has achieved adiabatic excitation. The instantaneous flip angle at any moment during the pulse can be approximated by the instantaneous value of ψ. Consider two locations A and B relative to the coil with local magnetic fields $\boldsymbol{B}_{1,A}$ unequal $\boldsymbol{B}_{1,B}$. At the end of the pulse, at $t = \pi/(2\xi)$, $\boldsymbol{B}_{eff}$, $\psi = 90\,^\circ$ the effective field will be aligned with the $\boldsymbol{x}$ axis in both locations. This is why the excitation is independent of the local B_1 field as long as both $\boldsymbol{B}_{1,A}$ and $\boldsymbol{B}_{1,B}$ are sufficiently strong to satisfy the adiabatic condition (2.9).

If the application of the pulse continues until $t = \pi/\xi$, ψ changes from $90\,^\circ$ to $180\,^\circ$. The effective magnetic field $\boldsymbol{B}_{eff}$ has experienced a $180\,^\circ$-rotation. Because the magnetisation vector tracks the effective field, the magnetisation is inverted from z to $-z$. Compared to conventional pulses, where the magnetisation is always perpendicular to the $\boldsymbol{B}_1$ field, the trajectory of the magnetisation is quite different.

The adiabatic half passage (AHP) or excitation pulse is a non-selective pulse. Its excitation profile is asymmetric, because the pulse itself is asymmetric in time. The effective bandwidth is B_1-dependent. This is completely different for the adiabatic full passage (AFP) or inversion pulse. Its inversion band is well defined. Depending on the modulation functions, the transition can be very sharp. This usually goes along with a reduced bandwidth.

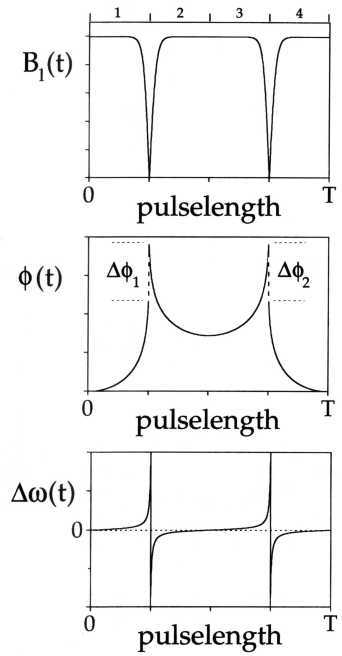

Figure 2.6.: Amplitude (top), phase (middle) and frequency modulation (bottom) of a BIR-4 pulse. Reproduced from [6]

2.6. Plane rotation pulses (BIR-4)

The adiabatic pulses so far are very useful for excitation and inversion of longitudinal magnetisation. Adiabatic excitation pulses work only if the initial magnetisation is aligned with the static field. Any transverse components would fan out about the $\boldsymbol{B}_{eff}$ field.

Refocusing magnetisation with adiabatic inversion pulses is not as such possible because the – initially transverse – magnetisation acquires a B_1 dependent phase (2.12). This phase, however, cancels out by applying the same pulse twice.

A more general and convenient solution are the so called $\boldsymbol{B}_1$–*independent plane* ***r****otation*

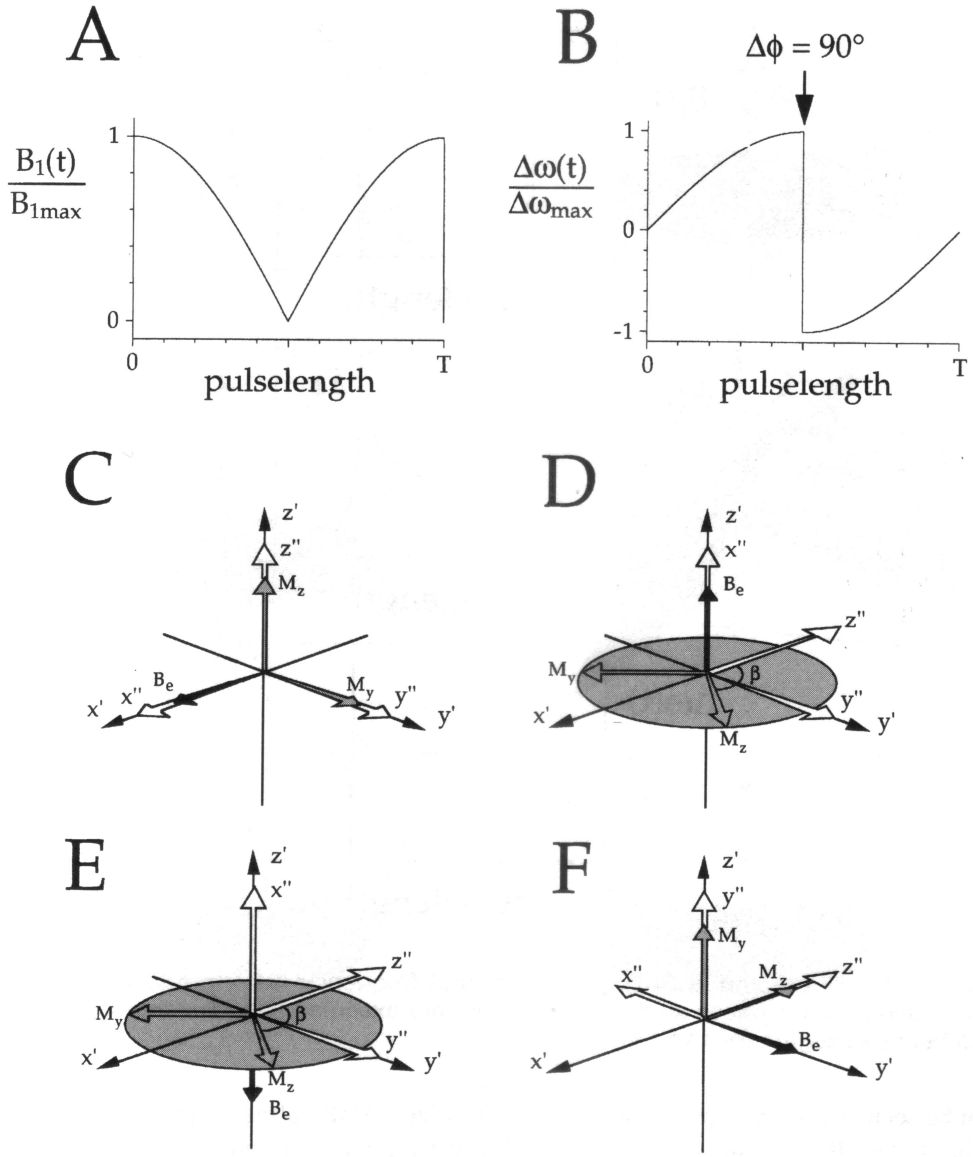

Figure 2.7.: Description of a BIR-1 pulse. (A-B) Normalised RF amplitude and frequency modulation of the pulse. (C-F) The effective field $\boldsymbol{B}_{eff} = \boldsymbol{B}_e$ starts along the $\boldsymbol{x}$ axis and rotates towards the $\boldsymbol{z}$ axis. At the midpoint of the pulse it is flipped instantaneously to the $-z$ axis from which it rotates to the $\boldsymbol{y}$ axis because it is 90 ° phase shifted to achieve excitation. $\boldsymbol{M}_x$ is initially parallel to the $\boldsymbol{B}_{eff}$ field and precesses about it in a tight cone throughout the pulse. Halfway through the pulse $\boldsymbol{M}_y$ and $\boldsymbol{M}_z$ are dephased by an angle β during the first segment. The $\boldsymbol{B}_{eff}$ inversion causes $\boldsymbol{M}_y$ and $\boldsymbol{M}_z$ to acquire a rotation $-\beta$ during the second half of the pulse, thereby eliminating the phase dispersion. Reproduced from [6].

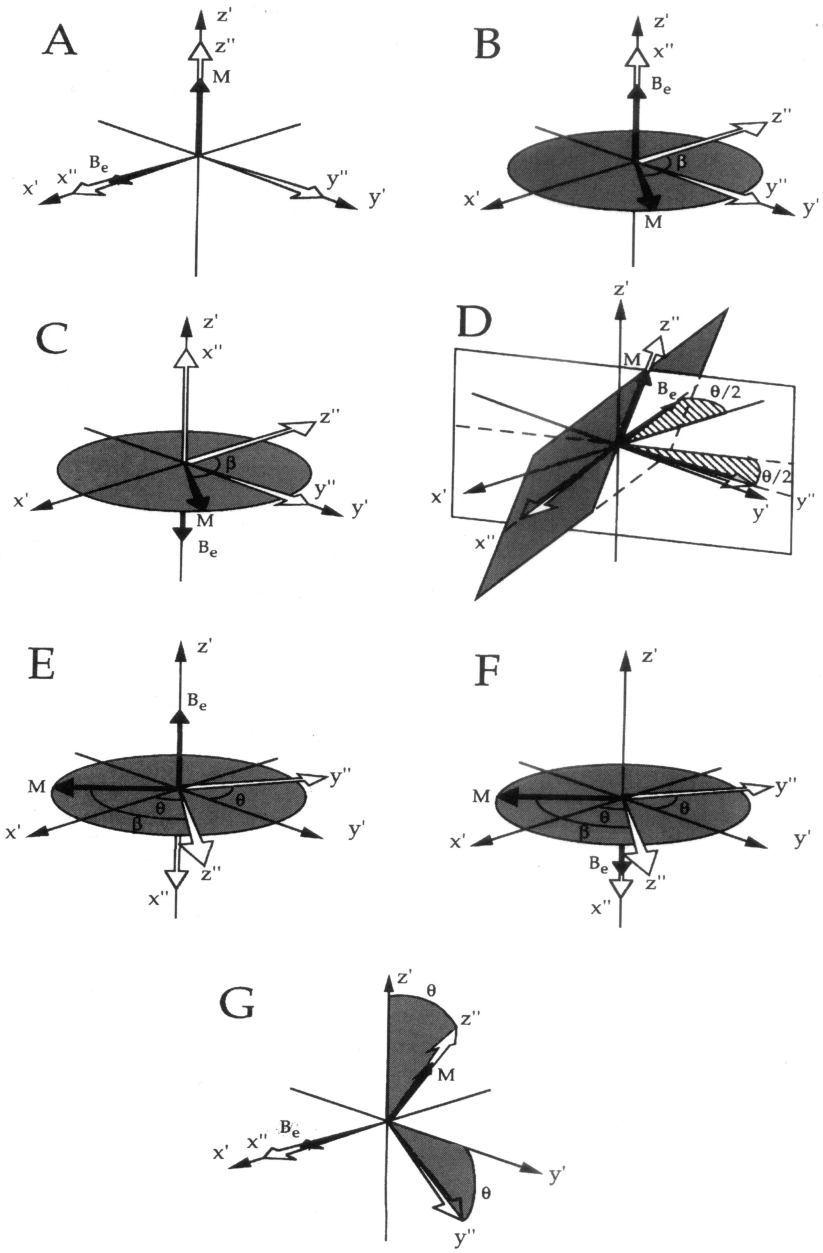

Figure 2.8.: BIR-4 pulse rotation. $\boldsymbol{B}_{eff} = \boldsymbol{B}_e$ starts in the $\boldsymbol{x}$ axis (A), rotates towards the longitudinal axis (B), is inverted along with a phase shift $\Delta\Phi_1$) (C), rotates back to the positive $\boldsymbol{z}$ axis, (D-E), is inverted again (F) with a phase shift $\Delta\Phi_2$ and rotates finally back to the $\boldsymbol{x}$ axis. The sum of the angles $\Delta\Phi_i$ determine the nutation angle of the magnetisation. Reproduced from [6].

pulses (BIR) [8]. There are several implementations, like BIR-1, BIR-2, and, most frequently used, BIR-4 [9,10]. They have in common that they consist of several elements. These are adiabatic excitation – or half passage – pulses and their time reversals, with phase discontinuities at the junction points. It is these phase jumps that determine the flip angle.

Plane rotation requires that at the end of the pulse the accumulated angle β equals 0. This can be achieved by inverting $\boldsymbol{B}_{eff}$ during the pulse. The nutation angle of the pulse is introduced by a phase shift of the $\boldsymbol{B}_1$ field immediately after the $\boldsymbol{B}_{eff}$ inversion.

The BIR-1 pulse consists of a time-reversed AHP followed by an AHP. In the case of the time reversed AHP, $\boldsymbol{B}_{eff}$ starts from an axis in the transverse plane and ends along the $\boldsymbol{z}$ axis. In case of a sin / cos pulse, the amplitude and frequency modulation of the pulse looks like

$$\boldsymbol{A}(t) = \begin{cases} B_1 \boldsymbol{x} \cos(\xi t) & (0 \le t < T/2) \\ B_1 \boldsymbol{y} \cos(\xi t) & (T/2 < t \le T/2) \end{cases} \tag{2.17}$$

$$\omega_{RF}(t) = \begin{cases} \omega - \gamma B_{1,z}(0) \sin(\xi t) & (0 \le t < T/2) \\ \omega + \gamma B_{1,z}(0) \sin(\xi t) & (T/2 < t \le T/2). \end{cases} \tag{2.18}$$

B_1 is the peak amplitude of the pulse of length $T = \pi/\xi$. $\boldsymbol{x}$ and $\boldsymbol{y}$ are unit vectors in the direction of the respective axis. At $t = T/2$ a 90 ° phase shift occurs as can be seen in (2.17). The phase shift can be set to a different value and thereby alter the flip angle of the pulse.

The effective magnetic field starts parallel with the $\boldsymbol{x}$ axis and moves in the xz plane towards the $\boldsymbol{z}$ axis where it arrives at $t = T/4$. Then the effective field $\boldsymbol{B}_{eff}$ moves in a plane that is rotated by the angle $\Delta\Phi$ relative to the xz plane. See also Figure 2.7 for further description.

Unfortunately, the BIR-1 pulse has a poor off-resonance behaviour. The more robust and most frequently used adiabatic plane rotation pulse is the BIR-4 pulse. In case of tanh / tan modulation functions the shape of the pulse is given by:

$$A(t) = \begin{cases} B_1 \tanh[\lambda(1 - 4t/T)] & (0 \le t < T/4) \\ B_1 \tanh[\lambda(4/T - 1)] & (T/4 \le t < T/2) \\ B_1 \tanh[\lambda(3 - 4t/T)] & (T/2 \le t < 3T/4) \\ B_1 \tanh[\lambda(4t/T - 3)] & (3T/4 \le t \le T) \end{cases} \tag{2.19}$$

$$\omega_{RF}(t) = \begin{cases} \omega - \frac{\tan[4\beta t/T]}{\tan\beta} & (0 \le t < T/4) \\ \omega - \frac{\tan[4\beta(4t/T-2)]}{\tan\beta} & (T/4 \le t < T/2) \\ \omega - \frac{\tan[4\beta(4t/T-2)}{\tan\beta} & (T/2 \le t < 3T/4) \\ \omega - \frac{\tan[4\beta(4t/T-4)]}{\tan\beta} & (3T/4 \le t \le T) \end{cases} \tag{2.20}$$

β and λ are dimensionless constants that determine how well the pulse satisfies the adiabatic condition. Very important are the phase shifts $\Delta\Phi_1$ at $t = T/4$ and $\Delta\Phi_2$ at

$t = 3T/4$. The desired flip angle is given by

$$\Delta\Phi_1 = \pi + \frac{\theta}{2} \tag{2.21}$$

$$\Delta\Phi_1 = -\pi - \frac{\theta}{2}. \tag{2.22}$$

Alternatively, the middle part of the pulse can be seen phase shifted by $\Delta\Phi = \pi + \frac{\theta}{2}$ relative to the outer segments. The typical shape of the pulse is seen in Figure 2.6. The trajectories the $\boldsymbol{B}_1$, $\boldsymbol{B}_{eff}$ fields and the magnetisation follow is displayed in Figure 2.8.

2.7. Modulation functions

Adiabatic pulses can be generated with a wide range of amplitude and frequency modulation functions. How well the adiabatic condition is fulfilled throughout the pulse and for up to which frequency offset, however, is determined by their shape. This will strongly influence the selectivity, bandwidth and power requirements of the pulse.

Ideally, the pulse should have constant amplitude and frequency sweep rate over the operational band to ensure that all spins, regardless of their frequency offset experience the same adiabaticity factor at resonance. The sweep has to end at some finite offset, however, it is important to bring down the amplitude smoothly to zero to satisfy the adiabatic condition [11]. The AFP thus have an amplitude modulation that starts and ends at zero and reaches its maximum at $t = T/2$. The frequency starts at either $\pm\omega_{RF,max}$, usually changes fastest halfway through the pulse and reaches $\mp\omega_{RF,max}$ at the end.

A hyperbolic secant (sech / tanh modulated) [12,13] pulse will have a sharper frequency profile than a tanh / tan modulated pulse, which, in turn, has a much higher bandwidth. The sin / cos pulse is somewhere in between.

To evaluate modulation functions, the adiabatic condition can be expressed explicitly. For a sech / tanh AHP pulse

$$\begin{aligned} \boldsymbol{B}(t) &= B_1 \operatorname{sech}(\beta(1 - t/T))\boldsymbol{x} \\ \omega_{RF}(t) &= \omega_{RF,max} \tanh(\beta(1 - t/T))\boldsymbol{x} \end{aligned} \qquad 0 \le t \le T \tag{2.23}$$

(2.9) becomes

$$1 \ll \left| \frac{\gamma B_{eff}(t)}{d\psi/dt} \right| = \frac{\omega_{RF,max}^2 T}{\beta B_1 \operatorname{sech}[\beta(1 - t/T)]} \sqrt{\left[\frac{\gamma B_1}{\omega_{RF,max}} \operatorname{sech}[\beta(1 - t/T)] \right]^2 + \tanh[\beta(1 - t/T)]^2}. \tag{2.24}$$

Evaluating the adiabatic conditions for potential modulation functions, it is possible to construct optimised functions that operate over predefined B_1 and $\omega_{RF,max}$ ranges. The generation of modulation functions can be even generalised to families of functions

and then the adiabaticity factor η is set to a minimum value and the inverse of 2.9 is taken to determine the parameters. Numerous optimised pulses have been generated that way [10, 14–17], but going into further details is beyond the scope of this work.

3. Human Energy Metabolism

The human body relies on a steady supply of energy in the form of nucleotide triphosphate (NTP), primarily in the form of adenosine triphosphate (ATP). The primary source of energy is oxidation of ingested nutrients, either carbohydrates, proteins or fats. The intestine extracts sugars, amino acids and fats from food after meals. Excess nutrients are stored in the liver, skeletal muscle and adipose tissue for later usage. The nutritious state interacts directly with anabolic hormones, like insulin, and catabolic hormones, like glucagon, to meet the immediate needs and stabilise plasma levels of glucose or fatty acids.

Skeletal muscles form a large part of the body mass and play an important role in the regulation of the nutritious state of the organism. It is the primary target of insulin which leads to glucose uptake after meals to either oxidate it or to form glycogen, if supplies exceed momentary demands. Glycogen in muscle is stored for its own usage only, no glucose can be released into the bloodstream to maintain constant plasma glucose levels during fasting.

In resting state or moderate action, energy demands of the muscle is met by oxidating fat in the citric acid cycle (TCA cycle) in the mitochondria. At higher workload glucose is reduced to pyruvate which, if oxygen supply is not limited, is burned in the TCA cycle, or lactate is formed. If immediate energy demands are very high, phosphocreatine (PCr) replenishes ATP stores.

The liver is also very important in maintaining a healthy state of the body, most importantly maintaining normal plasma glucose levels. This is done by storing large quantities of glycogen from carbohydrate food sources, and later releasing it back to the plasma. The liver also forms glucose from amino acids or other three carbon molecules like lactate. Unlike many other tissues the liver does not use phosphocreatine as a storage.

Whatever the source of energy is and what tissue it uses, the final form that catalyses energy demanding reactions is as nucleotide triphosphate (NTP), most often as (ATP). A simplified picture of the metabolic pathways is shown in Figure 3.1. The core of all major pathways is the tricarboxylic acid cycle. Although it is not shown in the figure, also amino acids can enter the TCA cycle for oxidation.

Living tissues are very dynamic and open systems. Cellular properties may appear constant, due to strong feedback loops but many times they rather are in a dynamic equilibrium. A typical example may be the concentration of intra- and extracellular sodium or potassium. Under normal conditions these levels are kept constant by active ion pumping requiring ATP, whose stores in turn are replenished all the time. This means that metabolite concentrations do not tell us the whole story. Additional dynamic information should be gathered. NMR is capable of supplying such information. This

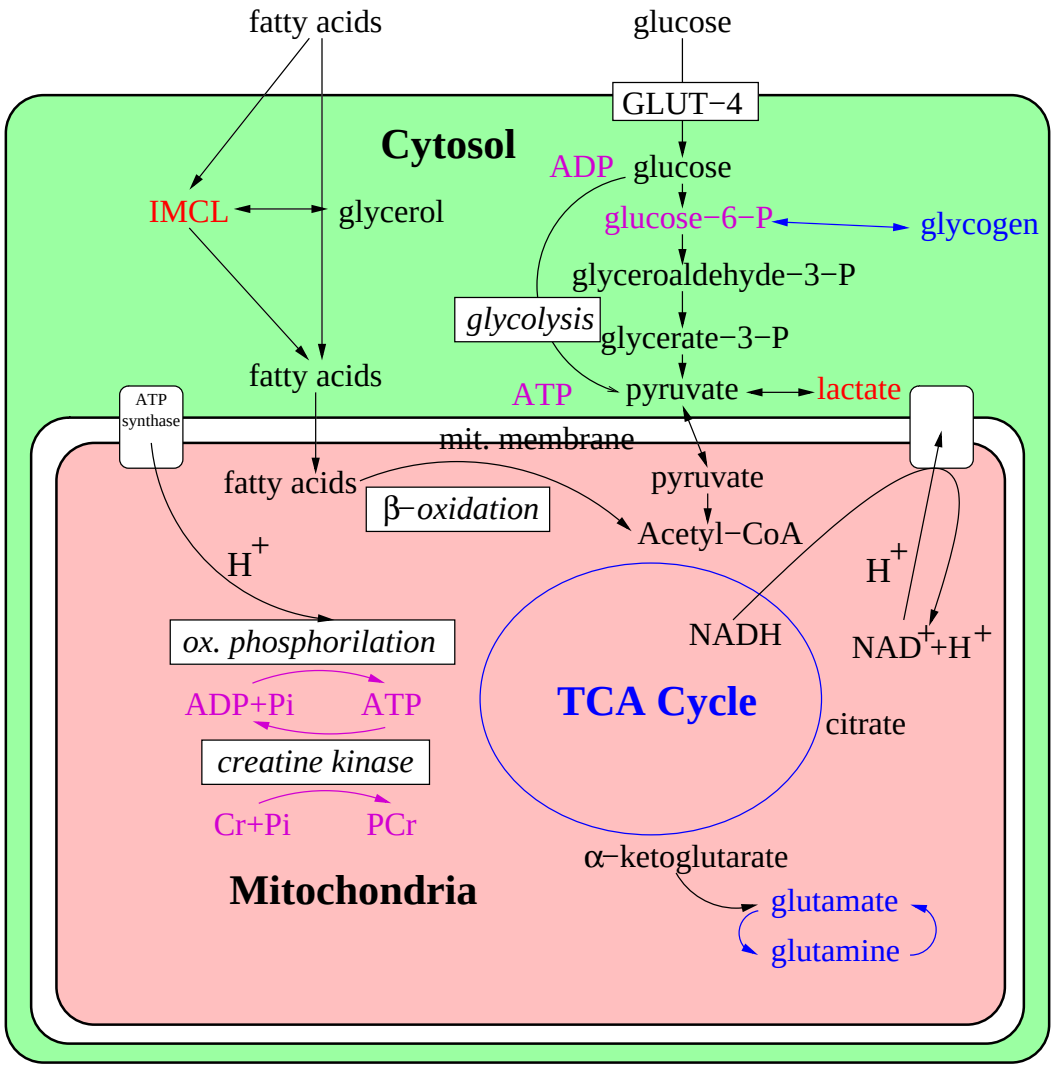

Figure 3.1.: Schematic and simplified description of cellular energy metabolism of a muscle cell. The cellular compartmentation between the cytosol (green) and mitochondria (pink) is of great importance to the reactions. Substrates in the form of fatty acids or glucose enter the cell or are released from intracellular stores (IMCL or glycogen). Fatty acids are cut into C-2 pieces by β-oxidation in the mitochondria which enter the TCA-cycle in the form of Acetyl-CoA. Glucose is phosphorilated and broken down into pyruvate which enters the mitochondria and the TCA-cycle. Several processes in the citric-acid cycle produce free protons which are transferred to the inter-membrane space of the mitochondria. These protons are used by ATP synthase to form ATP from ADP and inorganic phosphate in exchange for transporting protons back into the mitochondria. The colours indicate the accessibility by in-vivo NMR spectroscopy: by ^{1}H MRS in red, ^{31}P in magenta and ^{13}C in blue. Coloured text indicates that the metabolite is visible in the spectra. Coloured arrows indicate that the respective flux is measurable.

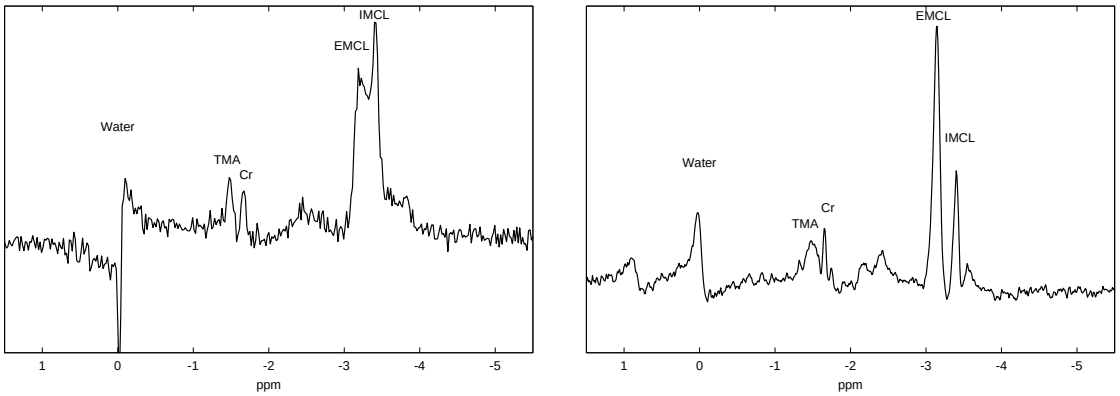

Figure 3.2.: Water suppressed proton spectra acquired at 3 T. A $(12\,\mathrm{cm})^3$ volume of interest was selected by a STEAM sequence ($T_E = 20\,\mathrm{ms}$, $T_M = 30\,\mathrm{ms}$, $T_R = 4\,\mathrm{s}$. Left: Spectrum from soleus muscle, 32 averages; right: Spectrum from tibialis anterior muscle. 64 averages. The shift of the EMCL peak is more pronounced in tibialis anterior than in soleus.

is indicated by coloured arrows in Figure 3.1.

The state of the nuclear spin is not altered directly when the chemical environment changes. This means that if the nucleus in question is part of chemical substance A during excitation and later on moved into substance B by some chemical reaction, the spin is still excited and may be detected at resonance frequency of substance B, neglecting relaxation.

MRS has large VOIs compared to the size of cells, sometimes there are even different tissue types involved. The detected signal therefore contains a mixture of contributions originating from different compartments. This can be a problem sometimes, additional information on the involved tissues is required to assign the signals unambiguously.

The following sections try to illustrate the relevance of NMR in general and multinuclear MRS in particular for clinical application and research.

3.1. Skeletal Muscle MRS

Skeletal muscle MRS was among the first applications of MRS to humans in-vivo [18,19]. The technical development of NMR scanners was dramatic since these early experiments. High static field strengths are available for human whole body examination, magnetic field gradients are stronger and faster and have less eddy currents. Better shimming allows for the acquisition of high resolution and high SNR spectra.

Proton spectra of human calf muscle (soleus and tibialis anterior are displayed in Figure 3.2. The extracellular lipids are aligned about the muscle fibres. This ordering effect induces a shift of the resonance frequency. This frequency shift is depending on the angle between the static magnetic field and the muscle. Typical spectra from human skeletal muscle are displayed in the following chapters. A ^{31}P spectrum is displayed in

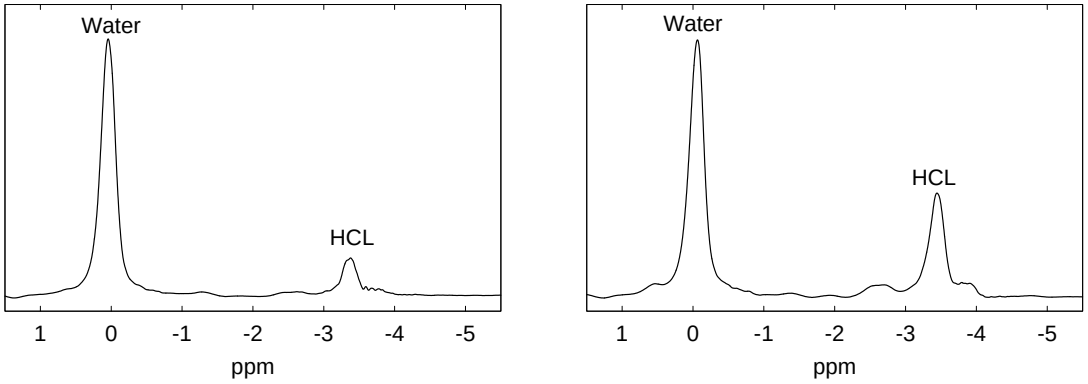

Figure 3.3.: Liver spectrum of two diabetic subjects, one with low (left) and one with high (right) HCL content.

8.2 and a ^{13}C spectrum in 7.8.

Multinuclear spectroscopy was – and continues to be – very appealing to physiologists since it allows for the direct, non-invasive observation of several important metabolites. High energy phosphates and intracellular pH, which can be determined from the chemical shift of inorganic phosphate, are bioenergetic indicators. During and after an intervention PCr. Pi and pH undergo rapid changes, usually in the order of seconds or minutes [18–20].

^{13}C spectroscopy is also very important for the assessment of human physiology, because ^{13}C spectra show glycogen and tricarboxylic acid (TCA) cycle intermediates [21–24]. Proton decoupling, which will be discussed in more detail in the next part, is almost a must for ^{13}C spectroscopy, both for signal enhancement and spectral simplification.

With proton MRS of skeletal muscle it is possible to quantify intracellular muscle fat [25–31]. Other interesting metabolites, which, however, require more sophisticated techniques to detect, include lactate [32–34] and deoxymyoglobin [35–40].

Very important is the tight relation of IMCLs and insulin resistance, i.e. how effective is insulin action on lowering the plasma glucose level, which has been shown in a number of studies [41–43]. However, a paradox exists in the picture of IMCL. High IMCL levels are not only detected in insulin-resistant subjects but also in very well-trained insulin-sensitive people [44, 45]. In overt T2DM, insulin resistance has been linked to abnormalities of muscle mitochondria [46, 47] as assessed from biopsies.

3.2. In-vivo MRS in investigating hepatobilary disease

The liver plays a central role in intermediary metabolism by regulating storage and release of carbohydrates, lipids and proteins. Increased hepatocellular lipid (HCL) content is a feature of various insulin resistant states [48, 49], correlates negatively with insulin sensitivity [50] and could even be the key factor in the development of type-2 diabetes

mellitus (T2DM) [49, 51]. In the absence of significant alcohol intake or other hepatotoxic agents, HCL accumulation is termed steatosis or non-alcoholic fatty liver (NAFL). Steatosis likely results from excessive overflow of triglycerides and free fatty acids (FFA) from lipid stores in visceral adipocytes [51] or from an imbalance of the release of pro- and anti-inflammatory adipocytokines [48, 52]. It is unclear at present, however, which cellular mechanisms cause steatosis in humans.

A typical ^{31}P spectrum is shown in Figure 8.10. It shows resonances of nucleotide-triphosphates (NTP), mostly adenosine-triphosphate (ATP), inorganic phosphate, phosphomonoesters (PME) and phosphodiesters (PDE). In-vivo ^{31}P spectroscopy revealed elevated PME/PDE ratios in various liver diseases like cirrhosis, viral hepatitis and alcohol-related liver disease [53–57]. A correlation of PME signal and the severity of cirrhosis has been demonstrated [58,59]. Cho et al. [60] found increased glutamine/glutamate, PME and glycogen/glucose resonances compared to lipids in ^{1}H spectra with increased severity of chronic hepatitis.

PME and PDE to ATP ratios were elevated in livers of subjects with chronic alcohol abuse [57], although PDE/ATP fell with chronic viral or autoimmune hepatitis [61]. Recovery from fructose induced ATP depletion is severely reduced in patients with non-alcoholic steatohepatitis (NASH) [62, 63].

In the opinion of the authors, one promising prospect for human hepatic ^{31}P MRS is the measurement of hepatic energy homoeostasis through the measurement of ATP. If hepatic energy homoeostasis can be found to correlate with global hepatic function, there could be many clinical possibilities. For example, a common and significant clinical problem arises when selecting organs appropriate for liver transplantation. Perhaps hepatic energy homoeostasis could be used to select donor organs in vivo or ex vivo, test organ preservation solutions, and predict outcomes such as primary graft non-function. [64].

Unlike many other liver function tests, MRS detects changes non-invasively in-situ. It does not depend on blood flow or assessment of plasma components which depend on liver perfusion. It is noteworthy that MRS is uniquely suited to research studies because it can non-invasively measure in-vivo biochemical processes and thus allows researches to study dynamic responses to physiologic challenges

3.3. From Nuclear Spin to Metabolic Fluxes

Let us finish this chapter with a short summary of what are the motivation behind the experiments, that will be presented in the remainder of this work.

A way to quantify TCA-cycle activity is to measure the relative ^{13}C enrichment of glutamate at the C-4 and C-2 or C-3 positions. The temporal evolution of label incorporation after ^{13}C enriched substrate administration is the basis of this model-based quantification. The chemical shift of glutamate C-2 and C-3 resonances is very similar to that of fatty acids whose signals is stronger by several orders of magnitude. It is, however, well separated in the proton spectrum. ^{13}C spectroscopy suffers primarily from its low sensitivity. Polarisation transfer is one way to enhance the signal significantly.

Compared to nuclear Overhauser (nOe) [65] enhancement, which may yield comparable signal intensities, it has the distinct advantage that the in-vivo nOe factors are almost impossible to determine accurately. Furthermore, the chemical shift displacement, when using gradient based slice-selection techniques for localisation, is very large in ^{13}C spectroscopy. Therefore, prelocalisation on the proton channel is a significant benefit. When polarisation transfer is applied a frequency selective saturation of the fatty acid signal could be possible.

Last but not least, the development of a B_1 insensitive pulse sequence is desirable since this improves the performance of the experiment significantly, especially when surface coils are used. This will be the topic of the second part, especially Chapter 7.

Oxidative phosphorilation is also a very interesting topic. The ^{31}P saturation transfer experiment has successfully been used on skeletal muscle by Petersen et al. [24, 66] and by our group [67]. In these works several important findings were made on the interaction between glucose metabolism, fatty acid metabolism, insulin resistance and mitochondrial phosphorilation. There are, however, still several experimental issues which can be improved. This includes a more sophisticated acquisition scheme to reduce the vulnerability of motion artifacts and slow drifts in e.g. phase or frequency. This increased accuracy can be traded for shorter acquisition times which are typically very long. Another matter is localisation. The first study where this improved sequences were used was published by Szendrödi et al. [68]. In this work it is treated in Chapters 8 and especially 10.

In the experiments described so far the only localisation is given by the sensitivity profile of the transmit/receive coil. This may be sufficient for measurements in skeletal muscle but for tissues like the liver it is not. his brings us to the third important goal of this work: Implementation of the ^{31}P magnetisation transfer experiment to localised hepatic in-vivo spectroscopy. Until now assumptions of ATP homoeostasis were made from studies using metabolic challenges with fructose [69,70], ethanol [71], and L-alanine [72]. Further in vitro studies in tissue extracts, cell cultures or isolated mitochondria suggested less tolerance of steatotic livers to oxidative stress and mitochondrial injury, at least when steatosis is complicated by inflammation, termed steatohepatitis. Thus, the aim of the present study was to test the feasibility of directly quantifying rates of ATP synthesis in the human liver. The prerequisite for this is a quick robust localisation scheme that yields high SNR and is only moderately susceptible to artifacts of cardiac and respiratory motion. The direct measurement of hepatic ATP production has not yet been reported in-vivo. The only work so far was on perfused isolated rat livers [73]. The experimental ingredients and preliminary results, which are going to be published [74], are described in Chapters 8, 9, 11 and 12. The possibility to quantify hepatic rates of oxidative phosphorilation in-vivo is not only interesting to diabetologists but also for the study and diagnosis in diffuse liver disease, for transplantation to test the functional integrity of the tissue and possibly for oncologists.

Summarising, the motivation of this work is to improve NMR experiments addressing mitochondrial function, to supply the sometimes sophisticated and specific adaptations of basic experiments required for these measurements. Two parameters that are exclusively accessible by MRS in-situ are the measurement of TCA cycle activity and ATP

synthesis. With the help of this work it will be possible to successfully perform these experiments.

4. Experiments

4.1. Hardware Setup

Figure 4.1.: The NMR scanner where all measurements for this work were performed.

The NMR experiments that will be presented in the following chapters of this work were implemented and performed using a 3 T whole body magnet. The diameter of the inner bore of the gradient system was 55 cm. The system is equipped with electronics of a BRUKER MEDSPEC S300 system, (Bruker Biospin, Ettlingen, Germany). The whole body gradient coils in $\boldsymbol{x}$, $\boldsymbol{y}$, and $\boldsymbol{z}$-directions allow for B_0 modulations of up to 45 mT/m with a ramp time of 420 μs.

The system is equipped with two completely independent radiofrequency transmit units. This is important if simultaneous irradiation at different frequencies is desired. A 4 kW amplifier is available for transmission at the proton resonance frequencies and a 1 kW broadband amplifier for irradiation for other nuclei like ^{13}C ^{31}P or ^{23}Na.

Only a single receive channel is available. The preamplifier, however, and filters can be selected by respective wiring of a switch box that is set between the transmitter and receiver electronics and the coil connector.

The radiofrequency coils used throughout this work were 10 cm, linear polarised, double resonance surface coils, tuned to the proton frequency and either the resonance frequency of ^{13}C or ^{31}P. The impedance and resonance frequency of the coil were fine-tuned for each subject or phantom for an optimal transition of the radiation between tissue and the coil.

4.2. Research on Human Subjects

All investigations involving human subjects were performed only with the informed written consent of the participants and after approval by the ethics committee of the Medical University of Vienna. This procedure is in accordance with the Helsinki (June 1964) declaration on the Ethical Principles for Medical Research Involving Human Subjects of the 18^{th} world declaration of the World Medical Association.

The potential risks of nuclear magnetic resonance can be divided into those generated by the static magnetic field, magnetic field gradients and those of the radiofrequency pulses.

The primary source of danger is the strong attractive force of the magnet on any magnetic material, in particular iron or steel objects. It is inevitable for the safety of the volunteers and the operating personnel to be free of such materials and not bring them close to the scanner. Therefore one has to be sure that the subjects do not have metallic splinters, nails, plates or similar in their bodies from previous injuries.

Another important matter is the danger of excessive tissue heating by radiofrequency fields. There are very restrictive limits on the transmitted power to prevent excessive energy absorption. The NMR system has builtin security measures that prevent tissue damage under normal conditions. Conducting materials, however, could absorb more heat thus damaging adjacent tissue. Typical cases are metallic particles in tattoos or cosmetics, electrodes or other metallic parts, for example encountered in implanted medical devices.

There is also a "secondary" risk of damage to some live-supporting devices like a cardiac pacemaker by the magnetic field. Therefore, scans of patients with such devices should not be performed.

4.3. Implementation and Pulse Programming

The experiments are controlled via ParaVision software package (Bruker Biospin, Ettlingen, Germany). This package, with the XWIN-NMR software package in the background, allows setup and execution and data reconstruction of imaging and spectroscopy measurements. Many commonly used methods are already implemented, yet more sophisticated experiments require interaction of the researcher and the system on a deeper level, up to programming a complete new pulse sequences. This is described in the rest of this section.

In general, before a scan is started, all necessary parameters are translated from physically meaningful units into parameters meaningful to the individual electronic components and loaded into the control unit.

The most central element is the so called pulse program. Basically, it is a temporal sequence of commands to be executed, or a delay optionally followed by action(s), i.e. switch the x-gradient to 40% for 4 ms, then turn it off, start the ADC, sample for 200 ms then stop it, etc. This pulse program is execute until all the required acquisitions have been done, then the scan is finished and the data reconstructed.

4.3.1. The Structure of Acquisition in ParaVision

Basically, there are two levels at which the user can interact with ParaVision, the software provided by the manufacturer to operate the scanner. The more "physical", intuitive top level, IMND[1] , or if newer protocols PVM (ParaVision Method), and the level of ACQP (ACQuisition Parameters), that in terms is strongly related to the electronic implementation of the acquisition process. That means, for example, on IMND level one can set geometric parameters in physical units, like a 30 mm saturation slice or a cubic voxel of $12 \times 12 \times 12$ mm. This, in terms, will be translated into (relative) gradient strengths and frequency offsets, that, alternatively, are directly accessible via ACQP.

Once the experiment is started, the pulse program is executed sequentially. In most cases, each line starts with a delay during which the action following the delay on the same line will be executed.

Conditional execution is possible with `if` statements. Loops are other common elements of the pulse program. Text following a `;` are treated as comments and ignored. As an example the pulse program for a pulse acquire experiment is displayed.

```
;
; simple working pulse program for a pulse-acquire experiment.
;
#include <DBX.include>; include other files

#include <MEDSPEC.include>
"d5=d4+100u" ; numeric calculations are possible.

start,  d0    ; entry point, d0 usually is the recovery delay
if (ACQ_trigger_enable)  ; if external triggering is enabled, wait for it.
{
10u   setnmr3|8
10u   trigpl1
10u   setnmr3^8 d7
}
100u    fq1:f1 ; sets frequency channel 1 (f1) to the next value in
```

[1] It was impossible to find out what these letters stand for; rumours have it that even at the manufacturer the definition has been lost.

```
; frequency list 1 (acqp ACQ_O1_list)
d8  gatepulse 1 ; makes it effective
p1:sp0          ph0  ; perform the excitation pulse,
; duration p1 (acqp P[1]), shape sp0 (acqp TPQQ[0]) and phase ph0
3.5u
if (Coil_operation &=&  Cross_Coil) ; do some coil-specific stuff.
{
2m grad{(80)|(0)|(0)} ; a gradient in slice direction with 80% strength.
d4 groff ; gradient off
}
1.5u            ph2
10u:e   syrec  ; switch to receiver
aqq     adc     ph0  ; start the ADC with the same phase
; as the excitation pulse and collect data during time aqq.
10u
2.5274m eoscnp  ; switch back to transmit
2.5u         ipp0  ; jump to next value of phase list ph0
lo to start times NS  ; jump to start until NS scans performed.
5u         rpp0  ; reset phase list ph0
goto start  ; for repeated experiments jump back
exit
ph0 = 0 2 1 3  ; phase list. values are multiples of 90 degrees$
ph2 = 0
```

While IMND is more intuitive to use in the first place, any changes exceeding the most basic ones of an existing pulse sequence requires rewriting complex C++ code. The pulse program is plain text and almost all parameters can be set in ACQP directly, this allows programming and debugging on the fly, no compiler is needed. Thus, after loading a suitable dummy method, modifications were done in ACQP. Parameters may be set interactively or through macros or scripts, which was used extensively.

4.4. Localisation and the X–nuclei

A short overview by what means the magnetisation can be localised shall be given here. First of all, any signal can only be detected within the sensitive volume of the coil. For many applications this is a sufficient localisation, especially if a surface coil is used. The volume of interest may be further confined by choosing an appropriate B_1 strength. For example, the flip angle of the excitation pulse at the coil centre may be around 180 °, enhancing the relative contribution of tissue further away from the coil.

This very simple method can be used where contaminations from surrounding tissue is negligible or their contribution is at least tolerable. If, however, tissue specificity is of greater importance, more sophisticated methods have to be used. Here, the $\boldsymbol{B}_0$ gradients come into play.

Table 4.1.: Some important acquisition (`acqp`) parameters. The names are of many parameters are different in `acqp` than they are in The pulse program. The elements column tries to describe the structure of the parameter, e.g. gives the dimension if it is an array or the elements' names in a structure.

Parameter in `acqp`	in pulse program	Elements	Description
PULPROG	-	-	name of the pulse program
GRDPROG	-	-	name of the optional gradient program
ACQ_ns	NS	-	number of scans – FIDs will be added
NI	NI	-	number of images – scans be stored consecutively
NAE	NAE	-	nr. of averages exp. – accumulates every NI
NR	NR	-	number of repetitions – repeats the whole experiment and stores it consecutively
D	dn	32	a delay [s]
ACQ_vd_list	vd	-	a variable delay (vd) and the list to feed it (ACQ_vd_list
ACQ_vp_list	vp	-	a variable length hard pulse (vp) and the list to feed it (ACQ_vp_list
P	pn	32	shaped pulse length [μs]
PL	pl$n$	32	hard pulse power level [μs]
TPQQ	sp$n$	16 x (shape,max. power,frequency offset)	shaped pulses n is 1-8 and 17-24
DPQQ	sp$n$	16 x (shape,max. power,frequency offset)	shaped pulses n is 9-16 and 25-32
BFn, SFOn	-	8	Basic frequency without/with global adjustment
ACQ_On_list	fq$n$	one list per basic frequency	Frequency offset list relative to basic frequency
-	fq$n$	1 or 2	frequency channel. 2 transmitter, 1 receiver
-	ph$n$	-	phase list
ACQ_size/SW_h	aqq	-	Acquisition time; is acquisition size over sweep width

4.4.1. PRESS and STEAM

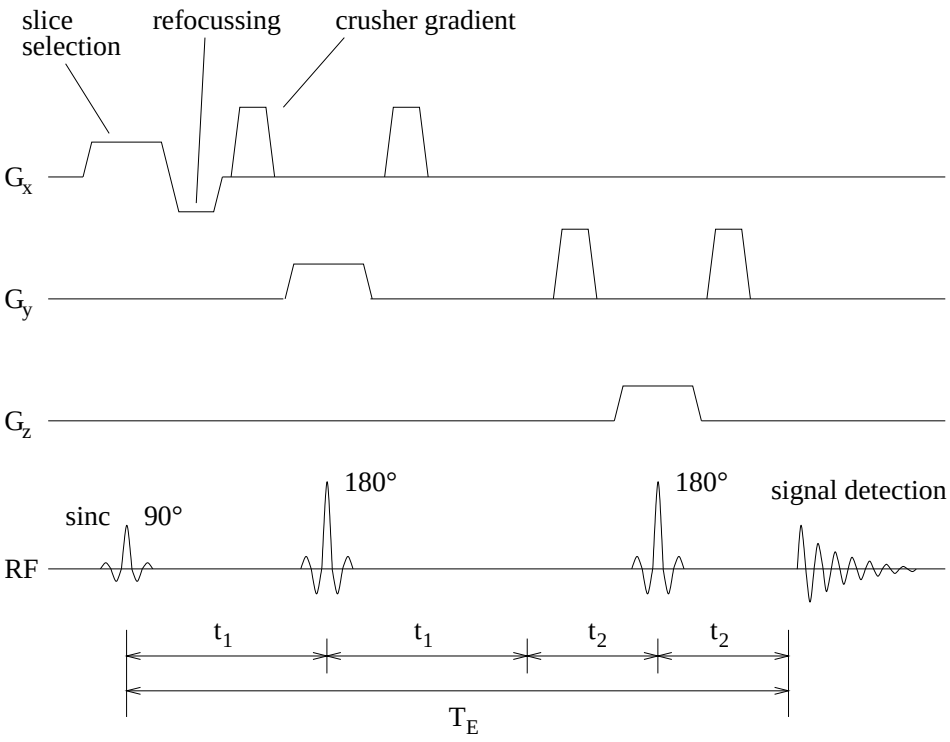

Figure 4.2.: Point resolved spectroscopy pulse sequence [75]. In a PRESS experiment the signal of the second spin echo is acquired. The excitation pulse and the two refocusing pulses are slice selective with the slices orthogonal to each other. Thus, the signal which is refocused at the top of the second echo comes from the cuboidal intersection of the three slices. The two echo times need not be equal. For coupled spin systems a proper selection of the timing greatly influences the observed signal. The figure is reproduced with friendly permission from Martin Meyerspeer.

The most common echo-based localisation schemes are **P**oint **RES**olved **S**pectroscopy (PRESS) [75] and **ST**imulated **E**cho **A**cquisiton **M**ode (STEAM) [76], both use three frequency selective pulses with simultaneous slice selection gradients for spatial encoding in the three spatial directions.

PRESS is basically a double spin echo, see Figure 4.2, while the evolution of the magnetisation in STEAM is more complicated. In contrast to PRESS, the signal observed in STEAM is a stimulated echo. Only one half of the magnetisation is refocused at the top of the stimulated echo. During the so called mixing time T_M the part of the magnetisation that is going to be refocused is aligned with the longitudinal axis, thus not subject to transversal relaxation.

With STEAM it is, in general, possible to use shorter echo times than with PRESS. With our hardware setup an echo time below 10 ms is possible. Also, 180 ° pulses are

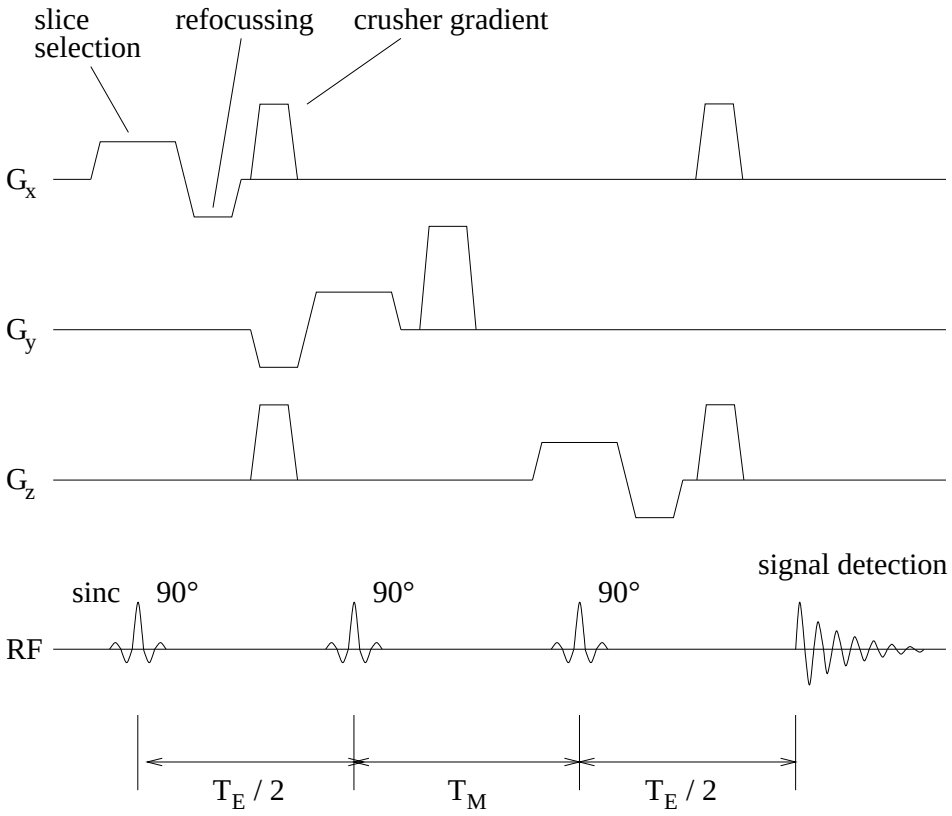

Figure 4.3.: Stimulated echo acquisition mode pulse sequence. The figure is reproduced with friendly permission from the thesis of Martin Meyerspeer.

more susceptible to imperfections than the 90 ° pulses and generate more SAR. Thus, STEAM is often preferred over PRESS despite the fact that it yields theoretically only 50 % of the signal.

4.4.2. ISIS

Image **S**elected **I**n-vivo **S**pectroscopy (ISIS) [77] is a technique that depends on adding and subtracting signals. In the simplest case of one dimensional ISIS, a frequency selective inversion pulse with a simultaneous gradient inverts the magnetisation prior non-selective excitation. In a second experiment the inversion pulse is not present. If the scans are subtracted, only signal from within the inverted area are added.

ISIS is not susceptible to T_2 relaxation times. Also, the transformation involves only $\boldsymbol{z} \rightarrow -\boldsymbol{z}$, which is efficiently realised with adiabatic full passage pulses.

4.4.3. CSI

Last but not least there are spectroscopic imaging techniques. The most commonly used is **C**hemical **S**hift **I**maging (CSI) [78]. CSI uses phase encoding gradients in on two

Table 4.2.: ISIS addition and subtraction scheme for one, tow and three dimensional localisation. The + or - sign indicates whether a slice selecting 180° pulse is played out or not. The receiver phase determines whether two scans are added or subtracted. The pulse sequence can be seen in 8.7.

	Receiver	x	y	z
1-D	+	-		
	-	+		
required scans	2			
2-D	+	-	-	
	+	+	+	
	-	-	+	
	-	+	-	
required scans	4			
3-D	+	-	-	-
	-	+	+	+
	-	-	-	+
	+	+	+	-
	-	-	+	-
	+	+	-	+
	-	+	-	-
	+	-	+	+
required scans	8			

three dimensions to define the VOI. Spatial Fourier transformation in the phase encoded directions yields a spatial-spectral matrix.

This allows for simultaneous acquisition of many voxels in one process. However, acquisition of many phase encoding steps is time consuming. This makes it susceptible to motion and inhibits its use in dynamic studies of reasonable temporal resolution.

There are improvements to speed up the acquisition by combining echo planar imaging and spectroscopy [79]. A further discussion of the matter is, however, beyond the scope of this work.

Part II.

^{13}C Spectroscopy and Coupled Spins

5. ^{13}C Spectroscopy

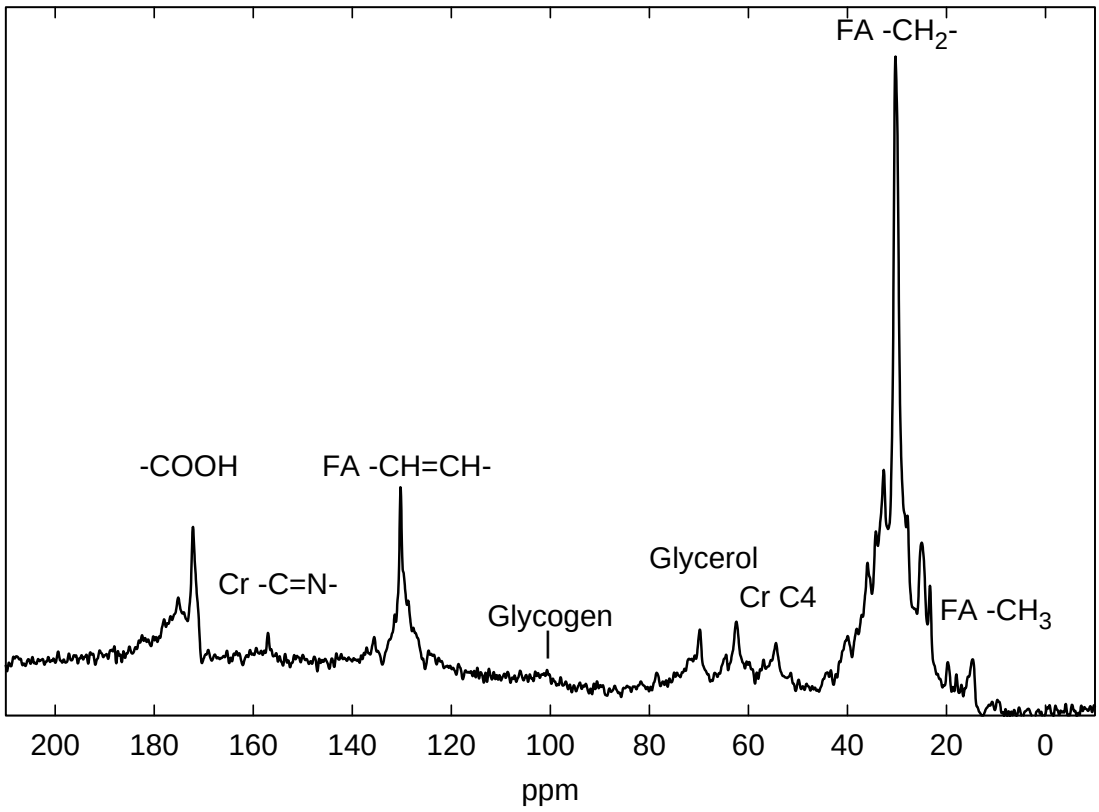

Figure 5.1.: Natural abundance, proton decoupled, ^{13}C spectrum from human calf muscle acquired at 3 T. Besides the predominant peaks of fatty acids (FA) and glycerol, resonances arising from creatine (Cr) and glycogen are visible.

The resonance lines of ^{13}C metabolites are distributed over a spectral range of ≈200 ppm, generally a big advantage, because many metabolite signals also present in the much more sensitive proton spectrum are strongly overlapping there, often to an extent where they are indistinguishable with typical line widths encountered in-vivo. The drawback of the wide spectral dispersion is that gradient-based localisation becomes very difficult and pulse design of sufficient bandwidths is at least demanding.

The signal intensity is low, the ^{13}C nucleus has a gyromagnetic ratio approximately fourfold smaller than protons. Further, the natural abundance of the ^{13}C isotope is only around 1%.

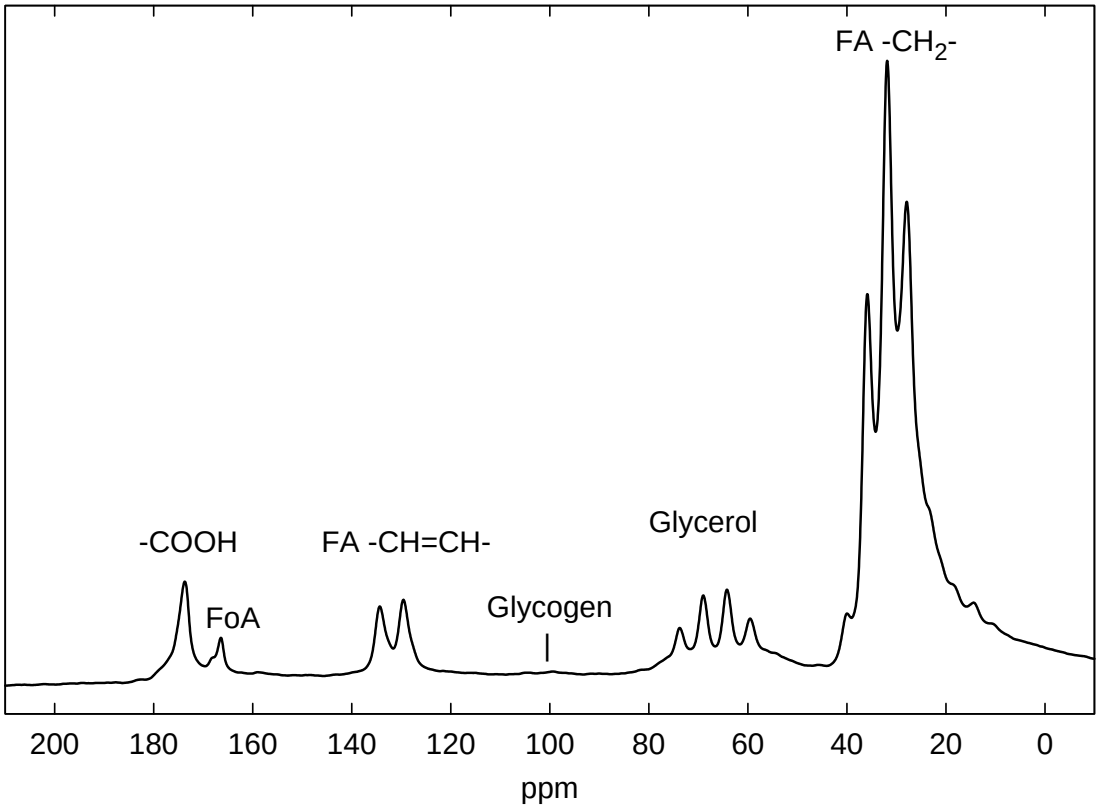

Figure 5.2.: Natural abundance ^{13}C spectrum of the human liver. The most prominent signals arise from fatty acids (FA) and glycerol. There is visible also a doublet resonance of a reference solution containing ^{13}C-enriched formic acid (FoA). One of the signals overlaps with the carboxyl peak of fatty acids at about 172 ppm and the other is visible at about 165 ppm.

As all organic substances contain carbon atoms, there is a wealth of information stored in ^{13}C spectra. In-vivo, for other tissue than brain, the spectrum is dominated by signals from fatty acids and glycerol. Spectra from human muscle and liver are shown in Figures 5.1 and 5.2.

In the liver and in skeletal muscle, glycogen C-1 is detectable. ^{13}C NMR spectroscopy is a valuable tool for in-vivo assessment of human glucose and fat metabolism. Fat and glycogen are virtually the only signals detectable at natural abundance.

The usage of isotope-enriched tracers, however, is an invaluable method for the study of metabolic pathways and determination of process dynamics. An example from [23] is shown in Figure 5.3. As the more and more ^{13}C-enriched tracer, typically glucose with ^{13}C enrichment at the C-1 position, is incorporated into muscle glycogen, the signal increases over time. The glycogen signal would have increased also if unlabelled glucose had been administered, but their is a significant gain in sensitivity with the isotope enrichment.

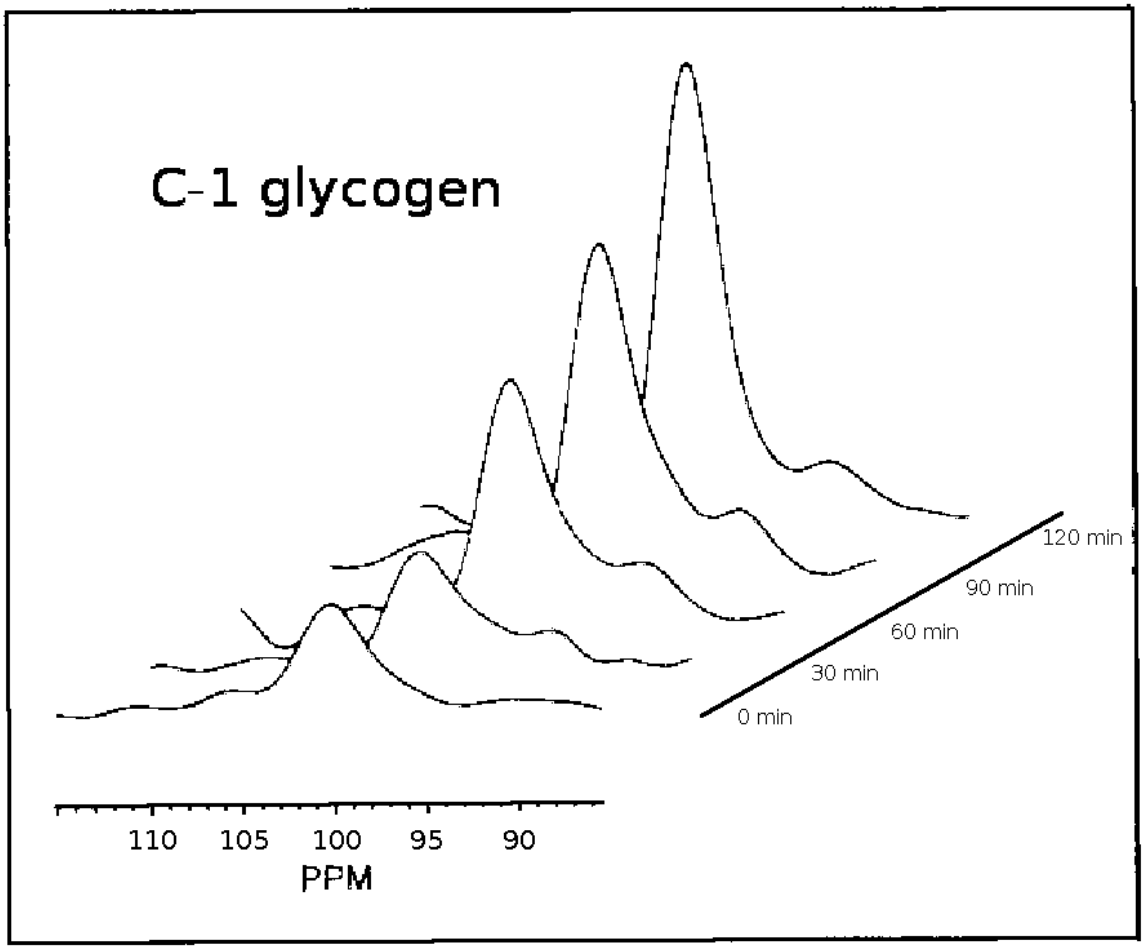

Figure 5.3.: Glycogen C-1 resonance at 100.5 ppm; the label appears with time when the tracer is incorporated into newly formed muscle glycogen. Reproduced from [23].

Heteronuclear coupling, which will be discussed in more detail in the following chapter, causes line splitting of many resonances. Line splitting divides the already low signal into several lines, thereby making the spectrum more complicated as well as reducing the SNR of metabolite signals.

The technique of proton decoupling, which breaks the coupling of the spins during acquisition, is very convenient for simplification and signal enhancement. Specific absorption rates (SAR) limitations of deposited heat are to be considered and become a limiting factor easily.

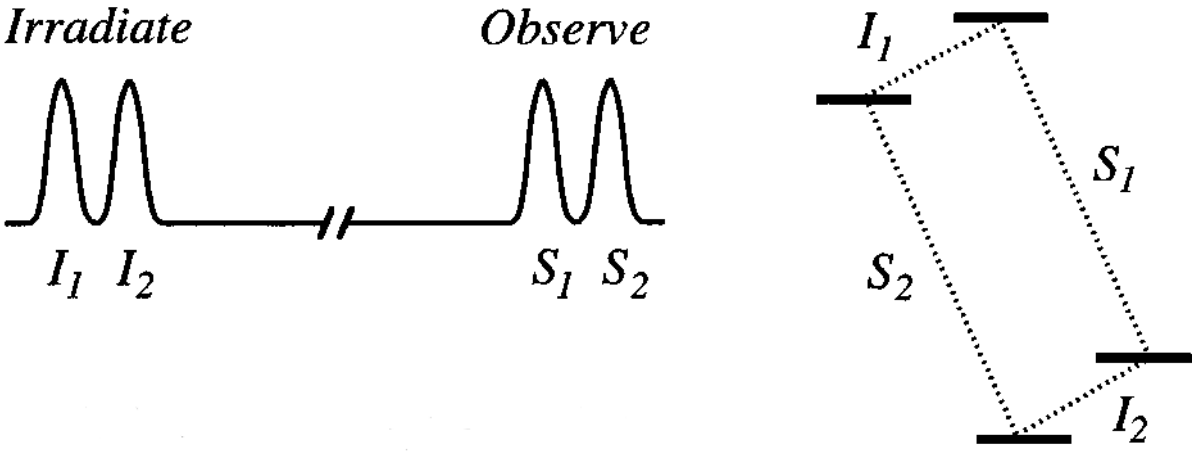

Figure 5.4.: Weakly coupled spins; left: the resonance frequency of both nuclei I and S are splitted symmetrically with a distance J. Right: corresponding energy levels. Reproduced from [80].

5.1. Coupled Spins

Nuclear spins are often magnetically coupled to other spins, forming a complex spin system. This leads to additional pathways for relaxations, line splitting and thus to a general complication of the experiment.

In the context of this chapter let us concentrate on the so called *scalar coupling* or J *coupling* only, that is described in the Hamiltonian by terms of the form

$$J\Phi_A\Phi_B, \tag{5.1}$$

a scalar product of the spin states. It is mediated through electrons of the involved nuclei.

The coupling does not depend on the external magnetic field. J is expressed in Hz. It can vary from a few Hz to up to 200 Hz for in-vivo detectable metabolites.

In general one distinguishes between homo-nuclear and hetero-nuclear coupling.

Depending on the strength of the coupling constant the distinction between strongly and weakly coupled spins is made. A weakly coupled spin system has a J significantly lower than the chemical shift difference. Since J does not depend on the static magnetic field, moving to higher field strengths, a strongly coupled system can become a weakly coupled one. Hetero-nuclear coupling is always a weak coupling since the different resonance frequencies of two nuclei are always much stronger than the coupling constant or the chemical shift.

The sensitivity of the signal detection is reduced because the coupling leads to a distribution of the magnetisation on more than one resonance, $\omega - J$ and $\omega + J$ in a two spin system. In the more general case of a IS_n system, the relative sensitivity of the n+1 lines is given by Pascal's triangle (1-1, 1-2-1, 1-3-3-1, 1-4-6-4-1, ...). Even at the

highest field strengths (>20 T) the deviation from the thermal equilibrium is only of the order of 10^{-5}.

Besides the loss in sensitivity, spectra are much more complicated and overlap of resonances more likely, giving rise to problems in quantification.

Another important issue is the evolution of the coupling after the excitation, leading to a complicated modulation function of the signal amplitude. For two weakly coupled spins the detectable magnetisation is, neglecting T_2 relaxation,

$$M(t) = M(0)\cos(2\pi Jt), \tag{5.2}$$

which is a relatively simple modulation. Setting the echo time of a STEAM or PRESS experiment to the wrong value will have fatal consequences on the detected signal intensity [81]. For slightly more complicated spin systems, however, the J modulation gets very complicated easily. Therefore, exact knowledge of the nature and strengths of the couplings is required [82, 83].

Yet, the coupling also holds additional information or can be used for advanced manipulations of the spin system. One useful application is the transfer of magnetisation from sensitive protons to insensitive ^{31}P or ^{13}C nuclei. The so-called polarisation transfer sequences will be discussed in more detail in Chapter 7.

5.2. Nuclear Overhauser Effect

The nuclear Overhauser effect (nOe) [65] is a dipole-dipole interaction through space between spatially adjacent nuclei. It is often observed in but not limited to coupled nuclei since it does not depend on a through-bond scalar interaction.

Quantitatively it can be described using dipolar relaxation theory. In a two spin system there are four energy levels, as indicated in Figure 5.4. Let us introduce the transition probabilities W_I, W_S, which describe transitions like from I_+ to I_- or S_+ to S_- and W_0 and W_2 which describe transitions like $I_+S_- \rightarrow I_-S_+$. If spin I is irradiated so that its magnetisation is zero, a new equilibrium state is formed:

$$0 = -(W_0 + W_S + W_2)(S_z - S_0) + (W_2 - W_0)I_0. \tag{5.3}$$

This can be rewritten in a more practical form:

$$nOe = 1 + \frac{\gamma_I}{\gamma_S}\left(\frac{W_2 - W_0}{W_0 + 2W_S + W_2}\right). \tag{5.4}$$

The maximum theoretical maximum nOe is given by:

$$nOe = 1 + \frac{\gamma_I}{\gamma_S}. \tag{5.5}$$

For equal spins (homonuclear case) the nOe is 1.5. For ^{1}H-^{31}P it is 2.235, for ^{1}H-^{13}C it is 2.968. In practise, the maximum value is not achievable, especially in the presence of other relaxation pathways than dipole-dipole interaction.

Although nOe generation can improve the signal intensities significantly, the quantification of metabolites is more difficult since the experimental nOe enhancement factors are often unknown.

6. Heteronuclear Decoupling

Consider a spin S of a nucleus that couples to the spin of another nucleus I, both nuclei have spin 1/2. Depending on whether the I is in state I_+, parallel, or I_-, antiparallel to the static magnetic field, the effective resonance frequencies of both spins S, ω_S and I, ω_I is shifted by $\pm J/2$. This is the well known line splitting of scalarly coupled spins.

6.1. Continuous Wave Decoupling

The "simplest" way of proton decoupling is continuous wave decoupling [84], i.e., irradiating the I spin at an amplitude strong enough to satisfy

$$\gamma B_2/2\pi \gg |J/2|. \tag{6.1}$$

In a rotating frame of reference with rotation equal to $\gamma B_2/2\pi$ the decoupling field B_2 becomes a static field. The resonance offsets become

$$\omega(I_+) = \sqrt{(\gamma B_2/2\pi)^2 + (\Delta\omega + J/2)^2} \tag{6.2}$$

$$\omega(I_-) = \sqrt{(\gamma B_2/2\pi)^2 + (\Delta\omega - J/2)^2} \tag{6.3}$$

If $\gamma B_2/2\pi$ coincides with the resonance frequency ω_I, $\Delta\omega = 0$ and complete decoupling is achieved. If more metabolites are of interest, however,

$\Delta\omega$ cannot be eliminated for all metabolites with different chemical shifts. The residual coupling J_{res} increases rapidly with $\Delta\omega$.

$$J_res = \omega(I_+) - \omega(I_-) = 2\pi J\Delta\omega/\gamma B_2. \tag{6.4}$$

For $\gamma B_2/2\pi = 3\,\mathrm{kHz}$, a chemical shift range of 200 ppm and a residual coupling of J_res <1 Hz the effective decoupling bandwidth, $2\Delta\omega$, is only 30 Hz. That renders it completely useless for in-vivo applications.

There were attempts to improve the performance with sine [85], square-wave [86] or sawtooth [87] modulations, but the results were disappointing. A significant progress could be achieved with *noise decoupling* [88]; in principle the continuous wave irradiation is replaced by white noise. In practise this was achieved by (pseudo-) random phase inversions of the decoupling B_2 field. The aperiodic phase shifts mix the spin states. The decoupling bandwidth is $1/\tau$ where τ is the mean time between two inversions. Over a long period of time this was the method of choice for high resolution ^{13}C MRS. Only with the advance to ever higher B_0 magnetic fields excessive sample heating prohibited its application.

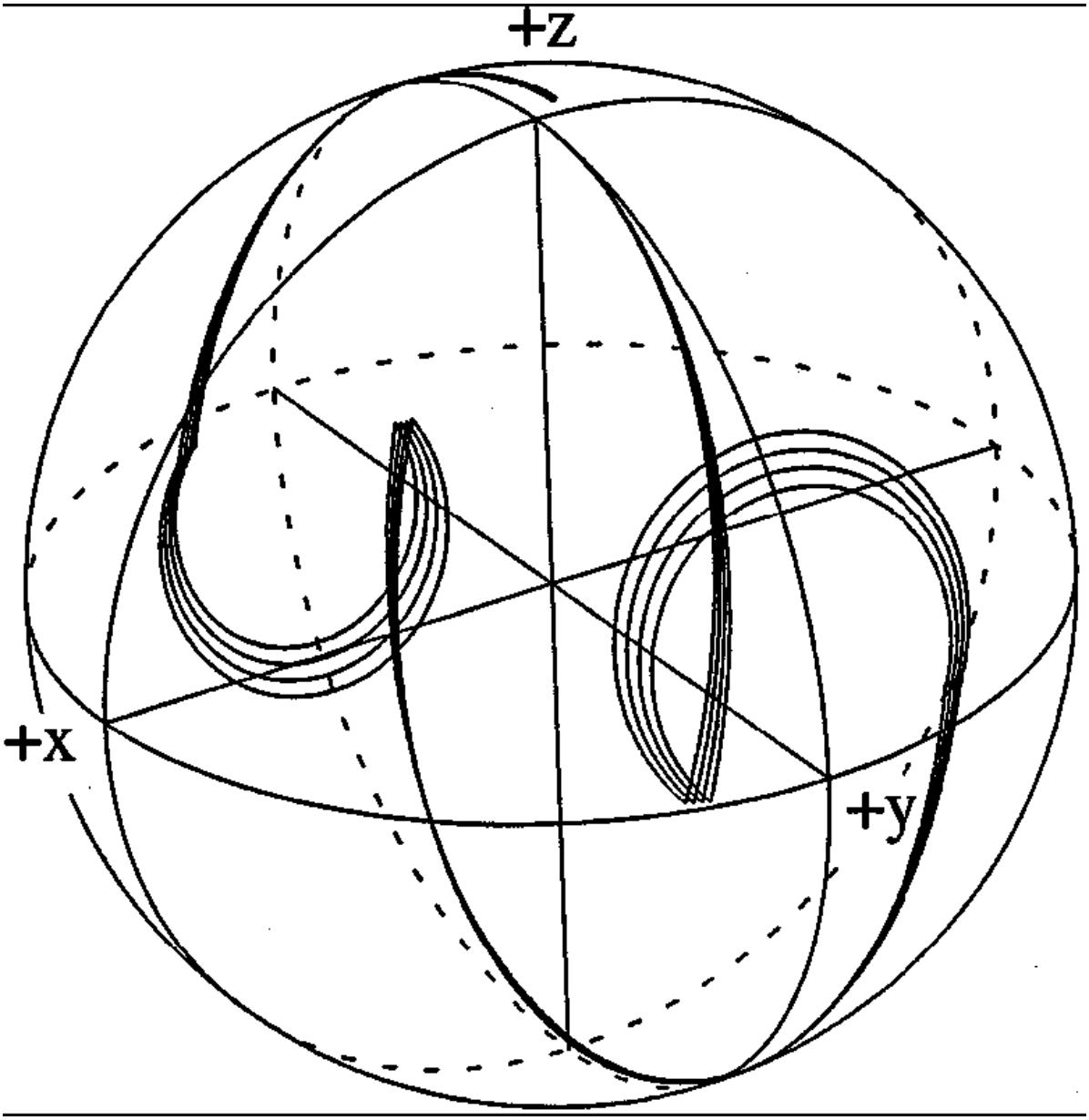

Figure 6.1.: Magnetisation trajectories of the I spins calculated for two consecutive composite pulses R_2R_2, where $R_2 = 90\,^\circ_{\boldsymbol{x}}270\,^\circ_{\boldsymbol{y}}90\,^\circ_{\boldsymbol{x}}$. The family of four trajectories represents resonance offsets near $\Delta B/B_2 = 0.3$, where $\Delta\omega = \gamma\Delta B/2\pi$. Note that all trajectories terminate very close to the $+\boldsymbol{z}$ axis in spite of the appreciable tilt of the effective fields ($\sim 17\,^\circ$). If this sequence is followed by the phase-inverted pair of pulses $\bar{R}_2\bar{R}_2$, the vectors are carried to a point much closer to the $+\boldsymbol{z}$ axis, and the overall effect is almost a perfect cycle. Reproduced from [80]

6.2. Composite Pulse Decoupling

The FID is sampled at a rate equal to the receiver bandwidth. The time between to ADC events, often referred to as the dwell time, is t_s. If between every consecutive ADC readouts the magnetisation of spin I is inverted, and the readout appears instantaneously at the centre between two inversions, it appears as if spin S is not coupled to spin I. This method is called *inversion decoupling* [89].

In practise this is not implementable since the readout never is instantaneous and the extremely short 180 ° pulses would require an extremely high amplitude.

There is, however, a practical solutions if the hard 180 ° pulses are replaced by composite pulses [90–93]

$$R_1 = 90^\circ(+x)180^\circ(+y)90^\circ(+x) \tag{6.5}$$

$$R_2 = 90^\circ(+x)270^\circ(+y)90^\circ(+x) \tag{6.6}$$

$$R_3 = 90^\circ(+x)180^\circ(2x)270^\circ(+x) \tag{6.7}$$

which are less sensitive to off-resonance effects and achieve inversion at lower power [89]. This is an advantage for in-vivo applications where power deposition is limited by SAR guidelines.

6.3. Magic Cycles and Supercycles

When RF pulses are repeated very often, errors from small imperfections accumulate; therefore they need to be combined into a self-compensating *magic cycle*. The first[1] such cycle suggested for proton decoupling was MLEV-4 [96]

$$MLEV-4 = RR\bar{R}\bar{R}. \tag{6.8}$$

R is one composite pulse and $\bar{R}$ is its phase inverted counterpart. Off resonance magnetisation trajectories of the I spin during the sequence R_2R_2 (Figure 6.1) return almost exactly to their starting point. The four vectors correspond to trajectories of spins with frequency offset $\Delta\omega \approx 0.3\gamma B_2/2\pi$. The tilt of the effective RF field is 167 °. If the elements $\bar{R}_2\bar{R}_2$ are added the magnetisation returns even closer to its origin.

The effective motion of spin I, which can be seen as a rotation about some axis, is very small during a complete cycle. Since the same cycle is repeated a lot of times, this motion of spin I can be seen as a low frequency rotation. With other words $\omega(I_+)$ and $\omega(I_-)$ are very similar and the resulting line splitting reduced significantly, below the resolvable linewidth of many experiments.

Even more effective is the incorporation of the MLEV-4 scheme into a *super cycle* [97–99], where sequences of modifications of the basic scheme are applied as a whole. An example is the following:

$$RR\bar{R}\bar{R} \rightarrow R\bar{R}\bar{R}R \tag{6.9}$$

[1] Actually the CPMG experiment was the first to use self-compensating cycles in NMR [94, 95].

or

$$RR\bar{R}\bar{R} \rightarrow \bar{R}\bar{R}RR. \tag{6.10}$$

Even more, completely unrelated cycles can be nested one into the other. For example the MLEV-4 cycle placed into the five-step phase cycle [100]

$$0^\circ - 150^\circ - 60^\circ - 150^\circ - 0^\circ \tag{6.11}$$

has proved especially effective.

6.4. WALTZ

In the theoretical work by Waugh [99] some shortcomings of the MLEV-16 decoupling sequence are explained which led to the development of WALTZ-16 decoupling [92,93]. It uses a composite inversion pulse (R_3) that is less sensitive to imperfections. If represented in multiples of a 90° flip angle, it is $1\bar{2}3$. The simplest magic cycle WALTZ-4 looks like

$$1\bar{2}3 \quad 1\bar{2}3 \quad \bar{1}2\bar{3} \quad \bar{1}2\bar{3}^2. \tag{6.12}$$

An expansion of the permutation scheme leads to the WALTZ-16 decoupling scheme

$$34\bar{2}3\bar{1}2\bar{4}2\bar{3} \quad 3\bar{4}2\bar{3}1\bar{2}4\bar{2}3 \quad 3\bar{4}2\bar{3}1\bar{2}4\bar{2}3 \quad \bar{3}4\bar{2}3\bar{1}2\bar{4}2\bar{3}. \tag{6.13}$$

Adjacent pulses with the same phase have been combined, for example $1 + 3 = 4$. The residual splitting of the WALTZ-16 (J_{res} is below 0.02 Hz [101], making ultra-high resolution ^{13}C MRS possible. Since WALTZ-16 is less sensitive to instrumental imperfections than is MLEV-16, it has superseded the latter, and is still in widespread use. The effective bandwidth of the pulse is about twice the pulse amplitude $\gamma B_2/2\pi$.

There are other cycles and supercycles and the basic element R can be composed of pulses with different flip angles. These additional degrees of freedom can be exploited by computer algorithms, which produced several extensions to the decoupling schemes [102–105], of which GARP [105] appears to be the most popular. For $\gamma B_2/2\pi = 3$ kHz, the GARP scheme achieves decoupling over an effective frequency bandwidth of 15 kHz, which is a significant improvement over WALTZ-16.

6.5. Adiabatic Decoupling

A revolutionary improvement in high resolution NMR was the introduction of adiabatic inversion into decoupling. The principles of adiabatic pulses are described in Chapter 2. Hyperbolic secant pulses have been used for decoupling by Starčuk et al. [106] or by Bendall [107].

To achieve higher bandwidths a flatter envelope for the amplitude modulation is preferable. The introduction of a class of functions for the amplitude modulation

$$A(t) = 1 - |\sin[\pi(2t - T)/2T]|^n, \tag{6.14}$$

[2]This formulation accounts the name WALTZ.

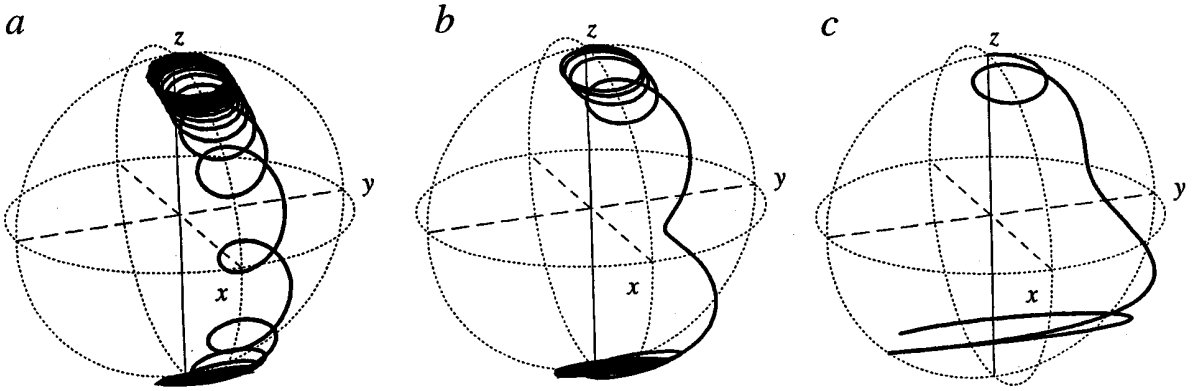

Figure 6.2.: Magnetisation trajectories for adiabatic rapid passage when the effective radiofrequency field $\boldsymbol{B}_{eff}$ starts at an inclination with respect to the $+\boldsymbol{z}$ axis (exaggerated for the purpose of illustration). (a) For good adiabaticity ($\eta = 10$) the path is a cycloid. (b) When the adiabatic condition begins to be violated ($\eta = 3$), the effective field moves too fast to allow a complete revolution of the magnetisation vector about $\boldsymbol{B}_{eff}$ when $\boldsymbol{B}_{eff}$ has its minimum value B_2 at resonance. (c) For a gross violation of the adiabatic condition ($\eta = 1$) the trajectory makes wild excursions and never reaches the $-z$ axis. Reproduced from [80]

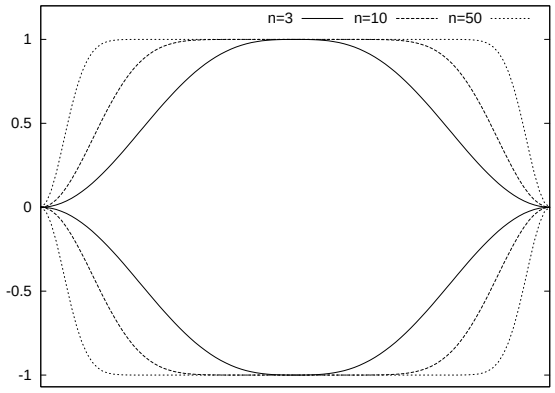

Figure 6.3.: The shape of the WURST pulse. Three different amplitude modulations for different values of the parameter n=3, 10, 20 are plotted. With increasing n, the plateau extends over a greater part of the pulse.

where n is an integer and T is the pulse length. If n is large, the amplitude is constant over most of the sweep range, favouring very wideband decoupling; if n is small certain imperfections are reduced but at the expense of a narrower effective bandwidth. This sausage shaped profile has given rise to the name WURST decoupling (Figure 6.3) [108–111]. The frequency is swept linearly across its band, which is equivalent to a parabolic phase modulation.

The big advantage of adiabatic decoupling is that the effective bandwidth increases quadratically with the B_2 field, whereas the decoupling bandwidth of other schemes increases only linearly with B_2. The evaluation of decoupling schemes is best performed by comparing the heat deposition generated. Therefore the introduction of the root-mean-squared amplitude of the pulse, $B_2(\mathrm{rms})$ makes sense which gives the effective power of a modulated pulse as it was an equally long square pulse.

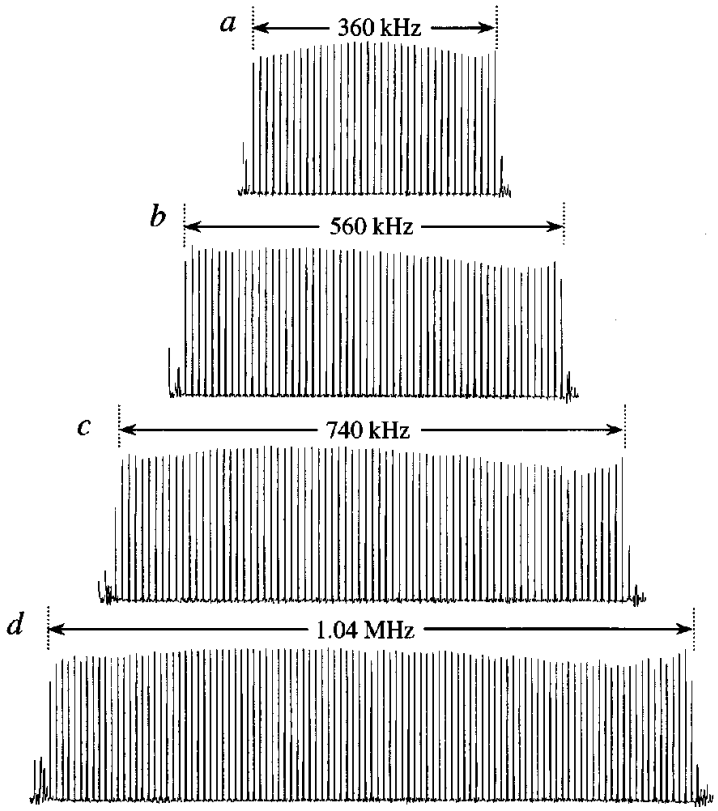

Figure 6.4.: Experimental offset dependence of WURST decoupling of ^{13}C while observing the protons in ^{13}C enriched sodium formate ($J = 200\,\mathrm{Hz}$). (a) $\gamma B_2(rms)/2\pi = 8.5\,\mathrm{kHz}$. (b) $\gamma B_2(rms)/2\pi = 10.5\,\mathrm{kHz}$. (c) $\gamma B_2(rms)/2\pi = 12.2\,\mathrm{kHz}$. (d) $\gamma B_2(rms)/2\pi = 14.3\,\mathrm{kHz}$. The variations in the intensity of the decoupled line are attributed mainly to limitations of the radiofrequency circuitry over these very wide frequency bands. Reproduced from [80].

7. Spectral Editing

7.1. Principles of Spectral Editing

While heteronuclear coupling appears as a disadvantage at first glance, it offers the possibility of spectral editing. Especially useful would be to prepare and use the proton magnetisation, with its higher gyromagnetic ratio and smaller spectral dispersion for localisation and transfer it onto the coupled carbon nucleus where the bigger spectral dispersion is useful in signal detection, besides the advantage of isotope tracing.

In general, spectral editing includes anything that manipulate an NMR spectrum in order to limit the detection to specific metabolites. Techniques like water suppression, spatial localisation and others would fall into this very general definition. In the context of this work, however, spectral editing is defined as manipulation and discrimination of spins with scalar coupling.

As mentioned in the previous chapter (Figure 5.4), the weakly coupled spins IS have four possible states I_+S_+, I_+S_-, I_-S_+ and I_-S_-. Since we concentrate ourselves on heteronuclear coupling, the restriction to weakly coupled spins is well justified.

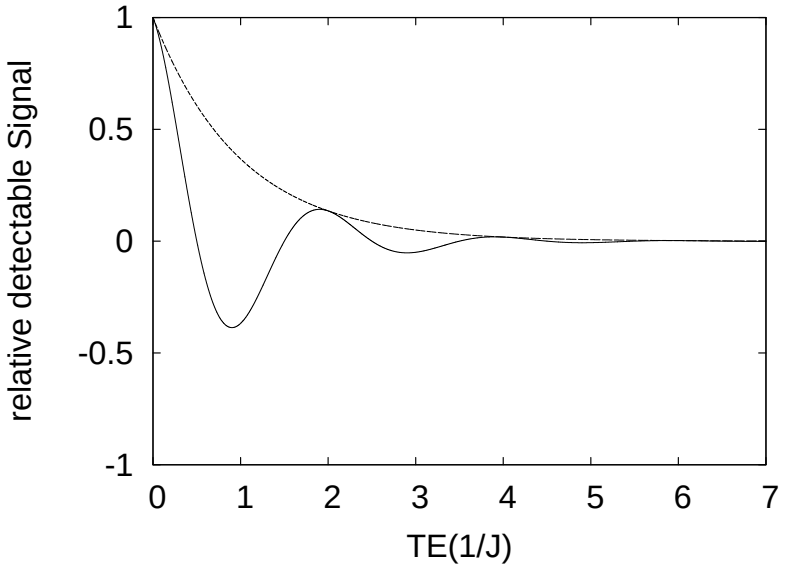

Figure 7.1.: Spin-echo of coupled and uncoupled spins

During a spin echo the coupled spins evolve as follows (TE is the echo time):

$$I(TE) = \qquad (I_x \cos(\pi JTE) + 2I_yS_z \sin(\pi JTE)) \exp(-TE/T_2) \qquad (7.1)$$

This assumes equal T_2 times of both in-phase (I_x) and anti-phase I_yS_z coherences, which is, in general, not the case. Anti-phase coherences have a net-integral of zero and may not be resolvable with in-vivo linewidths.

The relaxation of an uncoupled spin is, on the other hand, only dependent on the T_2 relaxation time.

$$S_x \exp(-t/T_2) \tag{7.2}$$

Both behaviours are shown in Figure 7.1. At $TE = n/2j$ the spins appear in

$n = 1, 2, 3$ ..... $-I_yS_z$ anti-phase coherences

$n = 2, 6, 10$ ..... $-I_x$ coherence inverted relative to uncoupled spins

$n = 4, 8, 12$ ..... I_x coherence equal to uncoupled spins.

The behaviour – and their differences – of coupled and uncoupled spins in spin echo is the basis of almost all spectral editing techniques.

Another important manipulation tool is a frequency selective pulse acting on only one of the coupled spins, either I or S. Since we consider only heteronuclear coupled spins, the application of a pulse at the basic frequency of one nucleus is automatically frequency selective with respect to the other nucleus. Application of a selective 180° pulse refocuses the J evolution at a time symmetrical to the inversion pulse.

7.2. Spectral editing methods

7.2.1. POCE

A practical utilisation of equations (7.1) and (7.2), *J difference editing*, was first proposed by Campbell et al. [112] and applied in-vivo by Rothman et al. [113] as a method for homo-nuclear editing proton spectra and thereby detecting lactate, GABA and others in the rat brain which are otherwise hidden by other metabolites with similar chemical shift.

The heteronuclear J difference editing sequence, generally known as POCE, *Proton-Observed Carbon-Edited* [114], is shown in Figure 7.2. Every other acquisition the ^{13}C 180° pulse is absent.

POCE is a sensitive alternative to direct detection of the insensitive carbon nuclear magnetic resonance signal since proton magnetisation, with its γ about four times higher than that of the ^{13}C nucleus, coupled to the carbon spin is measured.

7.2.2. INEPT

An alternative to POCE is polarisation transfer. Here, the carbon signal is detected, however, it is originally a proton coherence that is transferred to the other nucleus. This has several advantages. First, the ^{13}C chemical shift range is much bigger than that of the ^{1}H. Therefore, the spectral resolution is much higher and the decoupling bandwidth much lower. Second, it is a proton coherence originally, that means the experiment

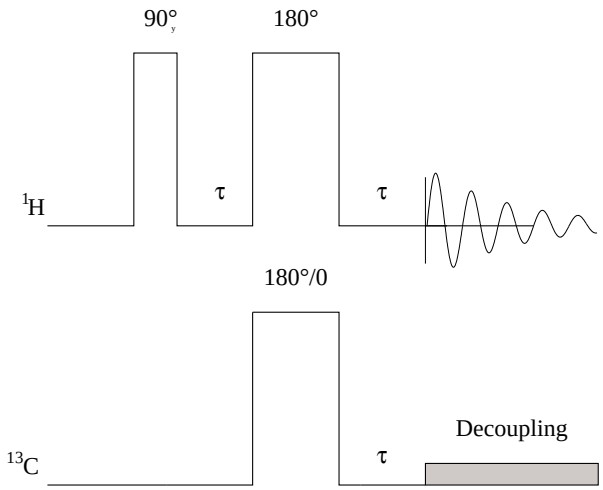

Figure 7.2.: POCE sequence. The ^{13}C pulse is turned on and off and the two experiments are subtracted. $\tau = 1/2J$. This leaves only signals from protons J-coupled to ^{13}C nuclei.

is governed by the – usually significantly shorter – T_1 times of the proton spins. The sensitivity enhancement of polarisation transfer is about four compared to almost three with full nOe generation. In practise, quantitative data on nOe enhancement factors are difficult to obtain. This introduces systematic errors in the quantification.

Insensitive Nuclei Enhanced by Polarisation Transfer (INEPT) [115] was the first sequence for heteronuclear polarisation transfer. The basic INEPT sequence is shown in Figure 7.3.

At the beginning the density operator is in the equilibrium state

$$\sigma(0) = I_z + \left(\frac{\gamma_S}{\gamma_I}\right) S_z. \tag{7.3}$$

After the first 90 ° pulse it becomes

$$\sigma(+) = -I_y + \left(\frac{\gamma_S}{\gamma_I}\right) S_z. \tag{7.4}$$

During the delay $\tau_1/2$ the spin system evolves under J and chemical shifts.

$$\sigma(\tau_1/2) = -I_y \cos(\pi J \tau_1/2) + 2I_x S_z \sin(\pi J \tau_1/2) + \left(\frac{\gamma_S}{\gamma_I}\right) S_z \tag{7.5}$$

The simultaneous 180 ° pulse on both spins I and S refocuses chemical shift but not J evolution:

$$\sigma(\tau_1/2+) = I_y \cos(\pi J \tau_1/2) - 2I_x S_z \sin(\pi J \tau_1/2) + \left(\frac{\gamma_S}{\gamma_I}\right) S_z. \tag{7.6}$$

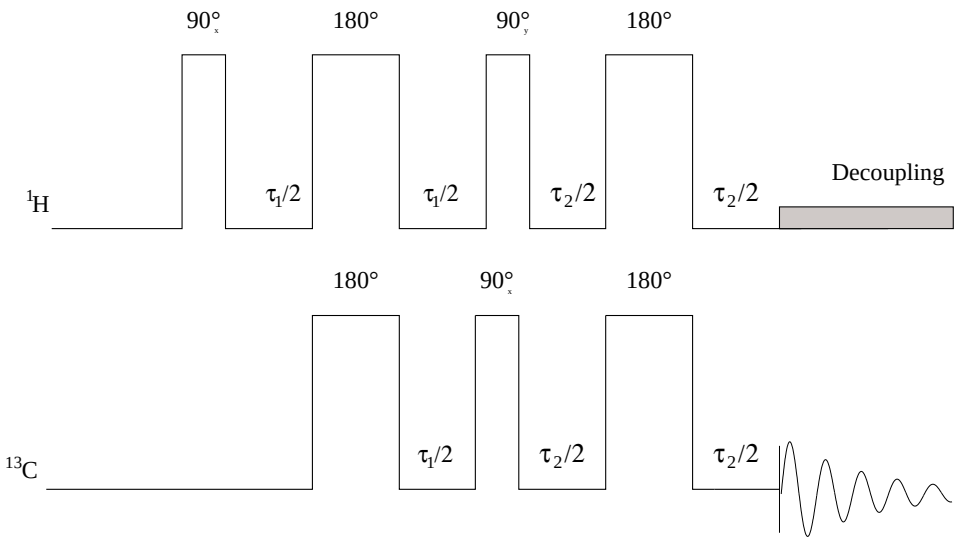

Figure 7.3.: Refocused INEPT sequence. $\tau_1 = 1/4J$. After the two simultaneous 90° pulses the basic INEPT sequence is completed. The magnetisation, however, is in an anti-phase state. Therefore, the acquisition is delayed to let the anti-phase coherences evolve into an in-phase state to permit proton decoupling. The two 90° pulses refocus $\boldsymbol{B}_0$ inhomogeneities and chemical shift. For CH, CH_2 and CH_3 spin systems the optimum values for the delay τ_2 are different. If a simultaneous detection of different spin systems is required, the timing is not optimal.

In the subsequent delay $\tau_1/2$ the spins evolve into

$$\sigma(\tau_1) = I_y \cos(\pi J \tau_1) - 2I_x S_z \sin(\pi J \tau_1) + \left(\frac{\gamma_S}{\gamma_I}\right) S_z. \tag{7.7}$$

The final 90° pulses generate

$$\sigma(\tau_1+) = I_y \cos(\pi J \tau_1) - 2I_z S_y \sin(\pi J \tau_1) - \left(\frac{\gamma_S}{\gamma_I}\right) S_y. \tag{7.8}$$

If the sign of the final ^{1}H pulse is flipped every other experiment and the two scans are subtracted, only the term

$$-2I_z S_y \sin(\pi J \tau_1) \tag{7.9}$$

remains. This reduces to $2I_z S_y$ when $\tau_1 = 1/2J$. As one can see from equations (7.3) to (7.8), the detected signal was originally a proton coherence. Unfortunately, this is a anti-phase coherence, which excludes the possibility to decouple.

There is an extension, commonly known as refocused INEPT. Here, the acquisition is

delayed to let it evolve into in-phase

$$\begin{aligned}\sigma(\tau_1+\tau_2/2) &= [I_y\cos(\pi J\tau_2/2) - 2I_xS_z\sin(\pi J\tau_2/2)]\cos(\pi J\tau_1)\\ &\quad -[2I_zS_y\cos(\pi J\tau_2/2) - S_x\sin(\pi J\tau_2/2)]\sin(\pi J\tau_1)\\ &\quad -\left(\frac{\gamma_S}{\gamma_I}\right)[S_y\cos(\pi J\tau_2/2) - 2I_zS_x\sin(\pi J\tau_2/2)].\end{aligned} \tag{7.10}$$

In the middle of the delay a 180 ° pulse refocuses chemical shift evolution.

$$\begin{aligned}\sigma(\tau_1+\tau_2/2) &= [I_y\cos(\pi J\tau_2/2) - 2I_xS_z\sin(\pi J\tau_2/2)]\cos(\pi J\tau_1)\\ &\quad -[2I_zS_y\cos(\pi J\tau_2/2) - S_x\sin(\pi J\tau_2/2)]\sin(\pi J\tau_1)\\ &\quad +\left(\frac{\gamma_S}{\gamma_I}\right)[S_y\cos(\pi J\tau_2/2) - 2I_zS_x\sin(\pi J\tau_2/2)].\end{aligned} \tag{7.11}$$

Finally,

$$\begin{aligned}\sigma(\tau_1+\tau_2/2) &= [I_y\cos(\pi J\tau_2) - 2I_xS_z\sin(\pi J\tau_2)]\cos(\pi J\tau_1)\\ &\quad -[2I_zS_y\cos(\pi J\tau_2) - S_x\sin(\pi J\tau_2)]\sin(\pi J\tau_1)\\ &\quad +\left(\frac{\gamma_S}{\gamma_I}\right)[S_y\cos(\pi J\tau_2) - 2I_zS_x\sin(\pi J\tau_2)].\end{aligned} \tag{7.12}$$

If $\tau_1 = 1/2J$ and $\tau_2 = 1/2J$ and the phase cycle of the second 90 ° pulse is applied, the remaining signal is

$$\sigma(\tau_1+\tau_2) = S_x + \left(\frac{\gamma_S}{\gamma_I}\right)2I_zS_x. \tag{7.13}$$

For I_nS systems, the situation gets more complicated in the refocusing part of the sequence. After the excitation of the ^{13}C nuclei, the coherences start to evolve under the influence of n coupling partners.

7.2.3. DEPT

An alternative to INEPT is *Distortionless Enhancement by Polarisation Transfer* (DEPT) [116]. The basic sequence is displayed in Figure 7.4. Although it looks similar to the INEPT sequence, the way the polarisation is transferred from protons to the ^{13}C channel is different.

The first 90 ° pulse produces

$$\sigma(+) = -I_y + \left(\frac{\gamma_S}{\gamma_I}\right)S_z. \tag{7.14}$$

During the time τ spins evolve into

$$\sigma(\tau) = -I_y\cos(\pi J\tau) + 2I_xS_z\sin(\pi J\tau) + \left(\frac{\gamma_S}{\gamma_I}\right)S_z. \tag{7.15}$$

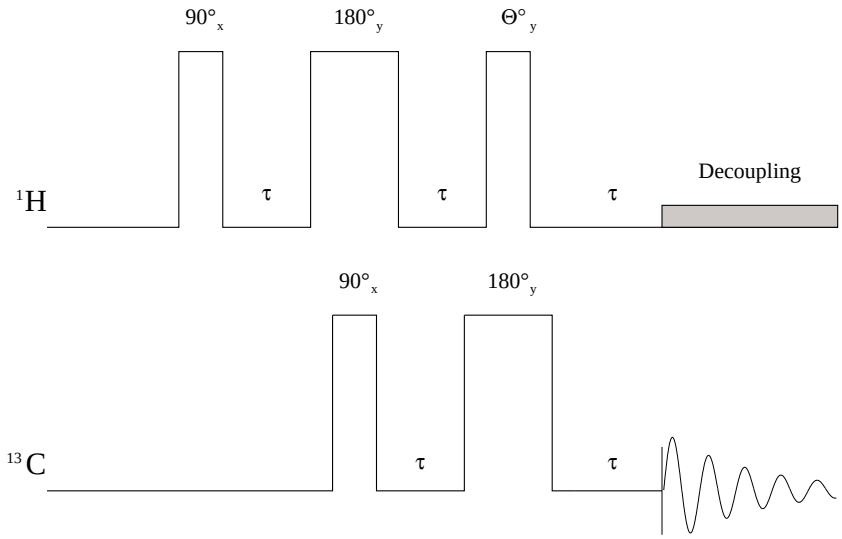

Figure 7.4.: The basic DEPT sequence. For a detailed description of the evolution of the magnetisation refer to the text or the legend Figure 7.5.

The simultaneous 90 ° and 180 ° leads to

$$\sigma(\tau+) = -I_y \cos(\pi J\tau) + 2I_x S_y \sin(\pi J\tau) - \left(\frac{\gamma_S}{\gamma_I}\right) S_y. \tag{7.16}$$

This contains a multi quantum state. During the next delay τ the system evolves into

$$\begin{aligned}\sigma(2\tau) &= \cos(\pi J\tau)[-I_y \cos(\pi J\tau) + 2I_x S_z \sin(\pi J\tau)] + 2I_x S_y \sin(\pi J\tau) \\ &\quad + \left(\frac{\gamma_S}{\gamma_I}\right)[-S_y \cos(\pi J\tau) + 2I_z S_x \sin(\pi J\tau)].\end{aligned} \tag{7.17}$$

The Θ pulse generates magnetisation from the double quantum states.

$$\begin{aligned}\sigma(2\tau+) =& I_y \cos(\pi J\tau)[-I_y \cos(\pi J\tau) - 2I_x S_z \sin(\pi J\tau)\cos(\Theta) + 2I_z S_z \sin(\pi J\tau)] \\ &+ 2I_x S_y \sin(\pi J\tau)\cos(\Theta) - 2I_z S_y \sin(\pi J\tau)\sin(\Theta) \\ &+ \left(\frac{\gamma_S}{\gamma_I}\right)[-S_y \cos(\pi J\tau) \\ &- 2I_z S_x \sin(\pi J\tau)\cos(\Theta) - 2I_x S_y \sin(\pi J\tau)\sin(\Theta)]\end{aligned} \tag{7.18}$$

During the final delay τ the anti-phase state evolves into in-phase magnetisation.

$$\begin{aligned}\sigma(3\tau) =& - I_y[\cos^3(\pi J\tau) + \cos(\pi J\tau)\sin(\pi J\tau)\cos(\Theta)] \\ &+ 2I_x S_z \cos^2(\pi J\tau)\sin(\pi J\tau)(1-\cos(\Theta)) + 2I_z S_z \cos(\pi J\tau)\sin(\pi J\tau)\sin\Theta \\ &+ 2I_x S_y \sin(\pi J\tau)\cos(\Theta) - 2I_z S_y \cos(\pi J\tau)\sin(\pi J\tau)\sin(\Theta) \\ &+ S_x \sin^2(\pi J\tau)\sin(\Theta) \\ &+ \left(\frac{\gamma_S}{\gamma_I}\right)[-S_y[\cos^2(\pi J\tau) + \sin^2(\pi J\tau)\cos(\Theta)] \\ &+ 2I_z S_x \cos(\pi J\tau)\sin(\pi J\tau)(1-\cos(\Theta)) - 2I_z S_z \sin(\pi J\tau)\sin(\Theta)]\end{aligned} \tag{7.19}$$

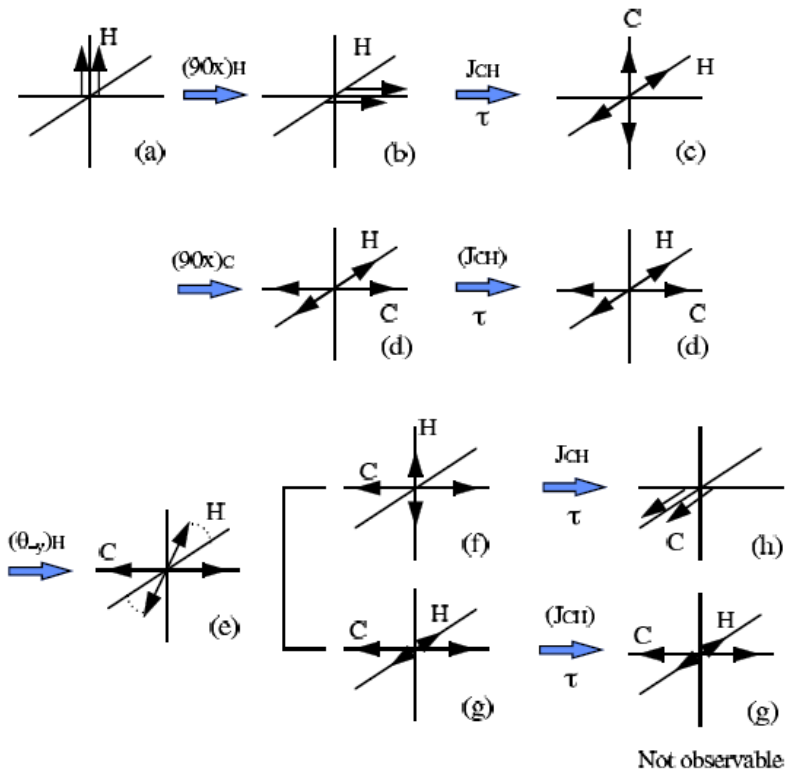

Figure 7.5.: Non-classical vector diagrams of the DEPT experiment for a two-spin system IS with one proton coupled to ^{13}C. After the first ^{1}H pulse the in-phase ^{1}H vector is converted to an anti-phase coherence due to scalar coupling between ^{13}C and ^{1}HÀ 90 ° pulse on ^{13}C on the $\boldsymbol{x}$ axis generates the desired multiple quantum state. This coherence is frozen until the last ^{1}H pulse with a flip angle Θ is applied. Then the multiple quantum coherence is partially converted into an anti-phase state, which finally evolves into the observable in-phase magnetisation. The delay τ is set to $1/2J$.to maximise the magnitude of the anti-phase and multiple quantum vectors. The two 180 ° pulses will refocus chemical shifts and are not included in the diagram. Reproduced from http://www.biophysics.org/education/

In the case of $\tau = 1/2J$ (7.19) reduces to

$$\sigma(3\tau) = S_x \sin(\Theta) + \left(\frac{\gamma_S}{\gamma_I}\right)[-S_y \cos(\Theta) - 2I_z S_z \sin(\Theta)]. \tag{7.20}$$

Phase cycling the Θ pulse eliminates the second term. The last one is an undetectable spin-order state. Figure 7.5 illustrates the spin evolution.

The signal intensity for DEPT for IS, I_2S and I_S spin systems depends on the flip angle Θ.

$$IS \ldots\ldots\ldots\

$$I_2S \ldots\ldots\ldots\ldots\ldots\ldots\ldots\ldots\ldots\ldots\ldots\ldots : \sin(\Theta)\cos(\Theta)$$

$$I_3S \ldots\ldots\ldots\ldots\ldots\ldots\ldots\ldots\ldots\ldots\ldots\ldots : \sin(\Theta)\cos^2(\Theta)$$

Unlike in basic INEPT, in DEPT the coherences are in-phase and decoupling is possible. In a matched DEPT experiment ($\tau = 1/2J$, spectra show no phase distortions. For mismatched DEPT, distortions arise from spurious anti-phase coherences.

7.3. Fully adiabatic INEPT

Nuclear spins are sensitive to the orientation of other nuclear spins in their vicinity, leading to the so-called scalar coupling. ^{13}C atoms in CH, CH_2, and CH_3 functional groups are coupled to protons. A typical value for the coupling constant J of metabolites encountered in in-vivo NMR spectra is $J \approx 140\,Hz$. The coherences which arise can be used for heteronuclear polarisation transfer.

Besides the magnetisations $\boldsymbol{M}_x$, $\boldsymbol{M}_y$, and $\boldsymbol{M}_z$, coupled spins can appear in more complex configurations. In heteronuclear polarisation transfer this is used to transfer magnetisation from the sensitive proton to the insensitive ^{13}C spin. In INEPT (Figure 7.3) the coherence evolution of CH is as follows: In this case I is the sensitive proton, S is the ^{13}C magnetisation.

$$90^\circ_x\ {}^1H : I_z \rightarrow I_y. \tag{7.21}$$

The simultaneous 180° pulses refocus B_0 inhomogeneities and chemical shifts but leave J evolution untouched.

$$\tau : I_y \rightarrow \qquad 2I_xS_z\sin(\pi J\tau) \tag{7.22}$$

$$90^\circ_y\ {}^1H, 90^\circ_x\ {}^{13}C : 2I_xS_z\sin(\pi J\tau) \rightarrow \qquad 2I_zS_y\sin(\pi J\tau). \tag{7.23}$$

The last two pulses transfer the transversal proton coherence to the carbon nucleus. For $\tau = 1/2J$ this reduces to $2I_zS_y$. This, however, is an anti-phase coherence that will cancel out under proton decoupling. Only those expressions contributing to the polarisation transfer signal were considered. Pure ^{13}C magnetisation is cancelled by a two-step phase cycling.

In refocused INEPT the acquisition is delayed until J evolution generates in-phase S_x magnetisation. For CH groups this delay is $1/2J$. For CH_2 and CH_3 spin systems the optimal evolution time is different. This makes the simultaneous optimal pulse sequence timing for different spin systems impossible.

Polarisation transfer was applied in-vivo by several groups with different methods and to different tissues [117–120].

7.4. The Pulse Sequence

In in-vivo studies surface coils are most commonly used for ^{13}C spectroscopy because they are widely available, offer a high signal to noise ratio and may be placed all over

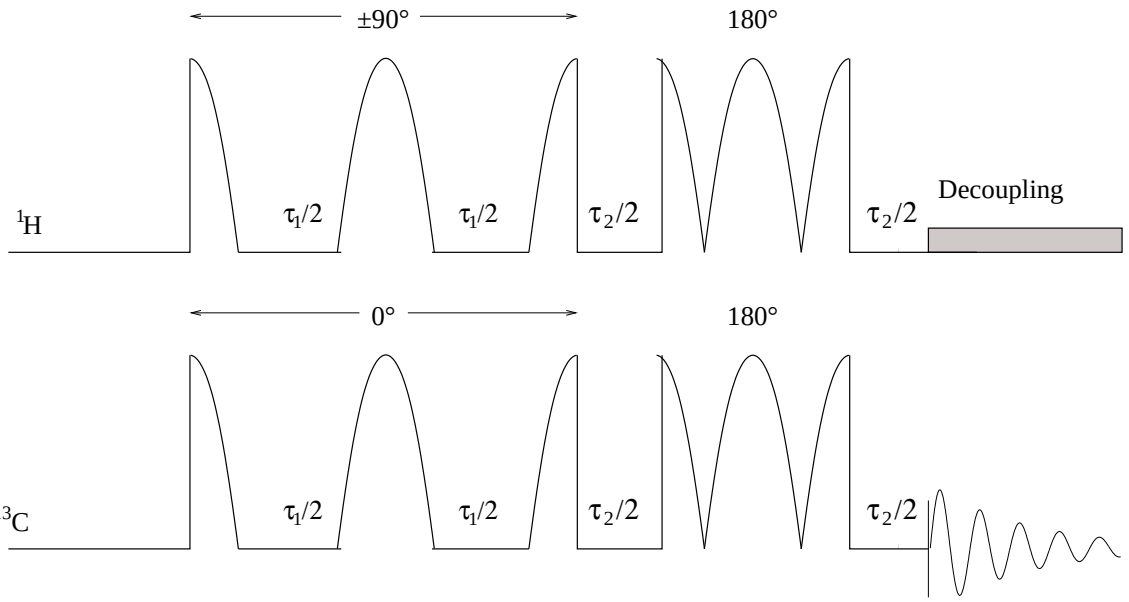

Figure 7.6.: Adiabatic refocused INEPT. The simultaneous applied segmented BIR-4 pulse produce the polarisation transfer in the time $\tau_1 = 1/2J$. After τ_1 they produce the same coherences as the pulses of the basic INEPT sequence. The 180 ° BIR-4 pulses refocus chemical shift evolution and B_0inhomogeneities while the anti-phase coherences evolve into magnetisation during τ_2.

the human body. Due to their inherent B_1 field inhomogeneity adiabatic plane rotation pulses (BIR-4) [9, 10] are used for this sequence. The challenges in this experiment are very restrictive timing and limits to peak and average RF-power.

The basic INEPT sequence is shown in Figure 7.3. The simultaneous application of ^{1}H and ^{13}C pulses transfers the magnetisation from the sensitive proton to the coupled ^{13}C spin which is then detected. The splitting pattern, however, is such that the coherences are 180 ° phase shifted. This makes decoupling impossible.

Therefore an extended version of INEPT, *refocused INEPT*, was introduced. During an additional delay of 1/2J – for an IS spin system – the coupling evolves to give parallel orientation at the end. Halfway through this delay, a 180 ° pulse is applied simultaneously on both channels.

The first difficulty is the timing. The typical value of J for most metabolites is 140Hz. Consequently, a complete BIR-4 pulse needs to fit in 3.57s. A careful choice of the modulation function is required.

The sequence consists of a total of 16 AHP and time-reversed AHP elements. Effectively, eight 180 ° pulses are played out in less then 10 ms. The rigorous requirements on sequence timing impose strict limits on the pulse shape to not violate peak power and SAR limits yet produce the desired flip angle.

Phantom experiments were performed on a solution of 200 mM glutamine, which is very similar to glutamate. A circular 10 cm linear polarised surface coil tuned to ^{1}H

and ^{13}C frequencies was used for transmission, signal detection and proton decoupling. Non-localised shimming was performed on the proton channel of the surface coil.

^{13}C spectra were acquired with 15 kHz bandwidth, 1024 complex data points resulting in 68 ms acquisition time while broadband ^{1}H decoupling was applied using a WALTZ-4 decoupling sequence (542 μs element) at $\approx$ 40 W. The same WALTZ-4 pulse with less power was used for nOe generation.

Figure 7.6 shows the pulse sequence as described in [121]. by Payne et al. used in their experiment ^{31}P spectroscopy where timing is less restrictive due to much smaller coupling constants. The restrictions on pulse shape and duration are much tighter in the ^{13}C experiment.

In the INEPT experiments the BIR-4 pulses were composed of adiabatic half passage (AHP) pulses (or their time reversal) with sine/cosine modulation functions. This AHP was also used for excitation in the nOe pulse acquire experiment. The repetition time was 2 s.

7.5. Results

A series of spectra with different echo-times $T_{E,2} = \tau_2$ (Figure 7.7) was acquired to simultaneously maximise C-2 (CH) and C-3, C-4 (CH_2) signals. It should be noted that these groups exhibit different J evolution, so, a compromise has to be made. A suitable value for $T_{E,2}$ was found to be 4.8 ms. The detection of both C-2 and C-4 is required for the quantification of TCA-cycle turnover.

An in-vivo experiment on the calf muscle of a healthy male volunteer was performed. The result can be seen in Figure 7.8. The INEPT spectrum is of comparable quality to the nOe-enhanced pulse acquire experiment.

So far no ^{13}C enrichment experiment were performed because there were clinical problems associated with the intended protocol. Therefore only phantom experiments on glutamine and no in-vivo data on glutamate can be shown.

7.6. Conclusions

In this part of the present work it was possible to demonstrate the efficacy of fully adiabatic refocused INEPT in human skeletal muscle. The sequence could be extended further by ISIS of the proton magnetisation if a better localisation was desirable.

This experiment involves a total of four 180 ° pulses on each channel within less than 10 ms. These place high efficiency demands on both the coil and the pulse itself, because the maximum available peak power was 1 kW and the total irradiation was limited by legal SAR guidelines. The sine/cosine modulated BIR-4 pulse had the necessary bandwidth and operated at the power levels available.

The most important source of signal loss in INEPT is the strong dependence of signal intensities on the sequence timing. Unfortunately, it is not possible to refocus CH, CH_2 and CH_3 groups at the same time. One has to either focus on one signal or chose a

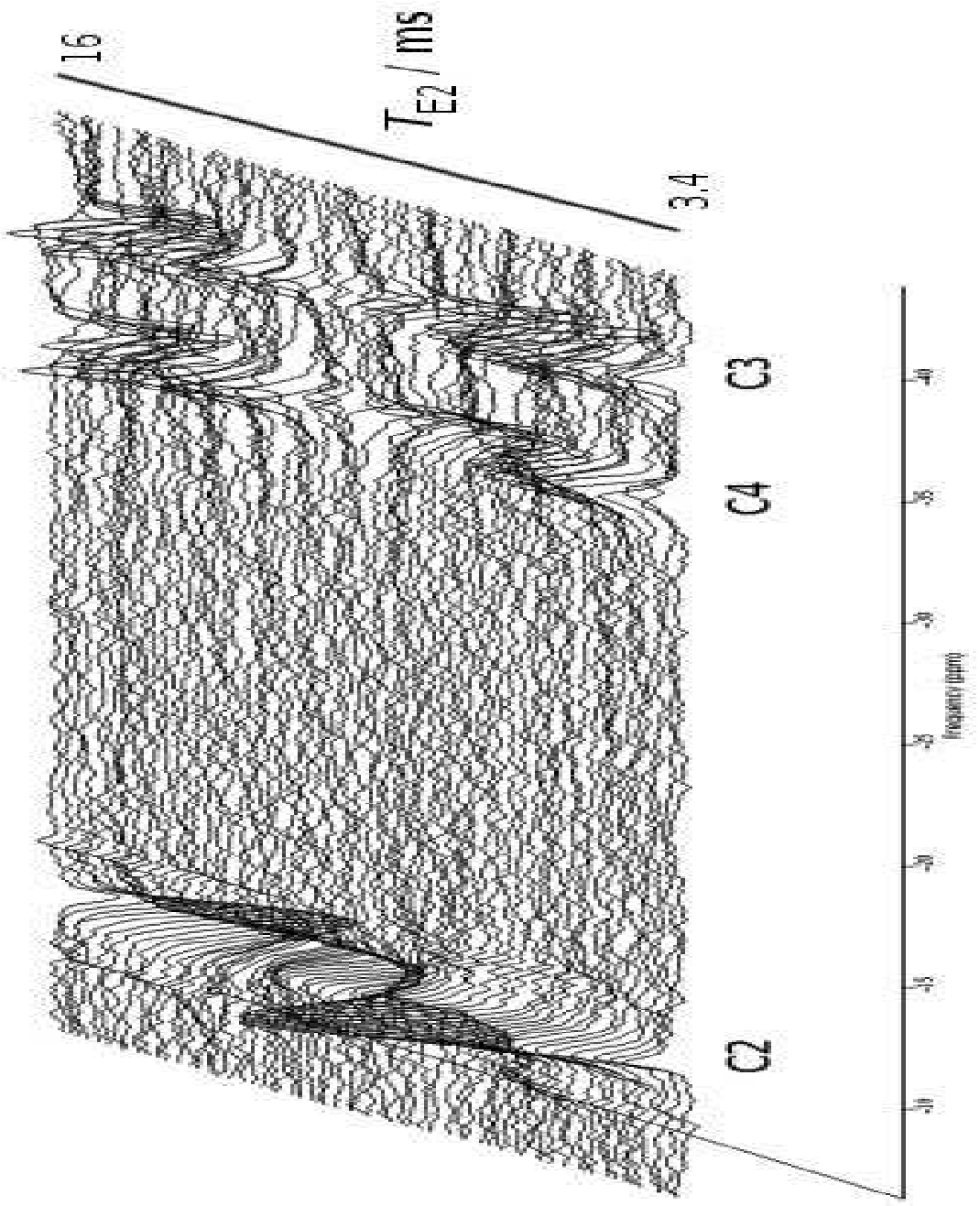

Figure 7.7.: Calibration experiment on a phantom of aqueous solution of glutamine. The echo time $T_{E,2}$ of the fully adiabatic refocused INEPT sequence is varied to experimentally optimise the sequence timing for both CH (C-2 position) and CH_2 (C-3 and C-4 positions) functional groups. The signal intensity is plotted as a function of $T_{E,2}$, 3.4 ms-16.2 ms, 0.2 ¿ms steps.

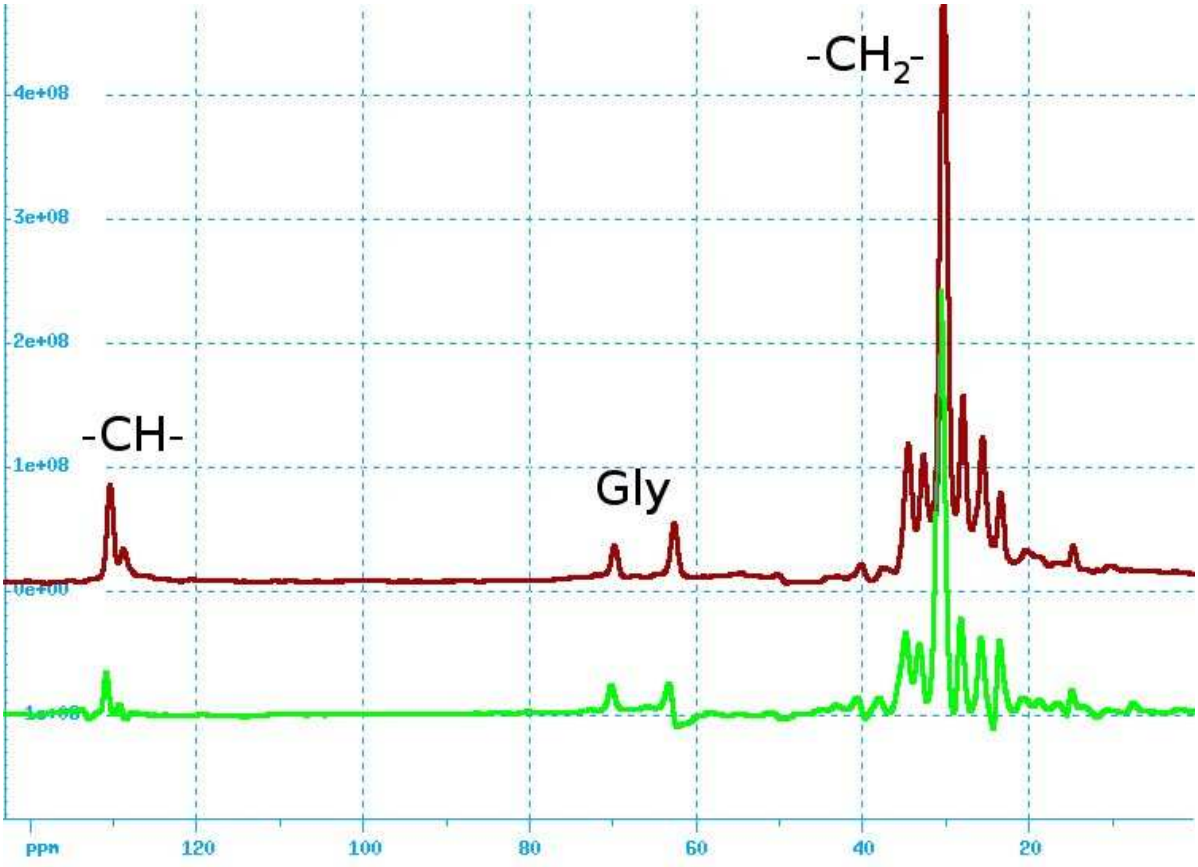

Figure 7.8.: Comparing ^{13}C spectra of human calf muscle. INEPT (bottom), nOe enhanced pulse-acquire (top), 256 accumulations in 8.5 min each. The timing was set to simultaneously detect CH and CH_2 groups.

suitable value where neither resonance shows maximal intensity. This can be seen from Figure 7.7. The signal modulation of the CH group is a single sinusoidal, whereas the CH_2 groups experience a more rapid and complicated modulation with $T_{E,2}$. Spurious anti-phase coherences lead to partial signal cancellation, giving rise to further signal loss. Anyways, compared to the nOe experiment, the signal intensities are similar.

In conclusion, fully adiabatic INEPT takes full advantage of the sensitivity of the surface coil and combines it with the potential of spectral editing.

Part III.

Chemical Exchange and Energy Metabolism

8. The in-vivo ^{31}P Saturation Transfer Experiment

8.1. Theory of Magnetisation Transfer

Consider two metabolites A and B that are in a steady state exchange

$$A \underset{k_{rev}}{\overset{k_{for}}{\leftrightarrows}} B. \tag{8.1}$$

The unidirectional rate constant k_{for} describes the reaction from A to B, the corresponding flux is $k_{for}[A]$. Similarly, the flux from B to A is described by $k_{rev}[B]$.

Modifying the Bloch equations to include chemical exchange gives

$$\frac{dM_{zA}(t)}{dt} = \frac{(M^0_{zA} - M_{zA}(t)}{T_{1A}} - k_{for}M_{zA}(t) + k_{rev}M_{zB}(t) \tag{8.2}$$

$$\frac{dM_{zB}(t)}{dt} = \frac{(M^0_{zB} - M_{zB}(t)}{T_{1B}} + k_{for}M_{zA}(t) - k_{rev}M_{zB}(t). \tag{8.3}$$

The analytical solution of these differential equations is

$$M_{zA}(t) = M^0_{zA} + c_1 e^{a_1 t} + c_2 e^{a_2 t} \tag{8.4}$$

$$M_{zB}(t) = M^0_{zB} + c_3 e^{a_1 t} + c_4 e^{a_2 t} \tag{8.5}$$

where

$$a_{1,2} = \frac{1}{2}\sqrt{-(R_A + R_B) \pm [(R_A + R_B)^2 + 4k_{for}k_{rev}]} \tag{8.6}$$

$$c_1 = M_{zA}(0) - M^0_A(t) - c_2 \tag{8.7}$$

$$c_2 = \frac{[(M_{zA}(0) - M^0_{zA})(a_1 + R_A) + k_{rev}(M^0_{zB} - M_{zB}(0)}{a_1 - a_2} \tag{8.8}$$

$$c_3 = c_1\frac{a_1 + R_A}{k_{rev}} \tag{8.9}$$

$$c_4 = c_2\frac{a_2 + R_A}{k_{rev}} \tag{8.10}$$

R_A and R_B are the longitudinal exchange rate constants. In the presence of chemical exchange they are given by

$$R_A = \frac{1}{T_{1A}} + k_{for} \tag{8.11}$$

$$R_B = \frac{1}{T_{1B}} + k_{for}. \tag{8.12}$$

It should be mentioned that T_{1A} and T_{1B} are the longitudinal relaxation times without chemical exchange.

8.2. General Remarks on the Experimental Implementation – ATP Synthesis

Several different experiments exist to acquire the necessary parameters. In this work the saturation transfer experiment [122], [123] was used.

Saturation of γ-ATP by selective RF irradiation leads to partial saturation of Pi and phosphocreatine (PCr) if the time constant of the chemical exchange is not longer than the T_1 time. This can be observed in-vivo.

This means that if A is Pi and B is γ-ATP, $M_{zB}(t) = 0$. This simplifies (8.5) to

$$\frac{M_{zA}(t)}{M_{zA}^0} = \frac{1}{R_A T_{1A}} + \left[1 - \left(\frac{1}{R_A T_{1A}}\right)\right] e^{-R_A t}. \tag{8.13}$$

In case of a very long saturation, equation (8.13) becomes

$$\frac{M_{zA}(\infty)}{M_{zA}^0} = \frac{1}{R_A T_{1A}} = \frac{1}{1 + k_{for} T_{1A}}. \tag{8.14}$$

This can be rewritten as

$$k_{for} = \frac{M_{zA}^0 - M_{zA}(\infty)}{M_{zA}^0} R_A \tag{8.15}$$

or

$$k_{for} = \frac{1}{T_A^*} \frac{M_{zA}^0 - M_{zA}(\infty)}{M_{zA}^0}. \tag{8.16}$$

For ATP synthesis from Pi and ADP M^0zA becomes $M_{Pi,0}$ and $M_{zA}(\infty)$ becomes $M_{Pi,s}$. $M_{Pi,s}$ can be determined by selective irradiation at the γ-ATP resonance frequency during the recovery period of the sequence. $M_{Pi,0}$ can be determined in a second experiment where the saturation frequency is mirrored about the frequency of the Pi signal.

T_1^* is the effective longitudinal relaxation time under saturation condition. This can be measured in an inversion recovery experiment, for example, if magnetisation transfer is present during the inversion recovery period.

8.3. Muscle ATP Synthesis

^{31}P spectra of the skeletal muscle show ATP resonances, PCr, inorganic phosphate (Pi), phosphomono- (PME) and -diesters (PDE). There are underlying broad-line resonances from immobile phospholipids, too. A typical spectrum can be seen in Figure 8.2. The strongest signal is that of PCr at 0 ppm. It is a singlet line and assumed to be independent of pH. α-ATP resonates at ~ -2.5 ppm, β-ATP at ~ -7.5 ppm, and γ-ATP at ~ -16 ppm. Pi resonates at around 5 ppm.

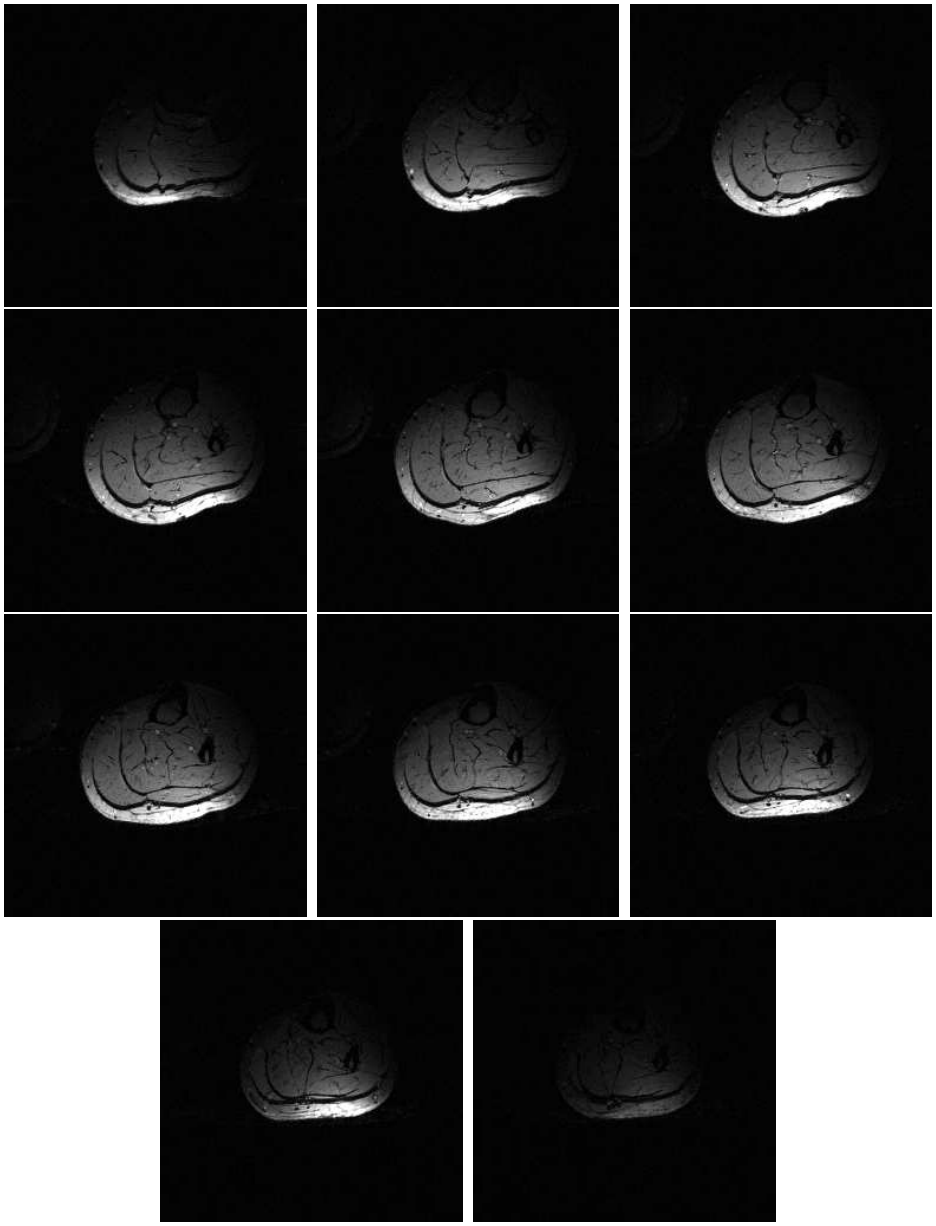

Figure 8.1.: Axial gradient echo images of lower leg acquired with the surface coil which is also used for the ^{31}P measurements. The images are acquired in 3 min with a field of view of 20 cm and 256 x 256 matrix size. $T_R = 0.34$ s, $T_E = 17$ ms.

Both of the following (simplified) reactions take place at the same time:

$$Pi + ADP \leftrightarrow ATP \tag{8.17}$$

$$PCr + ADP \leftrightarrow ATP + Cr \tag{8.18}$$

There is, however, no direct pathway to form PCr from Pi and ADP. The formation of ATP happens most frequently in mitochondria through oxidative phosphorilation, catalysed by various enzymes, whereas ATP hydrolysis happens at different locations, i.e., sites of energy consumption, as for example the myofibrils [124].

8.3.1. Muscle ^{31}P Spectroscopy of the Lower Leg

The human calf muscle was chosen because it is easily accessible and a relatively big muscle where no sophisticated localisation scheme needs to be applied.

The lower leg muscle was placed on a 10 cm linear polarised surface coil that is tuned to both the ^{1}H and ^{31}P frequencies. Gradient echo images are shown in Figure 8.1. The subcutaneous fat is seen as hyper-intense layer around the gastrocnemius muscle. The median and the lateral head of the gastrocnemius muscle are clearly distinguishable. More to the centre of the leg one can see the soleus muscle. The actual volume of interest depends on the size and shape of the subject's calf muscle and its filling of the sensitive volume of the coil. It can vary substantially between subjects, it is, however, in the range of several 100 ml.

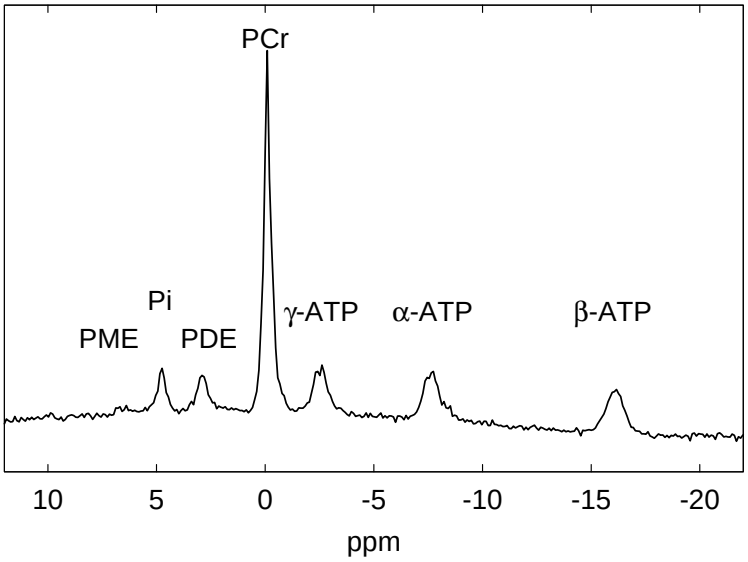

Figure 8.2.: ^{31}P spectrum of human calf muscle acquired at 3 T in 8.5 min.

8.3.2. The Pulse Programs

The eleven slices acquired and shown in Figure 8.1. cover the sensitive volume of the coil. Since the ^{1}H and ^{31}P coil loops have the same geometry, we assume that the ^{31}P

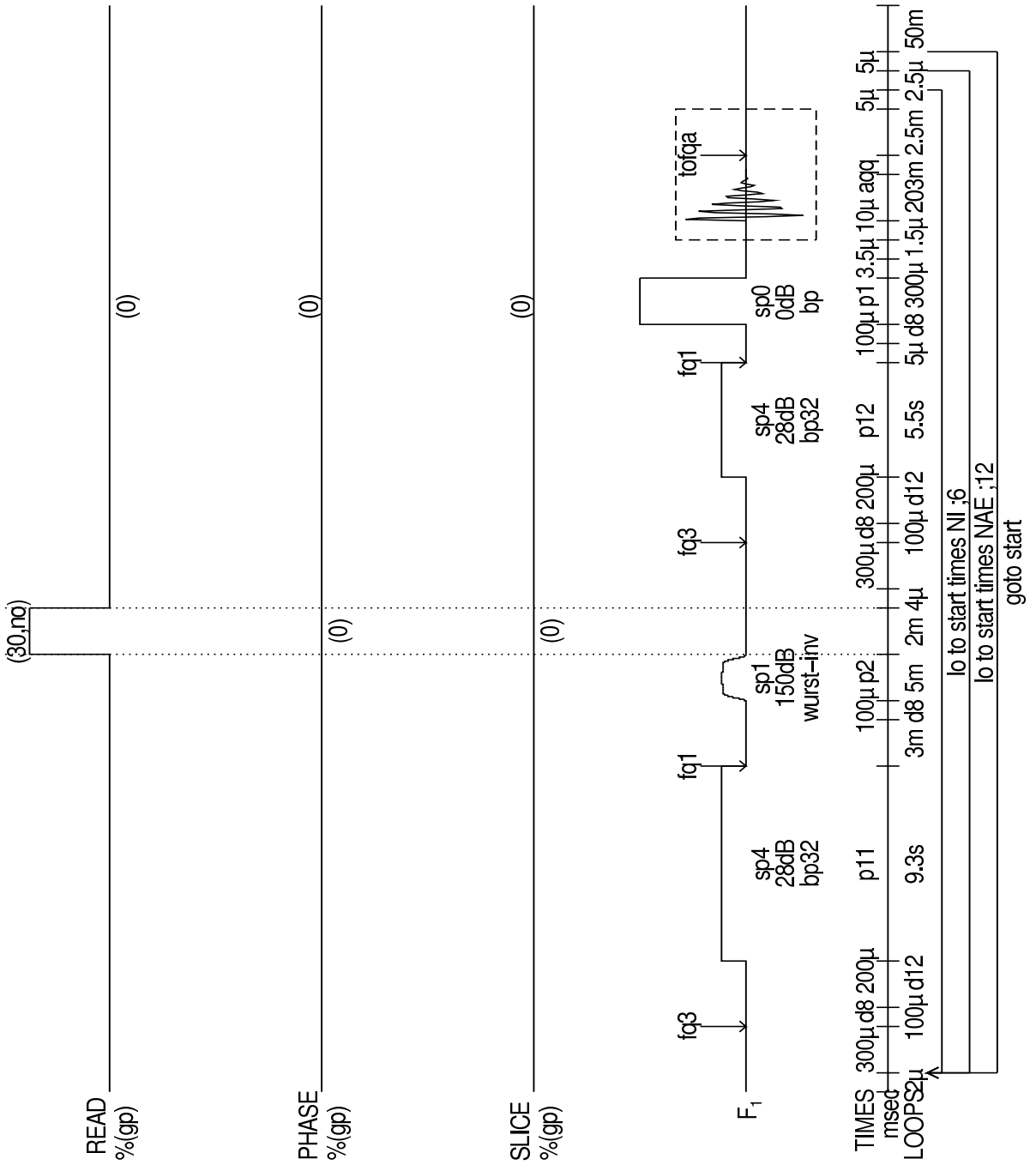

Figure 8.3.: Pulse program of the saturation transfer experiments. The signals are acquired in an interleaved manner.

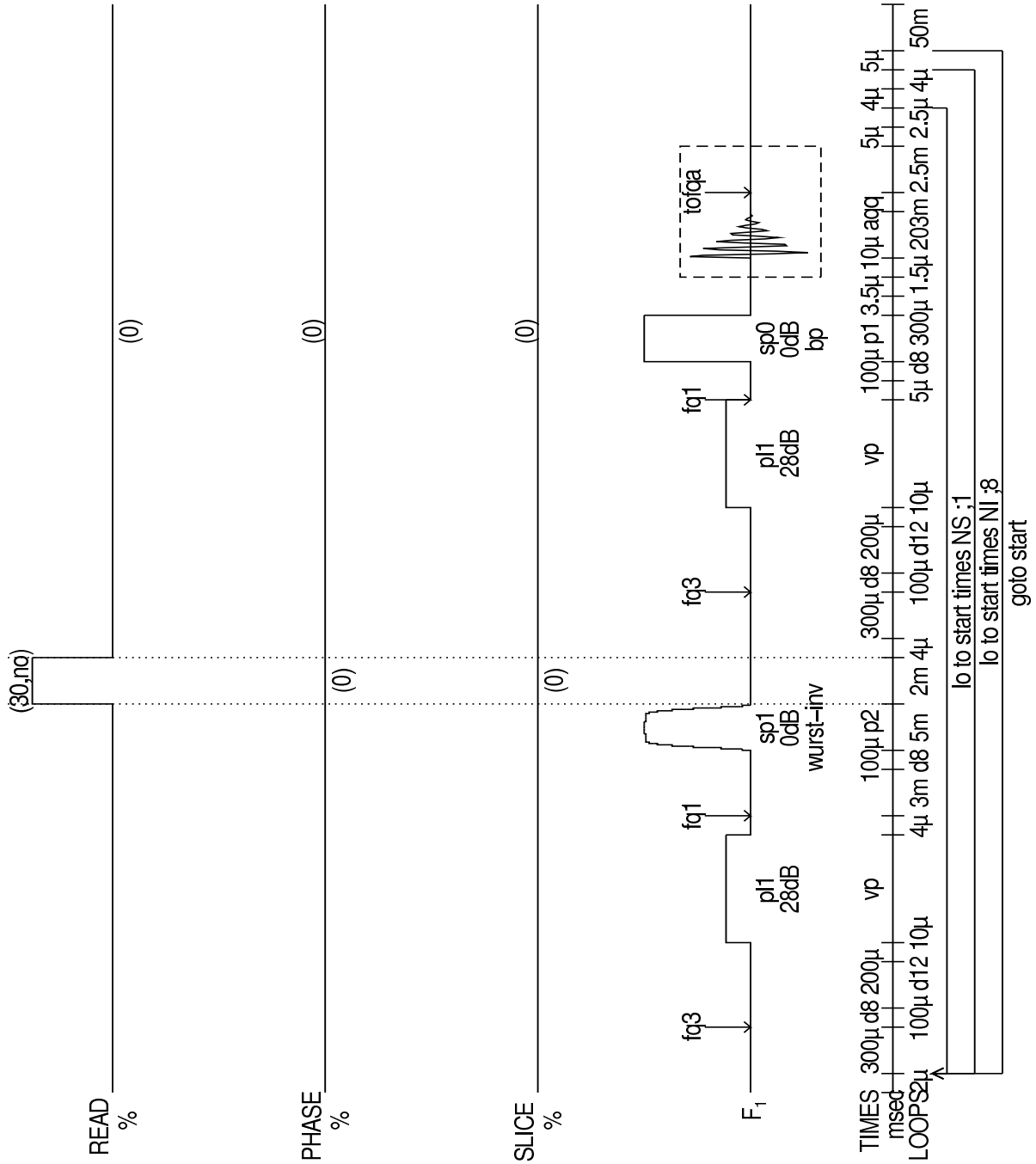

Figure 8.4.: Pulse program of the T_1 measurements. The program iterates over different inversion times. Averaging can be done inside and outside the loop.

signal shows a similar distribution, originating mostly from gastrocnemius and soleus muscle.

The saturation transfer experiment consists of several scans:

- A pulse-acquire experiment to determine the metabolite ratios and concentrations.
- A scan with selective saturation of the γ-ATP signal. This gives the signals $M_{Pi,s}$ and $M_{PCr,s}$.
- One scan with saturation turned on but the irradiation frequency mirrored about the Pi and PCr resonance frequency, respectively, which give the signals $M_{Pi,0}$ and $M_{PCr,0}$.
- A series of scans to determine the apparent T_1 relaxation time, T_1^*.

The pulse program for the saturation transfer experiment is shown in Figure 8.3. Continuous wave irradiation over the whole recovery period is applied by pulses p11 (sp11) and p12 (sp12). The sequence contains also an inversion pulse which is turned off, however.

The saturation transfer experiment requires at least two scans with saturation on; one at the frequency of γ-ATP and the other at a frequency mirrored about the Pi or PCr resonance. Considering the fact that in the end one uses the difference of the two, makes the experiment vulnerable to temporal instabilities and motion. Therefore, the acquisition scheme was not sequential but rather interleaved as can be seen in Figure 8.3, indicated by the loop over 'NI', which iterates over a list of saturation-frequencies (ACQ_O2_list) before averaging. This ensures that $M_{Pi,s}$ and $M_{PCr,s}$ as well as $M_{Pi,0}$ and $M_{PCr,0}$ are all acquired before averaging takes place.

A special modification of the above pulse program was made for the inversion recovery experiment to determine T_1^*. Since there is an overhead of about 30 s, when starting a new scan, variable length saturation pulses (vp) were used instead and the acquisition scheme organised accordingly so that all scans for the desired inversion times could be acquired without interruption or operator interaction. The NI counter loops over a list of prepared pulse lengths (ACQ_vp_list) of the variable length pulses that implement the correct inversion time.

The inversion pulse is an adiabatic full passage pulse of the WURST shape [108] and a duration of 5 ms.

8.4. Liver Spectroscopy and ATP Synthesis

Liver tissue has quite distinct properties, as well magnetically as physiologically, compared to muscle or adipose tissue. The same coil as described for muscle ^{31}P spectroscopy is used also for the liver measurements. It is attached to the lateral aspect of the liver and secured by adjustable straps. The patient lies supine, head first, in the scanner with the coil centre positioned in an axial slice through the isocentre of the magnet. Depending on the subjects' stature the sensitive volume of the coil is considerably shifted off-centre

to the top-left corner of the magnet. Axial and oblique (Figure 8.5) images are acquired to check the coil placement and select the VOI. Typically, the distance between the coil and liver is between 2 cm and 2.5 cm.

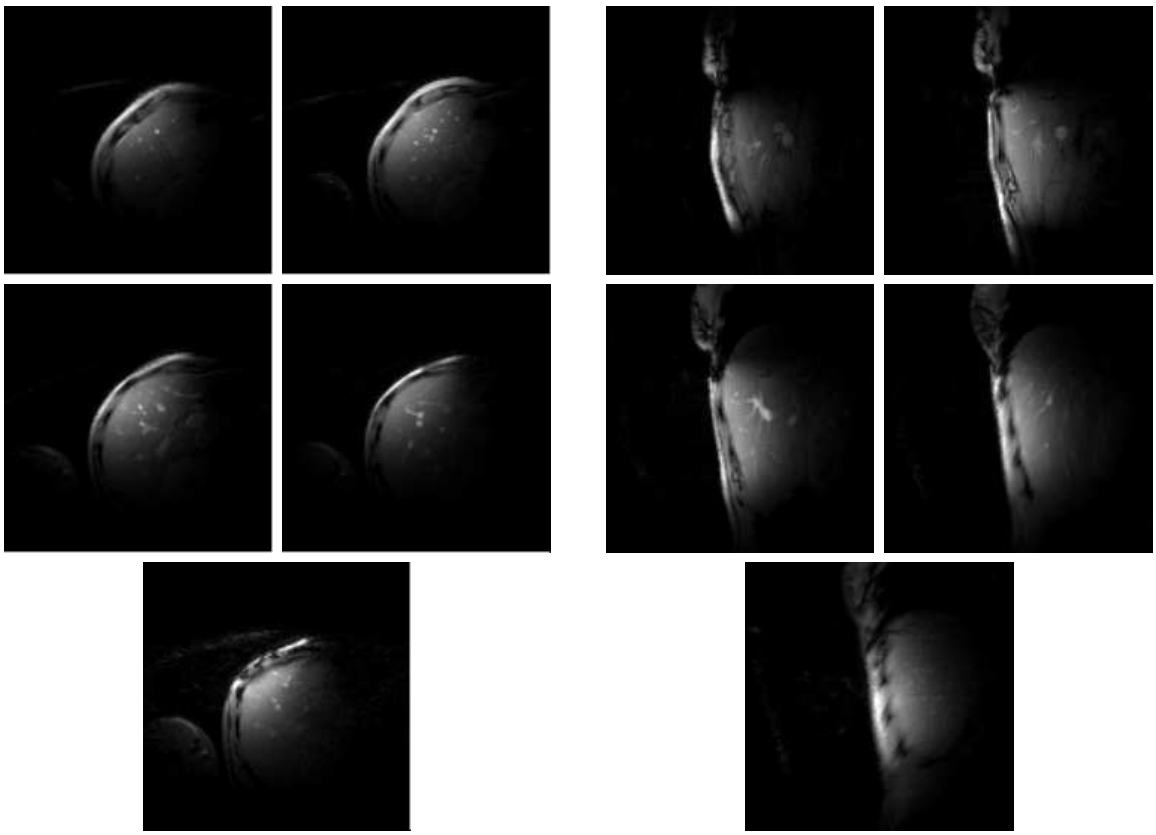

Figure 8.5.: Axial liver images acquired within one breath-hold (left). Oblique liver images, in a plane perpendicular to the axial plane, acquired within one breath-hold (right). Acquisition parameters: Five slices, $T_E = 15\,\text{ms}$, $T_R = 130\,\text{ms}$, FOV=25 cm, 128 x 128 matrix size.

To improve B_0 magnetic field homogeneity, linear shimming was performed using the proton signal of the surface coil. The automated non-localised procedure provided by the manufacturer was used. The spectral quality was further improved by manually adjusting the shim currents interactively based on signal from a cubic volume of interest exclusively placed into the liver. The ($30\,\text{mm}^3$) voxel was selected using STEAM [76] localisation ($T_E = 20\,\text{ms}$, $T_R = 2.5\,\text{s}$, $T_M = 30\,\text{ms}$). Manual shimming was performed during free breathing of the volunteers, observing several signal acquisitions to average fluctuations over breathing cycles.

The full width at half maximum of the water line could be up to 100 Hz before the shim correction and varied between above 10 Hz and below 40 Hz afterwards. This was verified by a scan acquired during breath-hold.

From the same volume, the HCL content was determined. A single scan without water

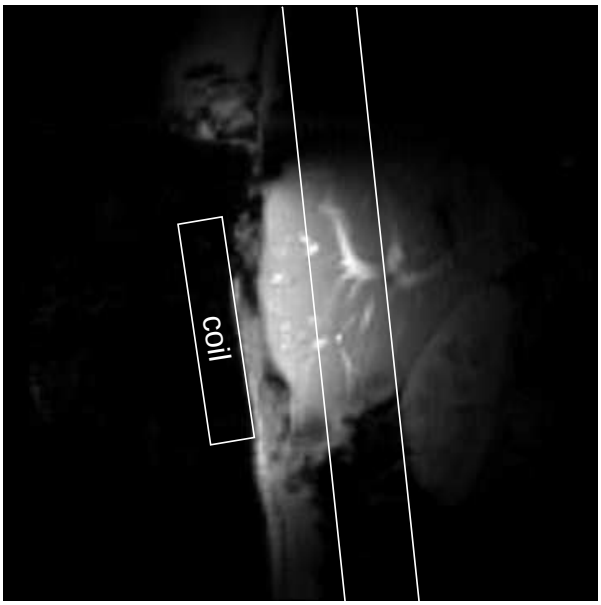

Figure 8.6.: Liver image schematically showing the coil placement. The 30 mm slab, which is the volume of interest, is indicated by the two parallel lines.

suppression was acquired during breathhold for five different echo times (i.e. 15, 20, 30, 50 and 70 ms, T_M=30 ms) each.

A localisation scheme is required that gives high signal to noise ratio per unit time, so a large volume of interest is desirable. That, however, is only fully advantageous if the B_0 homogeneity over the volume of interest is sufficient.

Echo based localisation schemes like STEAM or PRESS [75] are not suitable because of the high paramagnetic content of liver tissue and the resultant short T_2 relaxation times. Chemical shift imaging is too time consuming and the online verification of results is not possible, spectral quality and other errors or misadjustments can only be detected after the measurement session has finished.

This basically leaves ISIS [77] or DRESS [125]. ISIS gives fully three dimensional volume selection. Slice selective 180 ° pulses in combination with an add-subtract scheme (see Table 4.2). DRESS consists of a slice selective 90 ° pulse and a short refocusing gradient followed immediately by the acquisition. In this study a combination of both ideas was used, namely a one dimensional variant of ISIS with a double-oblique slice parallel to the coil plane in combination with the sensitivity profile of the surface coil. The setup and the VOI selection is best illustrated in Figure 8.6.

8.4.1. The Pulse Program

The 1D-ISIS pulse sequence is shown in Figure 8.7. The inversion pulse is a B_1 insensitive pulse of the WURST shape [108] of duration 5 ms. It has a bandwidth of 3700 Hz. The excitation pulse is a rectangular pulse of duration 0.45 ms. The excitation pulse was

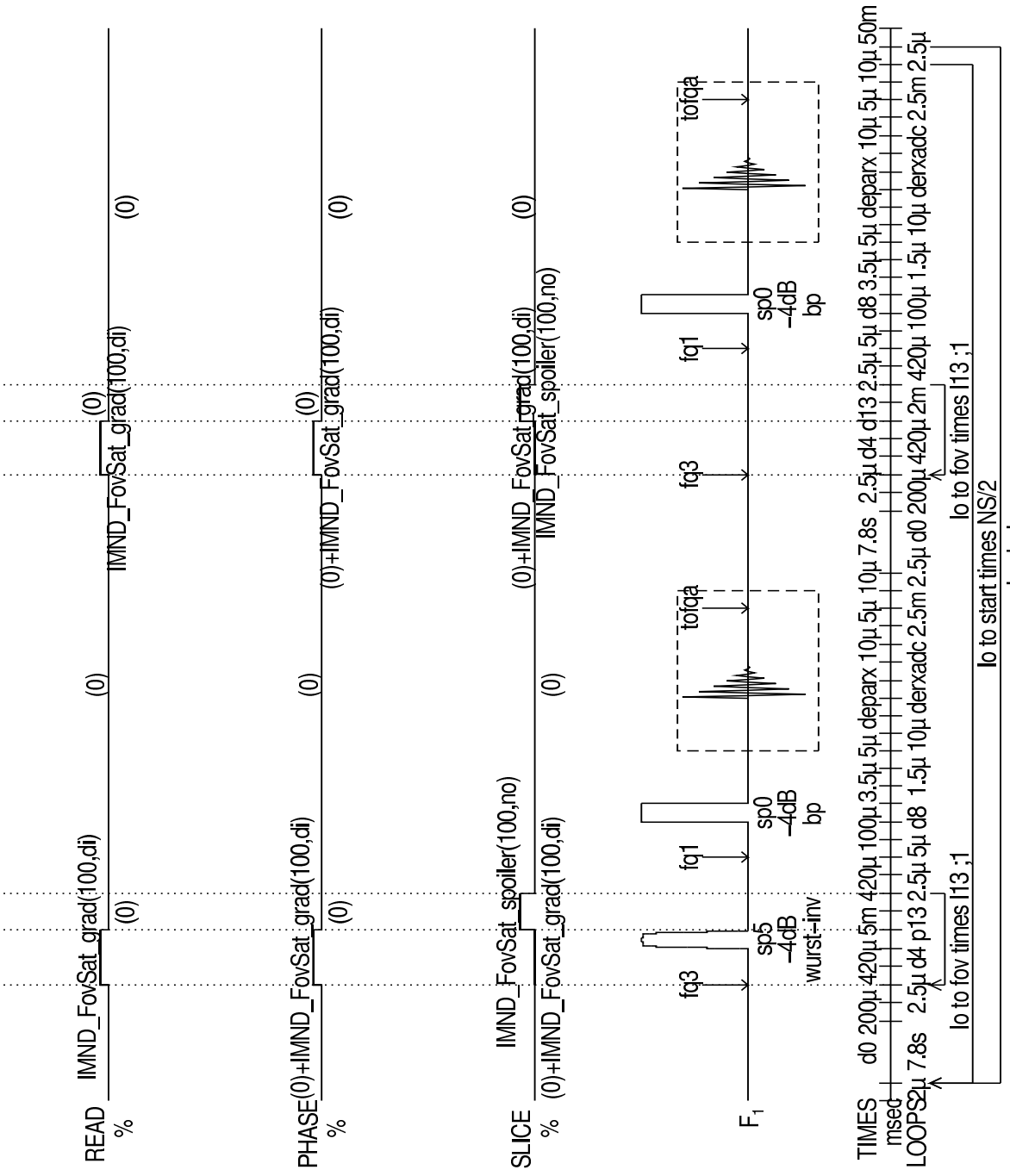

Figure 8.7.: Pulse program of the 1D-ISIS sequence.

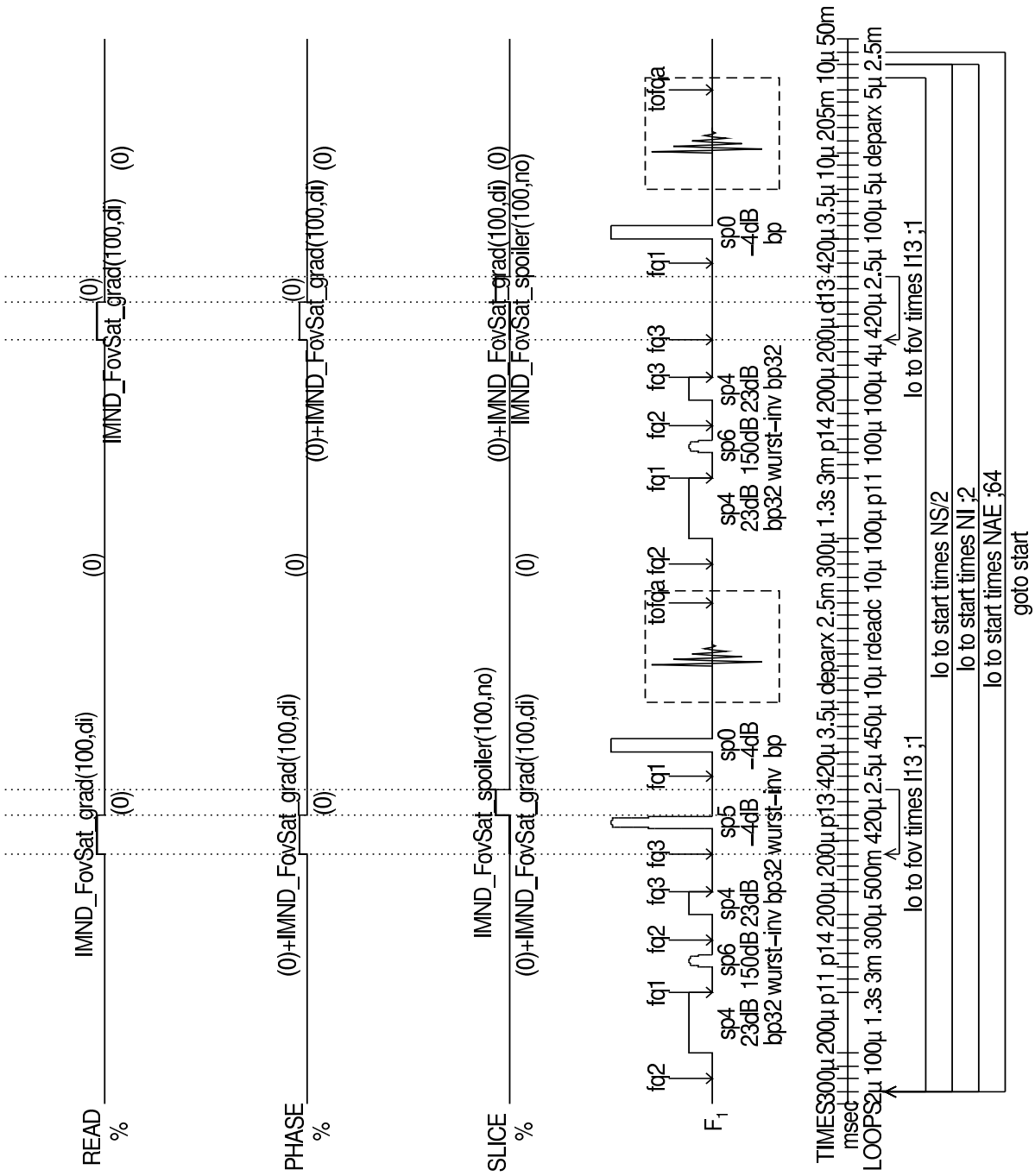

Figure 8.8.: Pulse program of the saturation transfer experiments. The signals are acquired in an interleaved manner.

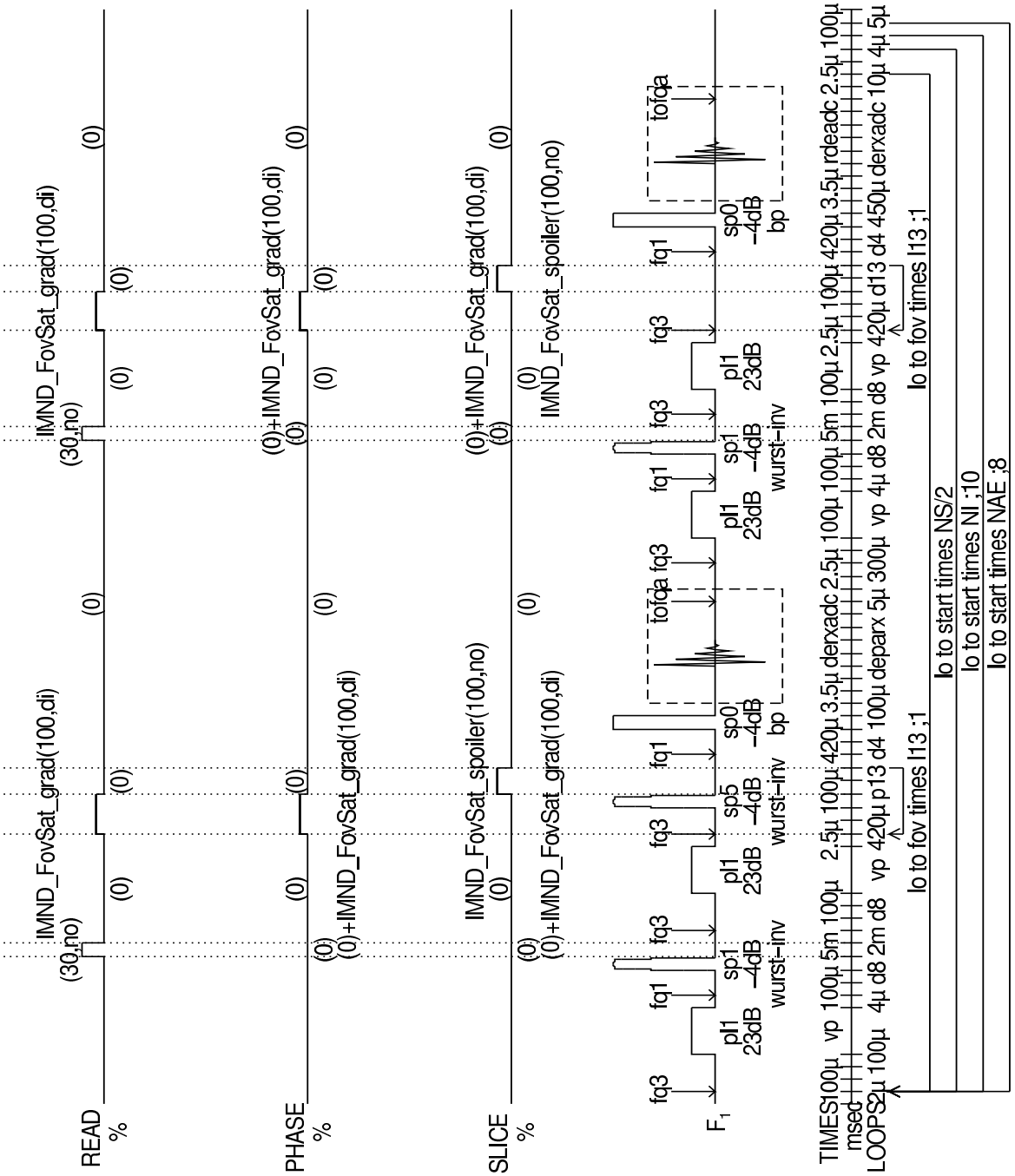

Figure 8.9.: Pulse program of the T_1 measurements. The program iterates over different inversion times. Averaging can be done inside and outside the loop.

chosen to generate a 90° flip angle in a distance of three to five cm away from the coil to improve the signal localisation. An adiabatic half passage pulse with the necessary bandwidth operating at a low B_1 field strength was not available. No respiratory triggering was active. The volume of interest (VOI) was confined in the other two dimensions by the boundaries of sensitivity of the coil.

Based on the proton images, a 30 mm slice (Figure 8.6) approximately parallel to the coil was selected to cover liver tissue. The resulting sensitive volume was approximately 35 x 35 x 30 x π mm^3 or 115 ml. The largest chemical shift displacement relative to the coil plane is that of β-ATP, approximately -16 ppm, or 6 mm.

For the saturation transfer experiment the basic pulse sequence in Figure 8.7 was extended by the saturation transfer elements, very similar as to those in the previous chapter (Figures 8.3 and 8.4). The complete sequences of both combined 1D-ISIS plus saturation transfer and 1D-ISIS plus inversion transfer are shown in Figures 8.8 and 8.9.

As with the pulse-acquire versions, the acquisition scheme is interleaved. Averaging takes places after looping over the saturation frequencies or the inversion times if this is wanted. This occurs outside the two step phase cycle required by the add-subtract cycle for the localisation. Thus, the number of acquisitions for a saturation transfer experiment including the control experiment with the saturation frequency mirrored has to be a multiple of four.

8.4.2. ^{31}P Spectra from Human Liver

The most obvious difference between muscle and liver spectra is the absence of the otherwise predominant PCr signal at 0 ppm, as one can see in Figure 8.10. This is because liver cells do not express the creatine kinase enzyme, under normal conditions. The three ATP resonances are present as well as inorganic phosphate (PI). Phosphomono- and -diesters are present at higher concentrations than in muscle. α-ATP has a significant contribution from NADP metabolites. A small signal at $\sim$-9.6 ppm is assigned to uridinediphosphoglucose (UDPG).

Lines are in general broader and the SNR is lower than in muscle spectra. Fortunately, T_1 relaxation times are relatively short, so the repetition times can be kept short. Especially in the PDE spectral region an underlying broad-line resonance from phospholipids distort the baseline.

The chemical shift of Pi is different in liver, $\sim$5.2 ppm vs. $\sim$4.8 ppm because the pH is typically higher in liver than in muscle tissue.

The β-ATP signal appears higher than γ-ATP arising from the chemical shift displacement. The gradient polarity is such that the negative offset frequencies are shifted closer to the coil, thereby contributing stronger to the total signal. Since β-ATP has the highest absolute value of the chemical shift or frequency offset, the effect is biggest for this resonance.

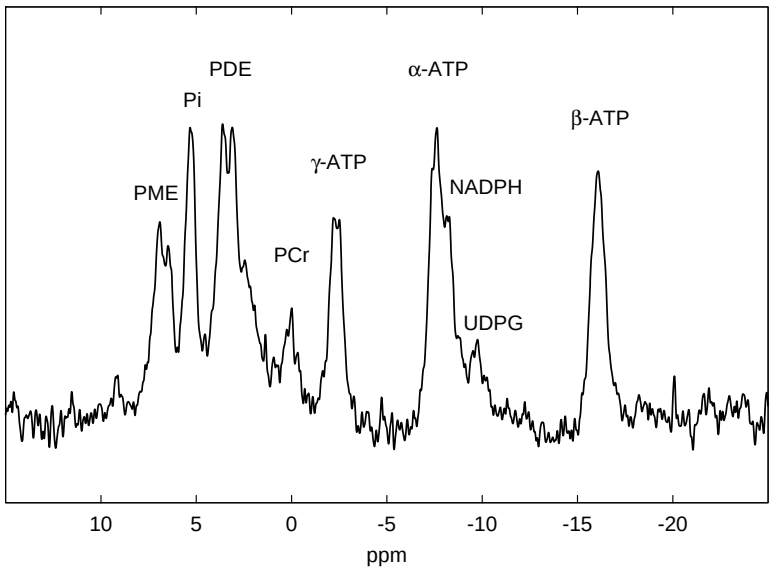

Figure 8.10.: ^{31}P spectrum acquired in 8.5 min (64 averages, T_R=8 s), localised with 1D-ISIS and a 10 cm diameter surface coil at 3 T. The contamination from muscle tissue, visible by the residual PCr signal is very small. Considering that this is the predominant signal in muscle ^{31}P spectra, being one order of magnitude bigger than the other resonances, the effect of residual muscle signal on the other metabolites is negligible (<5 %).

9. Quantification of ^{31}P Spectra

In general, quantification of in-vivo spectra is a challenge and must be done with great care. Especially if the signals were acquired from tissue with inherent anisotropy and the resulting ordering effects. Examples are overlapping resonances from IMCL and EMCL in muscle or motion, resulting in broader lines in liver. In-vivo spectra are often subject to artifacts, degenerated lines or other inconveniences like, for example, a large phospholipid background signal.

There are several ways how to achieve quantification of ^{31}P spectra. All of them require, however, some sort of operator interaction, at least evaluation of the fit results.

1. Manual preprocessing and picking the peak amplitude (frequency domain).
2. Manual preprocessing and integrating over the peak area.
3. (Semi-) automatic preprocessing and spectral modelling (fitting) in the frequency domain.
4. Time domain modelling and fitting.

Method 1 is probably the most stable to observe changes of a signal over time or under different conditions within one measurement session. If, however, T_2^* – or the line width – is not known or cannot easily be obtained from the spectra, absolute metabolite concentrations cannot be obtained.

Method 2 allows quantifying signals if a reference signal is present. Since in-vivo lines may be broad, degenerate and often overlap, integration is, in general, not very accurate. Also, setting a proper baseline is difficult and small errors in the setting has a relatively high impact on the quantification result.

Line fitting in the frequency domain of ^{31}P data is possible. LC-Model [126], however, a quasi gold-standard, is not applicable since it assumes fixed relative frequencies, an assumption not valid for several ^{31}P metabolites as they are pH dependent.

A completely different approach is quantification of signals directly in the time domain (Method 4). Although it is barely directly interpretable by the operator, it contains the same information as the spectrum. The model functions are often more simple in the time domain. Broad signals can be eliminated by disregarding the first few points in the FID. A more in-depth review can be found in [127].

9.1. Quantification of Muscle Spectra

Exemplary ^{31}P spectra from skeletal muscle (Figure 8.2) and liver (Figure 8.10) are shown. The muscle spectrum is dominated by the PCr resonance and in general lines

Table 9.1.: Model and starting values for the AMARES quantification of ^{31}P Muscle spectra

Peak name	frequency [ppm]	Line width [Hz]
Pi	4.8	10
PCr	0.0	10
PDE	3.0	10
PME	6.5	10
α-ATP	-7.5	10
β-ATP	-16.0	10
γ-ATP	-2.4	10

Table 9.2.: Prior knowledge used for the quantification of ^{31}P muscle spectra

Signal	property	relative to	value
All	model function	-	Gaussian
PDE, PME, PCr	phase	Pi	0
α-ATP, β-ATP	phase	γ-ATP	0
γ-ATP	line width	α-ATP	0
all	frequency	-	Soft constraints
-	phase	-	constant
-	begin time [1]	-	set to .23 ms

Table 9.3.: AMARES model and results (peak area) on an exemplary human muscle dataset. The β-ATP resonance is set to 5.5 mM. The leftmost column identifies the metabolite. All lines were fitted against Gaussian model functions. The applied constraints can be seen in equal line widths and phases of several resonances. As this is a time domain fit, the amplitude is equivalent to the peak area. The phase is relative to a constant overall constant and linear phase (begin time).

Resonance	Frequency [ppm]	Linewidth [Hz]	Peak Area [mM]	Phase [°]
Pi	4.933	13.34	1.57±0.05	-6.9
PDE	2.949	21.88	1.01±0.06	-6.9
PME	6.748	19.21	0.34±0.05	-6.9
γ-ATP	-2.412	23.41	3.73±0.06	-9.6
β-ATP	-16.619	28.51	5.50±0.07	-9.6
α-ATP	-7.554	23.41	5.25±0.06	-9.6
PCr	0.031	12.35	17.02±0.04	-6.9

do not overlap. So the signal quantification is more or less straight forward.

For metabolite ratios method 2, i.e. peak integration, was used. For computation of the exchange rate constant method 1, i.e. peak amplitude, was used because only differences of signals were needed, and it is the most robust.

Similar results are obtained if a time domain fit is used, in this case using the MRUI software package [128] and the AMARES algorithm [129]. PMEs and PDEs are more difficult to quantify because of their low signal to noise ratio, the results are less reliable than for bigger resonances.

The results of the quantification of a typical spectrum acquired from calf muscle are shown in Table 9.3.

9.2. Quantification of Liver Spectra

Table 9.4.: Model and starting values for the AMARES quantification of ^{31}P human liver spectra

Peak name	Frequency [ppm]	Line width [Hz]
Pi	5.3	10
PDE-1	3.2	10
PDE-2	2.3	10
PME-1	6.4	10
PME-2	7.0	10
α-ATP	-7.4	10
β-ATP	-16.0	10
γ-ATP	-2.3	10
NADP	-8.2	10
UDPG	-9.6	10

Quantification of the liver spectra can be challenging because there are many resonances between zero and eight ppm, some of them doublets, which partially overlap, and an underlying broad line further complicates the spectrum. Also, motion has to be taken into account, leading to partial degeneration of the Lorentzian lines, to lower SNR and to drifts in resonance frequency and phase. In the saturation transfer experiment, temporal stability between successive scans is very important, similar to the inversion recovery experiment. In our experience, using manual processing in the frequency domain, baseline setting and picking the amplitude of the Pi appeared to be more reliable than AMARES time domain fitting, where small variations, especially in the line width, led to stronger fluctuations than amplitude quantification. For the same reason we preferred manual processing of the spectra also for the T_1 measurements. Time domain signal fitting is not very useful for the quantification of inversion recovery data, as suitable constraints on phases are not feasible and the SNR is too low in some spectra to produce reliable

Table 9.5.: Prior knowledge used for the quantification of ^{31}P liver spectra

Signal	Property	Relative to	Value
All	model function	-	Gaussian
PDE, PME	phase	Pi	0
α-ATP, β-ATP, NADP, UDPG	phase	γ-ATP	0
GPC	line width	GPE	0
PC	line width	PE	0
α-ATP, UDPG	line width	NADPH	0.5[2]
all	frequency	-	Soft constraints
-	phase	-	set manually
-	begin time [3]	-	set to .25 ms

Table 9.6.: AMARES model and results (peak area) on an exemplary human liver dataset. The γ-ATP resonance is set to 2.5 mM. The left column identifies the metabolite: Phosphomono- and -diesters are fitted as two separate lines each. All lines were fitted against Gaussian model functions. The applied constraints can be seen in equal line widths and phases of several resonances. As this is a time domain fit, the amplitude is equivalent to the peak area. The phase is relative to a constant overall constant and linear phase (begin time).

Resonance	Frequency [ppm]	Line with [Hz]	Peak area [mM]	Phase [°]
Pi	5.366	17.43	1.38±0.06	-13.3
PDE-1	3.459	37.56	1.54±0.16	-13.3
PDE-2	2.437	37.56	0.71±0.10	-13.3
PME-1	6.467	23.95	0.62±0.08	-13.3
PME-2	7.104	23.95	0.68±0.10	-13.3
γ-ATP	-2.208	20.12	2.50±0.05	-18.1
β-ATP	-15.996	25.69	3.23±0.06	-18.1
α-ATP	-7.404	24.74	3.50±0.07	-18.1
NADPH	-8.251	21.28	0.64±0.05	-18.1
UDPG	-9.478	24.74	0.33±0.05	-18.1

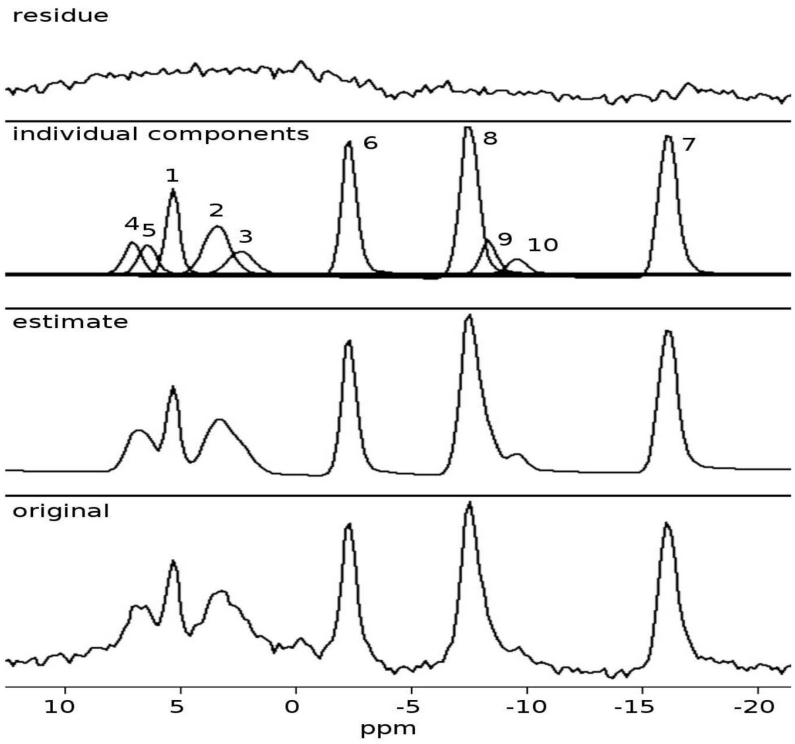

Figure 9.1.: Example of the AMARES quantification (see also Table 9.6). From bottom to top: Original dataset; fit result; individual model components (1 Pi, 2,3 PDE, 4,5 PME, 6,7,8 ATP, 9 NADPH, 10 UDPG); residual spectrum.

results. For the quantification of relative metabolite concentrations from spectra without inversion recovery and saturation transfer, however, a more sophisticated approach is necessary. The prior knowledge introduced here (see Tables 9.4 and 9.5) is a purely empirical attempt to model the data. The prior knowledge set was tested on one dataset and afterwards applied to all others with satisfying results in all spectra processed. It is of note that a similar prior knowledge based on Lorentzian line shapes was tested but did not produce stable results.

Very satisfactory results were achieved with the AMARES algorithm using the basis set and prior knowledge summarised in Tables 9.4 and 9.5. The liver spectrum is modelled with Gaussian rather than Lorentzian line shapes, indicating that there are effects of motion and possibly other factors leading to degenerated spectral lines.

Concentrations of liver metabolites are referred to an assumed ATP concentration of 2.5 mM [130] as an internal reference. Since the chemical shift of β-ATP is much larger than that of γ-ATP and the concentration of ADP is very low, the γ-ATP resonance is used rather than that of β-ATP.

An example of the fit, model, estimate and residue, is displayed in Figure 9.1. Detailed results for the same dataset are shown in Table 9.6.

10. Skeletal Muscle ATP Synthesis Rates

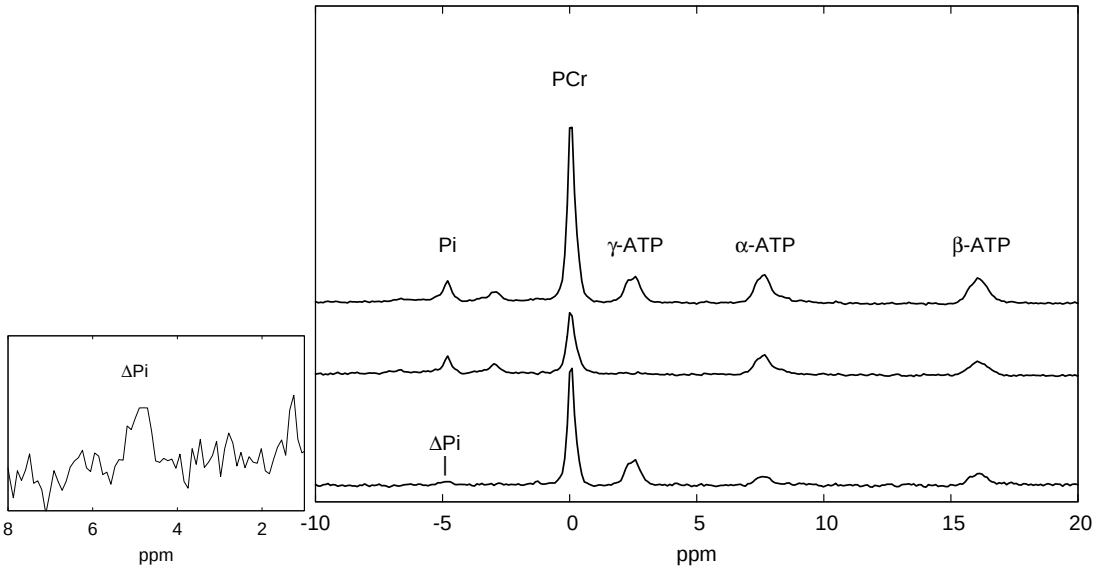

Figure 10.1.: ^{31}P spectra obtained from calf muscle during the saturation transfer experiment (2 x 16 averages, 8.5 min); Top: Spectrum where the saturation frequency was mirrored about the resonance of inorganic phosphate (Pi) with Pi and all three ATP resonances. Middle: Spectrum with selective saturation of γ-ATP which is therefore absent. Bottom: The difference spectrum. Small Frame: The area of the ΔPi signal of the difference spectrum is displayed magnified.

The skeletal muscle ^{31}P saturation transfer experiment has successfully been applied to both the measurement of creatine kinase and mitochondrial ATP synthase activity. Based on the experience with measurements by Brehm et al. [67], improvements to the measurement protocol have been made. Especially the introduction of an interleaved acquisition scheme improved the reproducibility of the data and allowed for the reduction in overall measurement time.

In Table 10.1 some of the measured data on healthy volunteers are summarised. So, far, at least a hundred volunteers have been measured using this protocol. These include patients with overt diabetes mellitus, type 1 and type 2, women with past gestrational

Table 10.1.: Skeletal muscle rates of ATP synthesis. Both rates from the reaction ADP + Pi → ATP catalysed by ATP synthase and PCr + ADP → Cr + ATP catalysed by creatine kinase. The equilibrium exchange constant, the concentration of either PCr or Pi and the unidirectional exchange rates are shown. Study A shows yet unpublished data of measurements in eight healthy women who served as a control group to women with past gestrational diabetes mellitus. Study B shows values of young, healthy, lean males and females (baseline values from group CONy in [68].

	ATP synthase			creatine kinase		
Study	k [s^{-1}]	[Pi] [mM]	Rate [mM/min]	k [s^{-1}]	[Pi] [mM]	Rate [mM/min
A	0.067	3.28	13.16	0.28	17.85	300.2
A	0.077	2.33	10.82	0.31	15.26	280.4
A	0.061	2.84	10.36	0.29	20.48	358.1
A	0.078	3.02	14.08	0.32	20.52	391.3
A	0.078	2.42	11.33	0.28	18.70	314.0
A	0.079	2.54	12.03	0.30	17.87	322.4
A	0.067	3.45	13.86	0.38	21.76	492.9
A	0.069	2.71	11.26	0.33	20.14	393.7
B	0.057	3.19	14.60	0.36	18.09	389.6
B	0.073	2.92	12.50	0.35	19.81	420.7
B	0.097	2.52	14.60	0.28	18.91	313.2
B	0.060	2.48	10.70	0.28	15.54	260.1
B	0.046	2.80	10.50	0.31	17.10	319.1
B	0.048	2.33	8.10	0.25	16.31	243.7
B	0.059	2.87	11.80	0.33	20.97	410.1
B	0.067	2.64	11.70	0.36	17.78	385.2
B	0.064	2.86	11.50	0.29	18.32	317.1
B	0.034	2.84	5.50	0.28	19.55	333.3
B	0.072	3.36	17.70	0.36	19.22	413.2
Mean	0.066±0.003	2.81±0.08	11.90±0.60	0.31±0.01	18.64±0.41	350.4±14.5

diabetes, acromegaly, and subjects who are the offsprings of patients with type 2 diabetes mellitus.

The measurements were done under fasting conditions, and with interventions like a hyperinsulinemic glucose clamp test, hyperlipidemia or before and after exercise. Some of the data has already been published [67,68], all except the most recently acquired data have been presented at high ranking international conferences, like the annual meeting of the international society in magnetic resonance (ISMRM), the European society in magnetic resonance in medicine and biology (ESMRMB), besides international scientific meetings of diabetologists since 2005. Several publications are currently under review or in preparation.

If we follow the discussion in [68], skeletal muscle insulin resistance is characteristic

in the elderly as well as in persons at increased risk of type 2 diabetes mellitus (T2DM) and those with overt T2DM. In these groups, the content of intramyocellular lipids (IMCL) is frequently increased and related to insulin resistance [41, 131]. In severe obesity and moderately controlled T2DM, insulin resistance has been linked to abnormal mitochondrial function of skeletal muscle as assessed by in vitro and ex vivo examination in biopsies [46, 47, 132]. Application of magnetic resonance spectroscopy (MRS) made it possible to noninvasively examine myocellular mitochondrial function by measuring rates of ATP synthesis in humans [133]. Insulin resistant elderly people and first-degree relatives of patients with T2DM have impaired muscle ATP production and elevated IMCL [24, 66].

These studies raised the questions of whether lipid accumulation in skeletal muscle and/or insulin resistance promotes mitochondrial dysfunction. If so, can insulin stimulation overcome such alterations? In this context, we recently showed that short-term elevation of plasma FFAs profoundly inhibits insulin-stimulated glucose transport/phosphorilation and mitochondrial function, reflected by diminished increase in intramyocellular glucose-6-phosphate and ATP synthesis, independently of ectopic muscle fat contents [67].

Baseline ATP synthesis was 27 % lower in patients with T2DM than in young control participants (8.6±0.6 mM/min vs. 11.8±1.0 mM/l, $p < 0.05$). The matched control group was in between and not significantly different from either T2DM or young controls (10.4±0.8 mM/min).

Insulin stimulated rates were higher than in the baseline measurement in all three groups, but not significantly in T2DM (young controls 14.8±1.3 mM/min, $p < 0.01$; matched controls 11.5±0.5 mM/min, $p < 0.05$; T2DM 9.5±0.9 mM/min $p = 0.26$). Patients with well-controlled insulin resistant T2DM have slightly lower ATP synthesis independent of glucose transport/phosphorilation and lipid deposition in muscle, lipid availability primarily determines baseline ATP synthesis, whereas insulin sensitivity defines insulin stimulated ATP synthesis.

Even a small degree of overweight and physical inactivity is associated with reduction in mitochondrial function, confirming the importance of lifestyle for development and prevention of insulin resistance and T2DM. Further research is needed, however, to delineate whether abnormalities in mitochondrial number and/or function are the cause or consequence of T2DM and to address the mitochondria as a target for novel therapeutic regimens. For more detailed results and discussions see [68].

Acromegaly generally results from slowly growing monoclonal pituitary adenomas secreting growth hormone (GH). As a result of its slow and often insidious onset, it frequently remains unrecognised for an extended time, which may give rise to sustained metabolic alterations. Patients with active acromegaly frequently exhibit mild hepatic and more pronounced muscular insulin resistance.

The patients with a history of acromegaly exhibit reduced insulin secretion and muscular ATP synthesis (9.4±0.8 mM/min vs. 12.6±0.9 mM/min, $p < 0.05$). Previous exposure to high IGF-1, lipids and/or glucose concentrations could be responsible for the induction of mitochondrial alterations in β cells and myocytes.

This summary of results of studies involving skeletal muscle ^{31}P saturation transfer

should illustrate that these experiments are not only experimentally feasible but of high value to metabolic research.

11. Hepatic ^{31}P T_1 Relaxation Times

Since no published T_1 values of hepatic ^{31}P signals had been available, these were measured on six male volunteers using the inversion recovery sequence (Figure 8.9). The saturation pulses, however, were turned off (the attenuator set to maximum damping).

Ten spectra with different inversion times between 50 ms and 4 s were acquired per subject. Also, an additional scan without inversion was done. The signals were individually fitted against the following model function

$$M(t) = M(0)/(1 - b\exp(-t/T_1)), \tag{11.1}$$

where t is the inversion delay, and b a factor that takes into account that experimentally it is usually not possible to achieve complete inversion despite the use of adiabatic pulses. Typical values ranged between 1.6 to 1.8, which is slightly less than the theoretical value of 2.

The spectra were quantified using peak amplitude picking as described in the previous chapter. The SNR was extremely low in some spectra. Therefore a total of ten inversion points were acquired. Also, the T_1 relaxation times vary significantly between metabolites as can be seen in Table 11.1 and varies between 0.4 s for ATP to almost 7 s for GPE. A paired student's t-test was used to compare PC to PE and GPC to GPE relaxation times. While there was no significant difference between the values for PC and PE ($p = 0.37$), there is a significant difference between the relaxation times of GPC and GPE ($p = 0.03$).

The measured values are in good agreement with previous studies performed at lower field strengths summarised in [134]. There is no obvious trend to longer T_1 times as discussed in [135].

These T_1 relaxation times on human liver are currently in press [74].

Table 11.1.: T_1 relaxation times [s], mean ± standard deviation. The two resonances visible for PDEs are assigned to GPC = glycero-phosphocholine and GPE = glycero-phosphoethanolamine, the resonances for PMEs to PC = phosphocholine, PE = phoshphoethanolamine, respectively.

Subject	Pi	PC	PE	GPC	GPE	γ-ATP	α-ATP	β-ATP
1	0.77±0.10	1.67±0.74	0.88±0.27	3.60±0.80	9.92±4.15	0.27±0.04	0.48±0.14	0.38±0.07
2	0.67±0.17	1.26±0.58	0.87±0.46	3.60±0.40	7.40±2.40	0.43±0.09	0.59±0.11	0.89±0.23
3	0.85±0.10	2.27±0.35	2.92±0.33	3.65±0.38	5.29±0.64	0.64±0.13	0.68 ± 0.12	0.65±0.07
4	0.51 ± 0.09	2.07±0.17	1.16 ± 0.3	3.97±1.1	4.83±0.70	0.30±0.03	0.45±0.10	0.43±0.09
5	0.48±0.06	3.72±1.5	1.71±0.49	4.19±0.47	4.96±2.1	0.43±0.16	0.66±0.17	0.47±0.07
6	1.07±0.23	2.46±1.7	3.33±0.56	6.54±2.1	9.46±3.2	0.48±0.13	0.59±0.15	0.50±0.08
	0.73±0.22	2.24±0.84	1.81±1.07	4.26±1.14	6.98±2.30	0.43±0.13	0.58±0.09	0.55±0.19
1.5-2.0T [134]	0.77	1.17		4.01		0.42	0.55	0.43

12. Hepatic Rates of ATP Synthesis

Taking together the results of the previous chapters, unidirectional flux from Pi to ATP was measured successfully in nine volunteers. A typical spectrum of the saturation transfer experiment is displayed in Figure 12.1. Figure 12.1 shows a spectrum with saturation (middle), one reference spectrum (top) and the difference spectrum (bottom). In the small zoomed part of the figure, the Pi region is amplified to allow for better visualisation of the effect of the magnetisation transfer. The individual results of the magnetisation transfer experiment including the apparent T_1 time, the relative signal reduction through magnetisation transfer ($1 - M_{Pi,s}/M_{Pi,0}$), equilibrium exchange rate constant k, concentration of Pi, and rate of ATP synthesis are summarised in Table 12.1. HCL are below 3 % in all subjects, which is typical for insulin sensitive normal weight humans.

The SNR of the spectra (256 averages acquired in about 8.5 min) after exponential filtering (10 Hz) was about 20 in all subjects. The uncorrected, with regard to partial T_1 saturation, signal difference between $M_{Pi,s}$ and $M_{Pi,0}$ is about 10 %. Typically 1024 transients could be acquired for both $M_{Pi,s}$ and $M_{Pi,0}$ leading to an individual ΔM_{Pi} to noise ratio of about four.

12.1. Discussion

The present work investigated the feasibility of the in-vivo ^{31}P saturation transfer experiment of the Pi-ATP exchange in the human liver at 3 T. Good localisation is a prerequisite, because overlying muscle tissue has metabolically and magnetically different properties compared to those of liver. One dimensional ISIS localisation allows for excellent specificity and high SNR. This has enabled estimation of the equilibrium exchange rate constant of the ATP synthesis reaction in a measurement session of about two hours, a tolerable time for most subjects.

Phosphorus spectra were acquired continuously, because respiratory triggering would have caused an unacceptable duration of the experiment. Effects of breathing motion could have broadened the spectral lines and changed them towards Gaussian lineshapes. However, the motion of the liver could be expected to occur mostly in-plane as the patient's motion was restricted by the coil holder and no significant contributions from muscle tissue were detectable in our experiments.

The mean equilibrium Pi-ATP exchange rate constant was estimated to be $0.30 \pm 0.02\,\mathrm{s}^{-1}$ in humans, compared to $0.38 \pm 0.03\,\mathrm{s}^{-}1$ in isolated perfused rat livers [73]. The standard errors indicate comparable precision in-vivo in humans and ex-vivo in perfused rat liver, measured at much higher field strength, where experimental conditions are much more

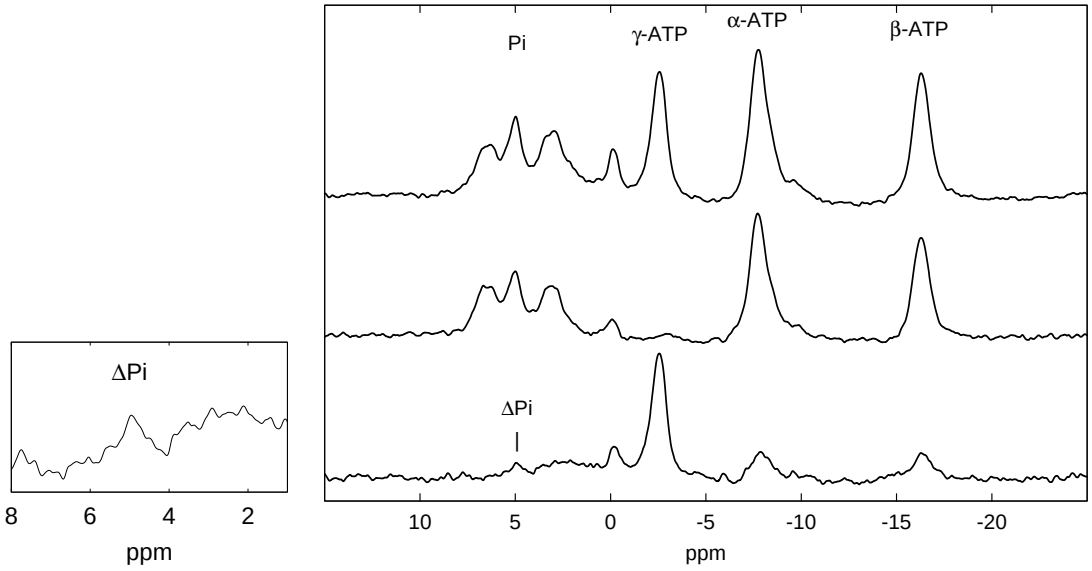

Figure 12.1.: ^{31}P spectra obtained from human liver during the saturation transfer experiment (2 x 1024 averages, 68 min); Top: Spectrum where the saturation frequency was mirrored about the resonance of inorganic phosphate (Pi) with Pi and all three ATP resonances. Middle: Spectrum with selective saturation of γ-ATP which is therefore absent. Bottom: The difference spectrum. Small Frame: The area of the ΔPi signal of the difference spectrum is displayed magnified ($\times \sim 5$).

Table 12.1.: The results of the saturation transfer experiments with and the hepatocellular lipid content (HCL) of nine subjects are shown. Apparent T_1^* relaxation time, the fractional signal reduction through magnetisation transfer (ΔM/M), the concentration of inorganic phosphate [Pi], the equilibrium exchange rate constant k and the ATP synthesis rate are shown for each subject.

Subject	T_1^* [s]	ΔM/M	[Pi] [mM]	k [s^{-1}]	Rate [mM$\times$$min^{-1}$]	HCL [% Signal]
1	0.50	0.173	1.68	0.35	35.02	1.07
2	0.55	0.138	1.71	0.25	25.98	0.56
3	0.50	0.164	1.59	0.33	31.28	1.26
4	0.58	0.150	1.59	0.26	24.46	2.82
5	0.48	0.149	1.73	0.31	31.94	1.95
6	0.41	0.143	1.57	0.35	32.80	1.82
7	0.49	0.127	1.58	0.26	24.60	0.70
8	0.50	0.189	1.65	0.38	37.17	1.94
9	0.62	0.139	1.66	0.22	22.22	1.29
Mean	0.52 $\pm$ .02	0.152 $\pm$ .006	1.64$\pm$0.02	0.30$\pm$0.02	29.49$\pm$1.77	1.49$\pm$0.24

favourable due to the absence of skeletal muscle and motion artifacts. Rates of hepatic ATP synthesis were 50 % lower than those in isolated perfused rat livers (64 mM liver/min) [73].

The HCL content was lower than 3 % in all volunteers, indicating a healthy liver without steatosis. The chemical shift displacement of fat relative to water is about 4.5 mm or 15 %. Water and fat signals, therefore, originate mostly from the same volume. The determination of HCL content in a similar fashion has been validated in vivo by Szczepaniak et al. [136].

Previously, indirect assumptions on hepatic ATP synthesis were made from changes in the phosphorus metabolite concentrations upon fructose administration [69] or from measurement of ATP concentration [62, 63]. ^{31}P MRS was applied to measure phosphorus metabolites upon administration of alanine, a gluconeogenetic precursor [72] or ethanol, which inhibits gluconeogenesis [71]. In any case, these studies did not provide quantitative estimates of flux through ATP synthase in liver.

In humans, ATP synthesis has been measured in skeletal muscle and found to range from 5 to 15 mM/min [24, 66–68], see also Chapter 10. ATP synthesis is approximately 12 mM/min in human visual cortex [137]. Such rates are three- to sixfold lower compared with those of hepatic ATP synthesis reported here.

Rates of ATP synthesis in human brain and muscle mainly reflect mitochondrial oxidation, whereas in the human liver it is not clear to what extent overall ATP production depends on the activities of the glycolytic and gluconeogenetic enzymes glyceraldehyde-3-phosphate dehydrogenase / 3-phosphoglycerate kinase as reported in the rat liver [73]. One study reported fasting splanchnic oxygen uptake of approximately 2.5 mmol O_2/min from arterio-venous balance experiments in young healthy volunteers [138]. Assuming a mean liver volume of 1.5 l and a ratio of ATP produced per oxygen atom (P/O ratio) of 2, allows to estimate oxidative ATP production to be approximately 7 mM/min. Thus, the net flux through mitochondrial ATP synthase would then account only for one fourth of the overall ATP synthetic rate measured by MRS. This is in agreement with the discussion in reference [73]. On the other hand, in hepatocytes depleted of mitochondrial DNA, and thus relying on anaerobic sources of ATP production, ATP synthesis was tenfold lower compared to hepatocytes with mitochondrial DNA [139], indicating that mitochondria markedly contribute to ATP synthesis in hepatocytes.

Baseline spectra showed a partial saturation of the Pi reference signal by ≈6 %, which then resulted in a 50 % decrease of the ΔPi signal in difference spectra. The mean T_1 value of the Pi resonance (Table 11.1) was used to correct for this. The limited accuracy of the Pi longitudinal relaxation time is a potential source of error for the results of the magnetisation transfer experiment since the difference ΔPi is more susceptible to errors.

In conclusion, a fast, high SNR localisation technique was implemented that allowed for the quantification of rates of hepatic ATP synthesis in human liver. Due to the simple and robust nature of the experimental design, this method is suitable for future clinical studies on hepatic energy metabolism, that will provide a better understanding of abnormalities underlying diseases like steatosis, insulin resistance and diabetes mellitus. The greater part of this work is also published in [74].

Summary and Outlook

There are several aspects in human energy metabolism that can be addressed by nuclear magnetic resonance. The aim of this work was to target specifically challenging aspects of cellular energy metabolism and provide the clinical researcher with appropriate experimental tools. In particular, the implementation, validation, execution and quantification of two specific experiments was performed at 3 T and described in detail.

The first experiment is an advanced version of the popular INEPT polarisation transfer sequence, especially adapted to the use with surface coils for the transfer of magnetisation from protons to adjacent, coupled carbon-13 nuclei. In this case the particular challenge was to accommodate the necessary pulses to the very restrictive timing and power limits. The calibration was done in appropriate phantom experiments and the feasibility was demonstrated also in-vivo. The sequence presented is a basis that can be extended for localisation or other manipulations of the proton magnetisation like, for example, fat suppression. This protocol can be applied to the study of the TCA-cycle or other carbon-13 enriched tracer studies.

The second experiment is to translate the phosphorus saturation transfer experiment from an initial pilot study to a robust, fast protocol for the application in larger scale, dynamic and longitudinal clinical research protocols. The main improvement was the introduction of an interleaved acquisition scheme which allows for the quasi-simultaneous acquisition of the saturation transfer experiment and the control experiment. This reduces the susceptibility to motion artifacts and speeds up the experiment which is of significant advantage in clinical studies.

The third experiment is addressing liver energy metabolism, in particular phosphorus spectroscopy and magnetisation transfer for the determination of chemical exchange. A localisation scheme combining high SNR with excellent tissue specificity. The experiment was optimised for the setup with a surface coil. The sequence timing was set based on calibration experiments, where the longitudinal relaxation times were measured, to be most robust, simple and yet yield much signal. The obtained values from a pilot study are very reasonable and the protocol is ready for its application to clinical, metabolic research.

An interesting development in scanner technology that will allow for the measurement at much higher magnetic field strengths like 7 T in the near future. This is especially interesting to multinuclear spectroscopy since a major limitation is the low sensitivity. Higher magnetic field strengths should improve the situation also by increasing the relative chemical shift range thereby alleviating the problem of spectral overlap. Phosphorus NMR should profit in a very straightforward manner from this development, even more than MRI or proton MRS where there are severe susceptibility and B_1-homogeneity issues. ^{13}C spectroscopy, especially when proton decoupling, nOe or spectral editing

with a lot of pulses are desired, will face SAR limits soon, on the other hand, simple measurement protocols like those used for glycogen without proton decoupling will gain significantly from higher static fields.

In conclusion, this work presents three experimental protocols. Each of them is suitable for a specific pathophysiological problem of human energy metabolism. This should open new possibilities for clinical researchers to gain additional information, thereby progressing the understanding of human metabolism. In consequence, an improvement in diagnosis and therapy of various disorders like insulin resistance, diabetes mellitus, non-alcoholic fatty liver disease or cardiovascular complications can be expected in the future.

Bibliography

[1] R. Bloch, W. W. Hansen, M. Packard. Nuclear Induction. *Phys Rev* 69: p. 127: 1946

[2] E. M. Haacke, R. W. Brown, M. R. Thompson, R. Vekatesan. Magnetic Resonance Imaging. Wiley-Liss: 1999

[3] J. P. Wansapura, S. K. Holland, R. S. Dunn, W. S. Ball. NMR relaxation times in the human brain at 3.0 tesla. *J Magn Reson Imaging* 9: pp. 531–538: 1999

[4] M. Krššák, V. Mlynárik, M. Meyerspeer, E. Moser, M. Roden. ^{1}H NMR relaxation times of skeletal muscle metabolites at 3 T. *Magn Reson Mater Phy* 16: pp. 155–159: 2004

[5] N. Bloembergen, E. M. Purcell, R. V. Pound. Relaxation effects in nuclear magnetic resonance absorption. *Phys Rev* 73: pp. 679–712: 1948

[6] R. A. de Graaf. In vivo NMR Spectroscopy. Wiley & Sons Ltd, West Sussex: 1998

[7] M. A. Bernstein, K. E. King, X. J. Zhou. Handbook of MRI pulse sequences. Elsevier Academic Press: 2004

[8] M. G. Kamil Ugurbil, M. R. Bendall. Amplitude- and frequency-modulated pulses to achieve 90° plane rotations with inhomogeneous B1 fields. *J Magn Reson* 72: pp. 177–185: 1987

[9] R. S. Staewen, A. J. Johnson, B. D. Ross, T. Parrish, H. Merkle, M. Garwood. 3-D FLASH imaging using a single surface coil and a new adiabatic pulse, BIR-4. *Invest Radiol* 25: pp. 559–567: 1990

[10] M. Garwood, Y. Ke. Symmetric pulses to induce arbitrary flip angles with compensation for RF inhomogeneity and resonance offsets. *J Magn Res* 94: pp. 511–525: 1991

[11] J. M. Böhlen, G. Bodenhausen. Experimental aspects of chirp NMR spectroscopy. *J Magn Reson A* 102: pp. 293–301: 1993

[12] M. S. Silver, R. I. Joseph, C. N. Chen, V. J. Sank, D. I. Hoult. Selective population inversion in NMR. *Nature* 310: pp. 681–683: 1984

[13] M. S. Silver, R. I. Joseph, D. I. Hoult. Selective spin inversion in nuclear magnetic resonance and coherent optics through an exact solution of the Bloch-Riccati equation. *Phys Rev A* 31: pp. 2753–2755: 1985

[14] K. Ugurbil, M. Garwood, A. Rath. Optimization of modulation functions to improve insensitivity of adiabatic pulses to variations in B1 magnitude. *J Magn Res* 80: pp. 448–469: 1988

[15] G. Town, D. Rosenfeld. Analytic solutions to adiabatic pulse modulation functions optimized for inhomogeneous B1 fields. *J Magn Res* 89: pp. 170–175: 1990

[16] J. Shen, J. Saunders. Analytically optimized frequency-modulation functions for adiabatic pulses. *J Magn Res* 95: pp. 356–367: 1991

[17] T. Skinner, P. Robitaille. General solutions for tailored modulation profiles in adiabatic excitation. *J Magn Res* 98: pp. 14–23: 1992

[18] B. D. Ross, G. K. Radda, D. G. Gadian, G. Rocker, M. Esiri, J. Falconer-Smith. Examination of a case of suspected McArdle's syndrome by 31P nuclear magnetic resonance. *N Engl J Med* 304: pp. 1338–1342: 1981

[19] B. Chance, S. Eleff, W. Bank, J. S. Leigh, R. Warnell. 31P NMR studies of control of mitochondrial function in phosphofructokinase-deficient human skeletal muscle. *Proc Natl Acad Sci U S A* 79: pp. 7714–7718: 1982

[20] R. H. Edwards, M. J. Dawson, D. R. Wilkie, R. E. Gordon, D. Shaw. Clinical use of nuclear magnetic resonance in the investigation of myopathy. *Lancet* 1: pp. 725–731: 1982

[21] C. T. Moonen, R. J. Dimand, K. L. Cox. The noninvasive determination of linoleic acid content of human adipose tissue by natural abundance carbon-13 nuclear magnetic resonance. *Magn Reson Med* 6: pp. 140–157: 1988

[22] R. J. Dimand, C. T. Moonen, S. C. Chu, E. M. Bradbury, G. Kurland, K. L. Cox. Adipose tissue abnormalities in cystic fibrosis: noninvasive determination of mono- and polyunsaturated fatty acids by carbon-13 topical magnetic resonance spectroscopy. *Pediatr Res* 24: pp. 243–246: 1988

[23] G. I. Shulman, D. L. Rothman, T. Jue, P. Stein, R. A. DeFronzo, R. G. Shulman. Quantitation of muscle glycogen synthesis in normal subjects and subjects with non-insulin-dependent diabetes by 13C nuclear magnetic resonance spectroscopy. *N Engl J Med* 322: pp. 223–228: 1990

[24] K. F. Petersen, D. Befroy, S. Dufour, J. Dziura, C. Ariyan, D. L. Rothman, L. DiPietro, G. W. Cline, G. I. Shulman. Mitochondrial dysfunction in the elderly: possible role in insulin resistance. *Science* 300: pp. 1140–1142: 2003

[25] J. W. Pan, J. R. Hamm, D. L. Rothman, R. G. Shulman. Intracellular pH in human skeletal muscle by 1H NMR. *Proc Natl Acad Sci U S A* 85: pp. 7836–7839: 1988

[26] P. A. Narayana, J. D. Hazle, E. F. Jackson, L. K. Fotedar, M. V. Kulkarni. In vivo 1H spectroscopic studies of human gastrocnemius muscle at 1.5 T. *Magn Reson Imaging* 6: pp. 481–485: 1988

[27] M. Bárány, P. N. Venkatasubramanian. Volume-selective water-suppressed proton spectra of human brain and muscle in vivo. *NMR Biomed* 2: pp. 7–11: 1989

[28] H. Bruhn, J. Frahm, M. L. Gyngell, K. D. Merboldt, W. Haenicke, R. Sauter. Localized proton NMR spectroscopy using stimulated echoes: application to human skeletal muscle in vivo. *Magn Res Med* 17: pp. 82–94: 1991

[29] F. A. Howe, R. J. Maxwell, D. E. Saunders, M. M. Brown, J. R. Griffiths. Proton spectroscopy in vivo. *Magn Reson Q* 9: pp. 31–59: 1993

[30] F. Schick, B. Eismann, W. I. Jung, H. Bongers, M. Bunse, O. Lutz. Comparison of localized proton NMR signals of skeletal muscle and fat tissue in vivo: two lipid compartments in muscle tissue. *Magn Reson Med* 29: pp. 158–167: 1993

[31] C. Boesch, J. Slotboom, H. Hoppeler, R. Kreis. In vivo determination of intramyocellular lipids in human muscle by means of localized 1H-MR-spectroscopy. *Magn Reson Med* 37: pp. 484–493: 1997

[32] J. W. Pan, J. R. Hamm, H. P. Hetherington, D. Rothman, R. Shulman. Correlation of lactate and pH in human skeletal muscle after exercise by ^{1}H NMR. *Magn Reson Med* 20: pp. 57–65: 1991

[33] L. Jouvensal, P. G. Carlier, G. Bloch. Practical implementation of single-voxel double-quantum editing on a whole-body NMR spectrometer: localized monitoring of lactate in the human leg during and after exercise. *Magn Reson Med* 36: pp. 487–490: 1996

[34] C. Brillault-Salvat, E. Giacomini, C. Wary, J. Peynsaert, L. Jouvensal, G. Bloch, P. G. Carlier. An interleaved heteronuclear NMRI-NMRS approach to non-invasive investigation of exercising human skeletal muscle. *Cell Mol Biol (Noisy-le-grand)* 43: pp. 751–762: 1997

[35] Z. Y. Wang, E. A. Noyszewski, J. S. Leigh. In vivo MRS measurement of deoxymyoglobin in human forearms. *Magn Reson Med* 14: pp. 562–567: 1990

[36] C. Brillault-Salvat, E. Giacomini, L. Jouvensal, C. Wary, G. Bloch, P. G. Carlier. Simultaneous determination of muscle perfusion and oxygenation by interleaved NMR plethysmography and deoxymyoglobin spectroscopy. *NMR Biomed* 10: pp. 315–323: 1997

[37] E. A. Noyszewski, E. L. Chen, R. Reddy, Z. Wang, J. S. Leigh. A simplified sequence for observing deoxymyoglobin signals in vivo: myoglobin excitation with dynamic unexcitation and saturation of water and fat (MEDUSA). *Magn Reson Med* 38: pp. 788–792: 1997

[38] P. A. Molé, Y. Chung, T. K. Tran, N. Sailasuta, R. Hurd, T. Jue. Myoglobin desaturation with exercise intensity in human gastrocnemius muscle. *Am J Physiol* 277: pp. 173–180: 1999

[39] R. Kreis, K. Bruegger, C. Skjelsvik, S. Zwicky, M. Ith, B. Jung, I. Baumgartner, C. Boesch. Quantitative (1)H magnetic resonance spectroscopy of myoglobin de- and reoxygenation in skeletal muscle: reproducibility and effects of location and disease. *Magn Reson Med* 46: pp. 240–248: 2001

[40] I. Baumgartner, H. C. Thoeny, O. Kummer, C. Roefke, C. Skjelsvik, C. Boesch, R. Kreis. Leg ischemia: assessment with MR angiography and spectroscopy. *Radiology* 234: pp. 833–841: 2005

[41] M. Krššák, K. Falk Petersen, A. Dresner, L. DiPietro, S. M. Vogel, D. L. Rothman, M. Roden, G. I. Shulman. Intramyocellular lipid concentrations are correlated with insulin sensitivity in humans: a 1H NMR spectroscopy study. *Diabetologia* 42: pp. 113–116: 1999

[42] G. Perseghin, P. Scifo, F. De Cobelli, E. Pagliato, A. Battezzati, C. Arcelloni, A. Vanzulli, G. Testolin, G. Pozza, A. Del Maschio, L. Luzi. Intramyocellular triglyceride content is a determinant of in vivo insulin resistance in humans: a 1H-13C nuclear magnetic resonance spectroscopy assessment in offspring of type 2 diabetic parents. *Diabetes* 48: pp. 1600–1606: 1999

[43] S. Jacob, J. Machann, K. Rett, K. Brechtel, A. Volk, W. Renn, E. Maerker, S. Matthaei, F. Schick, C. D. Claussen, H. U. Häring. Association of increased intramyocellular lipid content with insulin resistance in lean nondiabetic offspring of type 2 diabetic subjects. *Diabetes* 48: pp. 1113–1119: 1999

[44] B. H. Goodpaster, J. He, S. Watkins, D. E. Kelley. Skeletal muscle lipid content and insulin resistance: evidence for a paradox in endurance-trained athletes. *J Clin Endocrinol Metab* 86: pp. 5755–5761: 2001

[45] C. Thamer, J. Machann, O. Bachmann, M. Haap, D. Dahl, B. Wietek, O. Tschritter, A. Niess, K. Brechtel, A. Fritsche, C. Claussen, S. Jacob, F. Schick, H. U. Häring, M. Stumvoll. Intramyocellular lipids: anthropometric determinants and relationships with maximal aerobic capacity and insulin sensitivity. *J Clin Endocrinol Metab* 88: pp. 1785–1791: 2003

[46] C. S. Stump, K. R. Short, M. L. Bigelow, J. M. Schimke, K. S. Nair. Effect of insulin on human skeletal muscle mitochondrial ATP production, protein synthesis, and mRNA transcripts. *Proc Natl Acad Sci U S A* 100: pp. 7996–8001: 2003

[47] V. B. Ritov, E. V. Menshikova, J. He, R. E. Ferrell, B. H. Goodpaster, D. E. Kelley. Deficiency of subsarcolemmal mitochondria in obesity and type 2 diabetes. *Diabetes* 54: pp. 8–14: 2005

[48] P. Angulo. Nonalcoholic fatty liver disease. *N Engl J Med* 346: pp. 1221–1231: 2002

[49] M. Roden. Mechanisms of Disease: hepatic steatosis in type 2 diabetes–pathogenesis and clinical relevance. *Nat Clin Pract Endocrinol Metab* 2: pp. 335–348: 2006

[50] M. Krššák, A. Brehm, E. Bernroider, C. Anderwald, P. Nowotny, C. Dalla Man, C. Cobelli, G. W. Cline, G. I. Shulman, W. Waldhäusl, M. Roden. Alterations in postprandial hepatic glycogen metabolism in type 2 diabetes. *Diabetes* 53: pp. 3048–3056: 2004

[51] B. B. Lowell, G. I. Shulman. Mitochondrial dysfunction and type 2 diabetes. *Science* 307: pp. 384–387: 2005

[52] M. A. Lazar. The humoral side of insulin resistance. *Nat Med* 12: pp. 43–44: 2006

[53] R. Oberhaensli, B. Rajagopalan, G. J. Galloway, D. J. Taylor, G. K. Radda. Study of human liver disease with P-31 magnetic resonance spectroscopy. *Gut* 31: pp. 463–467: 1990

[54] K. K. Changani, R. Jalan, I. J. Cox, M. Ala-Korpela, K. Bhakoo, S. D. Taylor-Robinson, J. D. Bell. Evidence for altered hepatic gluconeogenesis in patients with cirrhosis using in vivo 31-phosphorus magnetic resonance spectroscopy. *Gut* 49: pp. 557–564: 2001

[55] S. D. Taylor-Robinson, E. L. Thomas, J. Sargentoni, C. D. Marcus, B. R. Davidson, J. D. Bell. Cirrhosis of the human liver: an in vitro 31P nuclear magnetic resonance study. *Biochim Biophys Acta* 1272: pp. 113–118: 1995

[56] S. D. Taylor-Robinson, J. Sargentoni, J. D. Bell, N. Saeed, K. K. Changani, B. R. Davidson, K. Rolles, A. K. Burroughs, H. J. Hodgson, C. S. Foster, I. J. Cox. In vivo and in vitro hepatic 31P magnetic resonance spectroscopy and electron microscopy of the cirrhotic liver. *Liver* 17: pp. 198–209: 1997

[57] D. K. Menon, M. Harris, J. Sargentoni, S. D. Taylor-Robinson, I. J. Cox, M. Y. Morgan. In vivo hepatic 31P magnetic resonance spectroscopy in chronic alcohol abusers. *Gastroenterology* 108: pp. 776–788: 1995

[58] T. Munakata, R. D. Griffiths, P. A. Martin, S. A. Jenkins, R. Shields, R. H. Edwards. An in vivo 31P MRS study of patients with liver cirrhosis: progress towards a non-invasive assessment of disease severity. *NMR Biomed* 6: pp. 168–172: 1993

[59] D. K. Menon, J. Sargentoni, S. D. Taylor-Robinson, J. D. Bell, I. J. Cox, D. J. Bryant, G. A. Coutts, K. Rolles, A. K. Burroughs, M. Y. Morgan. Effect of functional grade and etiology on in vivo hepatic phosphorus-31 magnetic resonance spectroscopy in cirrhosis: biochemical basis of spectral appearances. *Hepatology* 21: pp. 417–427: 1995

[60] S. G. Cho, M. Y. Kim, H. J. Kim, Y. S. Kim, W. Choi, S. H. Shin, K. C. Hong, Y. B. Kim, J. H. Lee, C. H. Suh. Chronic hepatitis: in vivo proton MR spectroscopic evaluation of the liver and correlation with histopathologic findings. *Radiology* 221: pp. 740–746: 2001

[61] K. Kiyono, A. Shibata, S. Sone, T. Watanabe, M. Oguchi, N. Shikama, T. Ichijo, K. Kiyosawa, T. Sodeyama. Relationship of 31P MR spectroscopy to the histopathological grading of chronic hepatitis and response to therapy. *Acta Radiol* 39: pp. 309–314: 1998

[62] H. Cortez-Pinto, J. Chatham, V. P. Chacko, C. Arnold, A. Rashid, A. M. Diehl. Alterations in liver ATP homeostasis in human nonalcoholic steatohepatitis: a pilot study. *JAMA* 282: pp. 1659–1664: 1999

[63] S. Nair, V. P Chacko, C. Arnold, A. M. Diehl. Hepatic ATP reserve and efficiency of replenishing: comparison between obese and nonobese normal individuals. *Am J Gastroenterol* 98: pp. 466–470: 2003

[64] S. F. Solga, A. Horska, J. M. Clark, A. M. Diehl. Hepatic 31P magnetic resonance spectroscopy: a hepatologist's user guide. *Liver Int* 25: pp. 490–500: 2005

[65] A. W. Overhauser. Polarization of nuclei in metals. *Phys Rev* 92: pp. 411–415: 1953

[66] K. F. Petersen, S. Dufour, D. Befroy, R. Garcia, G. I. Shulman. Impaired mitochondrial activity in the insulin-resistant offspring of patients with type 2 diabetes. *N Engl J Med* 350: pp. 664–671: 2004

[67] A. Brehm, M. Krššák, A. I. Schmid, P. Nowotny, W. Waldhäusl, M. Roden. Increased lipid availability impairs insulin-stimulated ATP synthesis in human skeletal muscle. *Diabetes* 55: pp. 136–140: 2006

[68] J. Szendroedi, A. I. Schmid, M. Chmelik, C. Toth, A. Brehm, M. Krššák, P. Nowotny, M. Wolzt, W. Waldhäusl, M. Roden. Muscle mitochondrial ATP synthesis and glucose transport/phosphorylation in type 2 diabetes. *PLoS Med* 4: 2007

[69] R. D. Oberhaensli, G. J. Galloway, D. J. Taylor, P. J. Bore, G. K. Radda. Assessment of human liver metabolism by phosphorus-31 magnetic resonance spectroscopy. *Br J Radiol* 59: pp. 695–699: 1986

[70] P. A. Mayes. Intermediary metabolism of fructose. *Am J Clin Nutr* 58: pp. –765: 1993

[71] C. Boesch, C. Elsing, H. Wegmüller, J. Felblinger, P. Vock, J. Reichen. Effect of ethanol and fructose on liver metabolism: a dynamic 31Phosphorus magnetic resonance spectroscopy study in normal volunteers. *Magn Reson Imaging* 15: pp. 1067–1077: 1997

[72] P. C. Dagnelie, D. K. Menon, I. J. Cox, J. D. Bell, J. Sargentoni, G. A. Coutts, J. Urenjak, R. A. Iles. Effect of L-alanine infusion on 31P nuclear magnetic resonance spectra of normal human liver: towards biochemical pathology in vivo. *Clin Sci (Lond)* 83: pp. 183–190: 1992

[73] W. Thoma, K. Ugurbil. Saturation-transfer studies of ATP-Pi exchange in isolated perfused rat liver. *Biochim Biophys Acta* 893: pp. 225–231: 1987

[74] A. I. Schmid, M. Chmelik, J. Szendroedi, M. Krššák, A. Brehm, E. Moser, M. Roden. Quantitative ATP Synthesis in Human Liver Measured by Localized ^{31}P Spectroscopy Employing the Magnetization Transfer Experiment. *NMR Biomed* (in press): 2007

[75] P. A. Bottomley. Selective volume method for performing localized NMR spectroscopy. U.S. patent 4 480 228: 1984

[76] J. Frahm, K. D. Merboldt, W. Hänicke. Localized proton NMR spectroscopy using stimulated echoes. *J Magn Res* 72: pp. 502–508: 1987

[77] J. Ordidge, A. Connelly, J. Lobman. Image-selected in vivo spectroscopy (ISIS). A new technique for spatially selective NMR spectroscopy. *J Magn Res* 66: pp. 283–294: 1986

[78] T. R. Brown, B. M. Kincaid, K. Ugurbil. NMR chemical shift imaging in three dimensions. *Proc Natl Acad Sci U S A* 79: pp. 3523–3526: 1982

[79] S. Posse, S. R. Dager, T. L. Richards, C. Yuan, R. Ogg, A. A. Artru, H. W. Müller-Gärtner, C. Hayes. In vivo measurement of regional brain metabolic response to hyperventilation using magnetic resonance: proton echo planar spectroscopic imaging (PEPSI). *Magn Reson Med* 37: pp. 858–865: 1997

[80] R. Freeman, E. Kupče. Decoupling: theory and practice. I. Current methods and recent concepts. *NMR Biomed* 10: pp. 372–380: 1997

[81] A. H. Wilman, P. S. Allen. An analytical and experimental evaluation of STEAM versus PRESS for the observation of the lactate doublet. *JMR B* 101: pp. 102–105: 1993

[82] R. B. Thompson, P. S. Allen. Response of metabolites with coupled spins to the STEAM sequence. *Magn Reson Med* 45: pp. 955–965: 2001

[83] H. Kim, R. B. Thompson, C. C. Hanstock, P. S. Allen. Variability of metabolite yield using STEAM or PRESS sequences in vivo at 3.0 T, illustrated with myo-inositol. *Magn Reson Med* 53: pp. 760–769: 2005

[84] W. A. Anderson, R. Freeman. Influence of a second radiofrequency field on high-resoution nuclear magnetic resoance spectra. *J Chem Phys* 37: pp. 85–103: 1962

[85] W. A. Anderson, F. A. Nelson. Removal of residual splitting in nuclear magnetic double resonances. *J Chem Phys* 39: pp. 183–189: 1963

[86] J. B. Grutzner, R. E. Santini. Coherent broad-band decoupling – an alternative to proton noise decoupling in carbon-13 nuclear magnetic resonance spectroscopy. *J Magn Reson* 19: pp. 173–187: 1975

[87] V. J. Basus, P. D. Ellis, H. D. W. Hill, J. S. Waugh. Utilization of chirp frequency modulation with 180° phase modulation for heteronuclear spin decoupling. *J Magn Reson* 35: pp. 19–37: 1979

[88] R. R. Ernst. Nuclear magnetic double resonance with an incoherent radiofrequency field. *J Chem Phys* 45: pp. 3845–3861: 1960

[89] R. Freeman, S. P. Kempsell, M. H. Levitt. Broadband decoupling and scaling of heteronuclear spin-spin interactions in high-resolution NMR. *J Magn Res* 35: pp. 447–450: 1979

[90] M. H. Levitt, R. Freeman. NMR population inversion using a composite pulse. *J Magn Res* 33: pp. 473–476: 1979

[91] R. Freeman, S. P. Kempsell, M. H. Levitt. Radiofrequency pulse sequences which compensate their own imperferctions. *J Magn Res* 38: pp. 453–479: 1980

[92] A. J. Shaka, J. Keeler, T. Frenkiel, F. R. An imporved sequence for broadband decoupling: WALTZ-16. *J Magn Res* 52: pp. 335–338: 1983

[93] A. J. Shaka, J. Keeler, F. R. Evaluation of a new broadband decoupling sequence: WALTZ-16. *J Magn Res* 53: pp. 313–340: 1983

[94] H. Y. Carr, E. M. Percell. Effects of diffusion on free precession in nuclear magnetic resonance experiments. *Phys Rev* 94: pp. 630–638: 1954

[95] S. Meiboom, D. Gill. Modified spin-echo method for measuring nuclear relaxation times. *Rev Sci Instrum* 29: pp. 688–691: 1958

[96] M. H. Levitt, R. Freeman. Composite pulse decoupling. *J Magn Res* 43: pp. 502–507: 1981

[97] M. H. Levitt, R. Freeman, T. Frenkiel. Broadband heteronuclear decoupling. *J Magn Res* 47: pp. 328–330: 1982

[98] M. H. Levitt, R. Freeman, T. Frenkiel. Supercycles for broadband heteronucler decoupling. *J Magn Res* 50: pp. 157–160: 1982

[99] J. S. Waugh. Theory of broadband spin decoupling. *J Magn Res* 50: pp. 30–49: 1982

[100] R. Tycko, A. Pines, R. Gluckenheimer. Fixed point theory of iterative excitation schemes in NMR. *J Chem Phys* 83: pp. 2775–2802: 1985

[101] A. Allerhand, R. E. Addleman, D. Osman, M. Dohrenwend. Ultra-high res'olution NMR. III. Performance of WALTZ-16 proton decoupling. *J Magn Res* 65: pp. 361–363: 1985

[102] A. J. Shaka, T. Frenkiel, R. Freeman. NMR broadband decoupling with low radiofrequency power. *J Magn Res* 52: pp. 159–163: 1983

[103] B. M. Fung. New sequences for phase-alternated broadband decoupling. *J Magn Res* 59: pp. 424–429: 1984

[104] V. Sklenár, Z. Starčuk. Composite pulse sequences with variable performance. *J Magn Res* 62: pp. 113–122: 1985

[105] A. J. Shaka, P. B. Barker, R. Freeman. Computeroptimized decoupling scheme for wideband applications and low-level operation. *J Magn Res* 64: pp. 547–552: 1986

[106] Z. J. Starčuk, K. Bartušek, S. Z. Heteronuclear broadband spin-flip decoupling with adiabatic pulses. *JMRA* 107: pp. 24–31: 1994

[107] M. R. Bendall. Broadband and narrowband spin decoupling using adiabatic spin flips. *J Magn Reson A* 112: pp. 126–129: 1995

[108] E. Kupče, R. Freeman. Adiabatic Pulses for Wideband Inversion and Broadband Decoupling. *J Magn Res* 115A: pp. 273–276: 1995

[109] E. Kupče, R. Freeman. Stretched adiabatic pulses for broadband spin inversion. *J Magn Reson A* 117: pp. 246–256: 1995

[110] E. Kupče, R. Freeman. Optimized adiabatic pulses for wideband spin inversion. *J Magn Reson A* 118: pp. 299–303: 1996

[111] E. Kupče, R. Freeman. An adaptable broadband decoupling scheme. *Chem Phys Lett* 250: pp. 523–527: 1996

[112] I. D. Campbell, C. M. Dobson, R. J. Williams, P. E. Wright. Pulse methods for the simplification of protein NMR spectra. *FEBS Lett* 57: pp. 96–99: 1975

[113] D. L. Rothman, K. L. Behar, H. P. Hetherington, R. G. Shulman. Homonuclear 1H double-resonance difference spectroscopy of the rat brain in vivo. *Proc Natl Acad Sci U S A* 81: pp. 6330–6334: 1984

[114] D. L. Rothman, K. L. Behar, H. P. Hetherington, J. A. den Hollander, M. R. Bendall, O. A. Petroff, R. G. Shulman. 1H-Observe/13C-decouple spectroscopic measurements of lactate and glutamate in the rat brain in vivo. *Proc Natl Acad Sci U S A* 82: pp. 1633–1637: 1985

[115] G. Morris, R. Freeman. Enhancement of nuclear magnetic resonance signals by polarisation transfer. *J Am Chem Soc* 101: pp. 760–762: 1979

[116] D. M. Doddrell, D. T. Pegg, M. R. Bendall. Distortionless enhancement of NMR signals by polarization transfer. *J Magn Reson* 48: pp. 323–327: 1982

[117] M. Saner, G. McKinnon, P. Boesiger. Glycogen detection by in vivo 13C NMR: a comparison of proton decoupling and polarization transfer. *Magn Reson Med* 28: pp. 65–73: 1992

[118] R. Gruetter, G. Adriany, H. Merkle, P. M. Andersen. Broadband decoupled, 1H-localized 13C MRS of the human brain at 4 Tesla. *Magn Reson Med* 36: pp. 659–664: 1996

[119] K. E. Gates, M. Griffin, G. R. Hanson, K. Burrage. Computer simulation of magnetic resonance spectra employing homotopy. *J Magn Reson* 135: pp. 104–112: 1998

[120] H. Watanabe, Y. Ishihara, K. Okamoto, K. Oshio, T. Kanamatsu, Y. Tsukada. In vivo 3D localized 13C spectroscopy using modified INEPT and DEPT. *J Magn Reson* 134: pp. 214–222: 1998

[121] G. S. Payne, M. O. Leach. Surface-coil polarization transfer for monitoring tissue metabolism in vivo. *Magn Reson Med* 43: pp. 510–516: 2000

[122] S. Forsen, R. Hoffman. Study of moderately rapid chemical exchange reactions by means of nuclear magnetic double resonance. *J Chem Phys* 39: pp. 2892–2901: 1963

[123] T. R. Brown, K. Ugurbil, R. G. Shulman. ^{31}P Nuclear Magnetic Resonance Measurements of ATPase Kinetics in Aerobic Escherichia coli Cells. *Proc Natl Acad Sci USA* 74: pp. 5551–5553: 1977

[124] G. J. Kemp, M. Meyerspeer, E. Moser. Absolute quantification of phosphorus metabolite concentrations in human muscle in vivo by (31)P MRS: a quantitative review. *NMR Biomed* (in press): 2007. DOI: 10.1002/nbm.1192

[125] P. A. Bottomley, T. B. Foster, R. D. Darrow. Depth-resolved surface coil spectroscopy (DRESS) for in vivo 1H, 31P, and 13C NMR. *J Magn Reson* 59: p. 338: 1984

[126] S. W. Provencher. Estimation of metabolite concentrations from localized in vivo proton NMR spectra. *Magn Reson Med* 30: pp. 672–679: 1993

[127] L. Vanhamme, T. Sundin, P. V. Hecke, S. V. Huffel. MR spectroscopy quantitation: a review of time-domain methods. *NMR Biomed* 14: pp. 233–246: 2001

[128] A. Naressi, C. Couturier, J. M. Devos, M. Janssen, C. Mangeat, R. de Beer, D. Graveron-Demilly. Java-based graphical user interface for the MRUI quantitation package. *Magn Reson Mater Phy* 12: pp. 141–152: 2001

[129] L. Vanhamme, van den Boogaart A, V. H. S. Improved method for accurate and efficient quantification of MRS data with use of prior knowledge. *J Magn Reson* 129: pp. 35–43: 1997

[130] N. Ercan-Fang, M. Gannon, V. Rath, J. Treadway, M. Taylor, F. Nuttall. Integrated effects of multiple modulators on human liver glycogen phosphorylase a. *Am J Physiol Endocrinol Metab* 283: pp. 29–37: 2002

[131] M. Roden, T. B. Price, G. Perseghin, K. F. Petersen, D. L. Rothman, G. W. Cline, G. I. Shulman. Mechanism of free fatty acid-induced insulin resistance in humans. *J Clin Invest* 97: pp. 2859–2865: 1996

[132] D. E. Kelley, J. He, E. V. Menshikova, V. B. Ritov. Dysfunction of mitochondria in human skeletal muscle in type 2 diabetes. *Diabetes* 51: pp. 2944–2950: 2002

[133] V. Lebon, S. Dufour, K. F. Petersen, J. Ren, B. M. Jucker, L. A. Slezak, G. W. Cline, D. L. Rothman, G. I. Shulman. Effect of triiodothyronine on mitochondrial energy coupling in human skeletal muscle. *J Clin Invest* 108: pp. 733–737: 2001

[134] P. A. Bottomley, R. Ouwerkerk. Optimum flip-angles for exciting NMR with uncertain T_1 values. *Magn Res Med* 32: pp. 137–141: 1994

[135] J. L. Evelhoch, C. S. Ewy, B. A. Siegfried, J. J. Ackerman, D. W. Rice, R. W. Briggs. 31P spin-lattice relaxation times and resonance linewidths of rat tissue in vivo: dependence upon the static magnetic field strength. *Magn Reson Med* 2: pp. 410–417: 1985

[136] L. S. Szczepaniak, E. E. Babcock, F. Schick, R. L. Dobbins, A. Garg, D. K. Burns, J. D. McGarry, D. T. Stein. Measurement of intracellular triglyceride stores by H spectroscopy: validation in vivo. *Am J Physiol* 276: pp. 977–989: 1999

[137] H. Lei, K. Ugurbil, W. Chen. Measurement of unidirectional Pi to ATP flux in human visual cortex at 7 T by using in vivo 31P magnetic resonance spectroscopy. *Proc Natl Acad Sci U S A* 100: pp. 14409–14414: 2003

[138] L. Simonsen, R. Coker, N. A L Mulla, M. Kjaer, J. Bülow. The effect of insulin and glucagon on splanchnic oxygen consumption. *Liver* 22: pp. 459–466: 2002

[139] K. S. Park, K. J. Nam, J. W. Kim, Y. B. Lee, C. Y. Han, J. K. Jeong, H. K. Lee, Y. K. Pak. Depletion of mitochondrial DNA alters glucose metabolism in SK-Hep1 cells. *Am J Physiol Endocrinol Metab* 280: pp. 1007–1014: 2001

List of Tables

1.1. Properties of some nuclei. 17
1.2. Spin-lattice relaxation times and spin-spin relaxation times of several tissues at a field strength of 3 T. Note that T_2 is always shorter than T_1. Brain data reproduced from [3], muscle data from [4]; TMA: trimethylamonium resonance, IMCL: intramyocellular lipids, EMCL: extracellular lipids. 25

4.1. Some important acquisition (`acqp`) parameters. The names are of many parameters are different in `acqp` than they are in The pulse program. The elements column tries to describe the structure of the parameter, e.g. gives the dimension if it is an array or the elements' names in a structure. 55
4.2. ISIS addition and subtraction scheme for one, tow and three dimensional localisation. The + or - sign indicates whether a slice selecting 180 ° pulse is played out or not. The receiver phase determines whether two scans are added or subtracted. The pulse sequence can be seen in 8.7. 58

9.1. Model and starting values for the AMARES quantification of ^{31}P Muscle spectra 102
9.2. Prior knowledge used for the quantification of ^{31}P muscle spectra 102
9.3. AMARES model and results (peak area) on an exemplary human muscle dataset. The β-ATP resonance is set to 5.5 mM. The leftmost column identifies the metabolite. All lines were fitted against Gaussian model functions. The applied constraints can be seen in equal line widths and phases of several resonances. As this is a time domain fit, the amplitude is equivalent to the peak area. The phase is relative to a constant overall constant and linear phase (begin time). 102
9.4. Model and starting values for the AMARES quantification of ^{31}P human liver spectra 103
9.5. Prior knowledge used for the quantification of ^{31}P liver spectra 104
9.6. AMARES model and results (peak area) on an exemplary human liver dataset. The γ-ATP resonance is set to 2.5 mM. The left column identifies the metabolite: Phosphomono- and -diesters are fitted as two separate lines each. All lines were fitted against Gaussian model functions. The applied constraints can be seen in equal line widths and phases of several resonances. As this is a time domain fit, the amplitude is equivalent to the peak area. The phase is relative to a constant overall constant and linear phase (begin time). 104

10.1. Skeletal muscle rates of ATP synthesis. Both rates from the reaction ADP + Pi → ATP catalysed by ATP synthase and PCr + ADP → Cr + ATP catalysed by creatine kinase. The equilibrium exchange constant, the concentration of either PCr or Pi and the unidirectional exchange rates are shown. Study A shows yet unpublished data of measurements in eight healthy women who served as a control group to women with past gestrational diabetes mellitus. Study B shows values of young, healthy, lean males and females (baseline values from group CONy in [68]. 108

11.1. T_1 relaxation times [s], mean ± standard deviation. The two resonances visible for PDEs are assigned to GPC = glycero-phosphocholine and GPE = glycero-phosphoethanolamine, the resonances for PMEs to PC = phosphocholine, PE = phoshphoethanolamine, respectively. 112

12.1. The results of the saturation transfer experiments with and the hepatocellular lipid content (HCL) of nine subjects are shown. Apparent T_1^* relaxation time, the fractional signal reduction through magnetisation transfer (ΔM/M), the concentration of inorganic phosphate [Pi], the equilibrium exchange rate constant k and the ATP synthesis rate are shown for each subject. 114

List of Figures

1.1. The possible orientations of a spin $I = \frac{1}{2}$ in an external magnetic field. . 18

1.2. Torque on a magnetic moment in an external magnetic field. 19

1.3. Magnetisation in two frames of reference. The coordinates x, y, and z denote the resting frame, the primed coordinates denote the moving frame. 22

1.4. Axis of precession in the rotating frame. 23

1.5. Spin-lattice relaxation: Return of magnetisation from the xy - plane towards M_z. At the same time spin-spin relaxation takes place. This is indicated by a dephasing of the spins. The increase of M_z after the external magnetic field is applied is shown in the right panel. 24

1.6. The spins experience different local field strengths that causes the transversal magnetisation M_{xy} to decreases. The relaxation rate depends on the spin's environment, giving rise to contrast (right). 26

2.1. Magnetic field distribution of (A/D) a single-turn surface coil, (B/E) a two-turn solenoidal coil (Helmholtz coil3 and (C/F) a four-turn solenoidal coil. for the coils in (B) and (C), the winding separation equals half the diameter. The B_1 distribution of (A-C) corresponds to the sensitivity following homogeneous (i.e. B_1 insensitive) excitation, for instance with adiabatic RF pulses. (D-F) show the sensitivity profiles of the coils following a 9O° excitation with a conventional square RF pulse. The B_1 dependence of the nutation angle significantly reduces the sensitive volumes of the coils. Reproduced from [6]. 30

2.2. Amplitude (left) and excitation profile (right) of a 2 ms three-lobe sinc pulse. The basic frequency was 125.7 MHz. 30

2.3. The relationship between the applied B_1 field with amplitude $A(t)$ and frequency $\omega_{RF}(t)$ modulations, the effective magnetic field $\boldsymbol{B}_{eff}$, and the magnetisation $\boldsymbol{M}$ in the rotating reference frame. The magnetisation vector precesses about the effective field and traces a cone, as indicated by the dotted path. Reproduced from [7] 32

2.4. (a-c) The adiabatic excitation process and (d-f) the non-adiabatic excitation process. The figures in each row show the magnetisation vector $\boldsymbol{M}$, the effective magnetic field $\boldsymbol{B}_{eff}$, and the applied RF field $\boldsymbol{B}_1$ throughout the course of an excitation pulse. (a) Beginning of an adiabatic pulse; (b) during the adiabatic pulse, showing the magnetisation precessing in a tight cone about the effective field; and (c) the end of the adiabatic pulse. (d) Beginning of a non-adiabatic pulse, (e) during the non-adiabatic pulse (assuming the spins are on-resonance), and (f) the end of the non-adiabatic pulse. Reproduced from [7]. 34

2.5. The inversion processes in (a-e) an adiabatic pulse and (f) a non-adiabatic pulse. (a) Beginning of the adiabatic inversion pulse; (b) during the first half of the adiabatic pulse, showing the magnetisation precessing in a tight cone about the effective field (the size of the cone is exaggerated for better visualisation); (c) at the mid-point of the adiabatic pulse; (d) during the second half of the adiabatic pulse; (e) at the end of the adiabatic pulse. (f) The trajectory of the magnetisation $\boldsymbol{M}$ of non-adiabatic pulse. Note that for adiabatic inversion, the magnetisation vector $\boldsymbol{M}$ is approximately parallel to the effective field $\boldsymbol{B}_{eff}$ during the pulse, whereas for non-adiabatic inversion $\boldsymbol{M}$ is perpendicular to the applied $\boldsymbol{B}_1$ field. Reproduced from [7] 35

2.6. Amplitude (top), phase (middle) and frequency modulation (bottom) of a BIR-4 pulse. Reproduced from [6] 36

2.7. Description of a BIR-1 pulse. (A-B) Normalised RF amplitude and frequency modulation of the pulse. (C-F) The effective field $\boldsymbol{B}_{eff} = \boldsymbol{B}_e$ starts along the $\boldsymbol{x}$ axis and rotates towards the $\boldsymbol{z}$ axis. At the midpoint of the pulse it is flipped instantaneously to the $-z$ axis from which it rotates to the $\boldsymbol{y}$ axis because it is 90° phase shifted to achieve excitation. $\boldsymbol{M}_x$ is initially parallel to the $\boldsymbol{B}_{eff}$ field and precesses about it in a tight cone throughout the pulse. Halfway through the pulse $\boldsymbol{M}_y$ and $\boldsymbol{M}_z$ are dephased by an angle β during the first segment. The $\boldsymbol{B}_{eff}$ inversion causes $\boldsymbol{M}_y$ and $\boldsymbol{M}_z$ to acquire a rotation $-\beta$ during the second half of the pulse, thereby eliminating the phase dispersion. Reproduced from [6]. 37

2.8. BIR-4 pulse rotation. $\boldsymbol{B}_{eff} = \boldsymbol{B}_e$ starts in the $\boldsymbol{x}$ axis (A), rotates towards the longitudinal axis (B), is inverted along with a phase shift $\Delta\Phi_1$) (C), rotates back to the positive $\boldsymbol{z}$ axis, (D-E), is inverted again (F) with a phase shift $\Delta\Phi_2$ and rotates finally back to the $\boldsymbol{x}$ axis. The sum of the angles $\Delta\Phi_i$ determine the nutation angle of the magnetisation. Reproduced from [6]. 38

3.1. Schematic and simplified description of cellular energy metabolism of a muscle cell. The cellular compartmentation between the cytosol (green) and mitochondria (pink) is of great importance to the reactions. Substrates in the form of fatty acids or glucose enter the cell or are released from intracellular stores (IMCL or glycogen). Fatty acids are cut into C-2 pieces by β-oxidation in the mitochondria which enter the TCA-cycle in the form of Acetyl-CoA. Glucose is phosphorilated and broken down into pyruvate which enters the mitochondria and the TCA-cycle. Several processes in the citric-acid cycle produce free protons which are transferred to the inter-membrane space of the mitochondria. These protons are used by ATP synthase to form ATP from ADP and inorganic phosphate in exchange for transporting protons back into the mitochondria. The colours indicate the accessibility by in-vivo NMR spectroscopy: by ^{1}H MRS in red, ^{31}P in magenta and ^{13}C in blue. Coloured text indicates that the metabolite is visible in the spectra. Coloured arrows indicate that the respective flux is measurable. 44

3.2. Water suppressed proton spectra acquired at 3 T. A $(12\,\mathrm{cm})^3$ volume of interest was selected by a STEAM sequence ($T_E = 20\,\mathrm{ms}$, $T_M = 30\,\mathrm{ms}$, $T_R = 4\,\mathrm{s}$. Left: Spectrum from soleus muscle, 32 averages; right: Spectrum from tibialis anterior muscle. 64 averages. The shift of the EMCL peak is more pronounced in tibialis anterior than in soleus. 45

3.3. Liver spectrum of two diabetic subjects, one with low (left) and one with high (right) HCL content. 46

4.1. The NMR scanner where all measurements for this work were performed. 51

4.2. Point resolved spectroscopy pulse sequence [75]. In a PRESS experiment the signal of the second spin echo is acquired. The excitation pulse and the two refocusing pulses are slice selective with the slices orthogonal to each other. Thus, the signal which is refocused at the top of the second echo comes from the cuboidal intersection of the three slices. The two echo times need not be equal. For coupled spin systems a proper selection of the timing greatly influences the observed signal. The figure is reproduced with friendly permission from Martin Meyerspeer. 56

4.3. Stimulated echo acquisition mode pulse sequence. The figure is reproduced with friendly permission from the thesis of Martin Meyerspeer. . . 57

5.1. Natural abundance, proton decoupled, ^{13}C spectrum from human calf muscle acquired at 3 T. Besides the predominant peaks of fatty acids (FA) and glycerol, resonances arising from creatine (Cr) and glycogen are visible. 61

5.2. Natural abundance ^{13}C spectrum of the human liver. The most prominent signals arise from fatty acids (FA) and glycerol. There is visible also a doublet resonance of a reference solution containing ^{13}C-enriched formic acid (FoA). One of the signals overlaps with the carboxyl peak of fatty acids at about 172 ppm and the other is visible at about 165 ppm. 62
5.3. Glycogen C-1 resonance at 100.5 ppm; the label appears with time when the tracer is incorporated into newly formed muscle glycogen. Reproduced from [23]. 63
5.4. Weakly coupled spins; left: the resonance frequency of both nuclei I and S are splitted symmetrically with a distance J. Right: corresponding energy levels. Reproduced from [80]. 64

6.1. Magnetisation trajectories of the I spins calculated for two consecutive composite pulses R_2R_2, where $R_2 = 90\,^\circ_{\boldsymbol{x}}270\,^\circ_{\boldsymbol{y}}90\,^\circ_{\boldsymbol{x}}$. The family of four trajectories represents resonance offsets near $\Delta B/B_2 = 0.3$, where $\Delta\omega = \gamma\Delta B/2\pi$. Note that all trajectories terminate very close to the $+\boldsymbol{z}$ axis in spite of the appreciable tilt of the effective fields ($\sim$17 °). If this sequence is followed by the phase-inverted pair of pulses $\bar{R}_2\bar{R}_2$, the vectors are carried to a point much closer to the $+\boldsymbol{z}$ axis, and the overall effect is almost a perfect cycle. Reproduced from [80] 68
6.2. Magnetisation trajectories for adiabatic rapid passage when the effective radiofrequency field $\boldsymbol{B}_{eff}$ starts at an inclination with respect to the $+\boldsymbol{z}$ axis (exaggerated for the purpose of illustration). (a) For good adiabaticity ($\eta = 10$) the path is a cycloid. (b) When the adiabatic condition begins to be violated ($\eta = 3$), the effective field moves too fast to allow a complete revolution of the magnetisation vector about $\boldsymbol{B}_{eff}$ when $\boldsymbol{B}_{eff}$ has its minimum value B_2 at resonance. (c) For a gross violation of the adiabatic condition ($\eta = 1$) the trajectory makes wild excursions and never reaches the $-z$ axis. Reproduced from [80] 71
6.3. The shape of the WURST pulse. Three different amplitude modulations for different values of the parameter n=3, 10, 20 are plotted. With increasing n, the plateau extends over a greater part of the pulse. 71
6.4. Experimental offset dependence of WURST decoupling of ^{13}C while observing the protons in ^{13}C enriched sodium formate ($J = 200$ Hz). (a) $\gamma B_2(rms)/2\pi = 8.5$ kHz. (b) $\gamma B_2(rms)/2\pi = 10.5$ kHz. (c) $\gamma B_2(rms)/2\pi = 12.2$ kHz. (d) $\gamma B_2(rms)/2\pi = 14.3$ kHz. The variations in the intensity of the decoupled line are attributed mainly to limitations of the radiofrequency circuitry over these very wide frequency bands. Reproduced from [80]. 72

7.1. Spin-echo of coupled and uncoupled spins 73
7.2. POCE sequence. The ^{13}C pulse is turned on and off and the two experiments are subtracted. $\tau = 1/2J$. This leaves only signals from protons J-coupled to ^{13}C nuclei. 75

7.3. Refocused INEPT sequence. $\tau_1 = 1/4J$. After the two simultaneous 90 ° pulses the basic INEPT sequence is completed. The magnetisation, however, is in an anti-phase state. Therefore, the acquisition is delayed to let the anti-phase coherences evolve into an in-phase state to permit proton decoupling. The two 90 ° pulses refocus $\boldsymbol{B}_0$ inhomogeneities and chemical shift. For CH, CH_2 and CH_3 spin systems the optimum values for the delay τ_2 are different. If a simultaneous detection of different spin systems is required, the timing is not optimal. 76

7.4. The basic DEPT sequence. For a detailed description of the evolution of the magnetisation refer to the text or the legend Figure 7.5. 78

7.5. Non-classical vector diagrams of the DEPT experiment for a two-spin system IS with one proton coupled to ^{13}C. After the first ^{1}H pulse the in-phase ^{1}H vector is converted to an anti-phase coherence due to scalar coupling between ^{13}C and ^{1}HȦ 90 ° pulse on ^{13}C on the $\boldsymbol{x}$ axis generates the desired multiple quantum state. This coherence is frozen until the last ^{1}H pulse with a flip angle Θ is applied. Then the multiple quantum coherence is partially converted into an anti-phase state, which finally evolves into the observable in-phase magnetisation. The delay τ is set to $1/2J$.to maximise the magnitude of the anti-phase and multiple quantum vectors. The two 180 ° pulses will refocus chemical shifts and are not included in the diagram. Reproduced from http://www.biophysics.org/education/ . . 79

7.6. Adiabatic refocused INEPT. The simultaneous applied segmented BIR-4 pulse produce the polarisation transfer in the time $\tau_1 = 1/2J$. After τ_1 they produce the same coherences as the pulses of the basic INEPT sequence. The 180 ° BIR-4 pulses refocus chemical shift evolution and B_0inhomogeneities while the anti-phase coherences evolve into magnetisation during τ_2. 81

7.7. Calibration experiment on a phantom of aqueous solution of glutamine. The echo time $T_{\mathrm{E},2}$ of the fully adiabatic refocused INEPT sequence is varied to experimentally optimise the sequence timing for both CH (C-2 position) and CH_2 (C-3 and C-4 positions) functional groups. The signal intensity is plotted as a function of $T_{\mathrm{E},2}$, 3.4 ms-16.2 ms, 0.2 ¿ms steps. . . 83

7.8. Comparing ^{13}C spectra of human calf muscle. INEPT (bottom), nOe enhanced pulse-acquire (top), 256 accumulations in 8.5 min each. The timing was set to simultaneously detect CH and CH_2 groups. 84

8.1. Axial gradient echo images of lower leg acquired with the surface coil which is also used for the ^{31}P measurements. The images are acquired in 3 min with a field of view of 20 cm and 256 x 256 matrix size. $T_R = 0.34$ s, $T_E = 17$ ms. 89

8.2. ^{31}P spectrum of human calf muscle acquired at 3 T in 8.5 min. 90

8.3. Pulse program of the saturation transfer experiments. The signals are acquired in an interleaved manner. 91

8.4. Pulse program of the T_1 measurements. The program iterates over different inversion times. Averaging can be done inside and outside the loop. . 92
8.5. Axial liver images acquired within one breath-hold (left). Oblique liver images, in a plane perpendicular to the axial plane, acquired within one breath-hold (right). Acquisition parameters: Five slices, $T_E = 15\,\text{ms}$, $T_R = 130\,\text{ms}$, FOV=25 cm, 128 x 128 matrix size. 94
8.6. Liver image schematically showing the coil placement. The 30 mm slab, which is the volume of interest, is indicated by the two parallel lines. . . 95
8.7. Pulse program of the 1D-ISIS sequence. 96
8.8. Pulse program of the saturation transfer experiments. The signals are acquired in an interleaved manner. 97
8.9. Pulse program of the T_1 measurements. The program iterates over different inversion times. Averaging can be done inside and outside the loop. . 98
8.10. ^{31}P spectrum acquired in 8.5 min (64 averages, T_R=8 s), localised with 1D-ISIS and a 10 cm diameter surface coil at 3 T. The contamination from muscle tissue, visible by the residual PCr signal is very small. Considering that this is the predominant signal in muscle ^{31}P spectra, being one order of magnitude bigger than the other resonances, the effect of residual muscle signal on the other metabolites is negligible (<5 %). 100

9.1. Example of the AMARES quantification (see also Table 9.6). From bottom to top: Original dataset; fit result; individual model components (1 Pi, 2,3 PDE, 4,5 PME, 6,7,8 ATP, 9 NADPH, 10 UDPG); residual spectrum. 105

10.1. ^{31}P spectra obtained from calf muscle during the saturation transfer experiment (2 x 16 averages, 8.5 min); Top: Spectrum where the saturation frequency was mirrored about the resonance of inorganic phosphate (Pi) with Pi and all three ATP resonances. Middle: Spectrum with selective saturation of γ-ATP which is therefore absent. Bottom: The difference spectrum. Small Frame: The area of the ΔPi signal of the difference spectrum is displayed magnified. 107

12.1. ^{31}P spectra obtained from human liver during the saturation transfer experiment (2 x 1024 averages, 68 min); Top: Spectrum where the saturation frequency was mirrored about the resonance of inorganic phosphate (Pi) with Pi and all three ATP resonances. Middle: Spectrum with selective saturation of γ-ATP which is therefore absent. Bottom: The difference spectrum. Small Frame: The area of the ΔPi signal of the difference spectrum is displayed magnified ($\times \sim 5$). 114

13. Danksagung

An dieser Stelle möchte ich einigen Personen danken, ohne deren Unterstützung diese Arbeit nicht in dieser Form möglich gewesen wäre. Zuallererst möchte ich Prof. Ewald Moser und Prof. Gerald Badurek dafür danken, die Betreuung und Beurteilung der Arbeit übernommen zu haben.

Nicht weniger Dank gebührt Martin Krššák, auf dessen Erfahrung ich aufbauen konnte und der stets unterstützend zur Verfügung stand und vor allem auch dafür, dass er sich die Mühe gemacht hat, diese Arbeit mit kritischem Auge zu lesen und mir dadurch sehr geholfen hat, diese Arbeit zu verbessern.

Des Weiteren gebührt Prof. Michael Roden Dank, der sowohl für mein finanziellles Auskommen während der Arbeit an dieser Dissertation gesorgt hat als auch für genügend Fragestellungen, die die Motivation für die hier entwickelten und beschriebenen Experimente lieferten.

Insbesondere gilt mein Dank auch meinen lieben Kollegen von der Klink für Innere Medizin III und dem Karl-Landsteiner Institut, insbesondere Attila Brehm, Julia Szendrödi und Michaela Kacerovsky. Ohne die gute Zusammenarbeit mit ihnen wären all die erfolgreichen Studien und Experimente nie möglich gewesen.

Auf keinen Fall möchte ich die herzliche, persönliche Atmosphäre im "Holzhaus" nicht unerwähnt lassen, die es ermöglicht, dass ein fruchtbarer Gedankenaustausch mit den Kollegen stattgefunden hat. Da ich sicher jemanden unerwähnt ließe, will ich hier keine Namen nennen. Aber eines steht sicher fest: Es sind einige über das berufliche hinausgehende Freundschaften bei der einen oder anderen gemeinsamen Tasse Tee oder Kaffee entstanden.

Es ist mir ein Anliegen, mich bei Martin Meyerspeer und vor allem Alex Rauscher zu bedanken, durch die ich erstmals mit der NMR-Arbreitsgruppe in Kontakt gekommen bin.

Meiner Familie und meinen Freunden sei dafür gedankt, dass sie mich während dieser Jahre begleitet haben.

Als letzter und wichtigster Person will ich Lisa Farthofer danken, dafür, dass sie, obwohl sie einen ganz anderen beruflichen Hintergrund hat, sich die Mühe gemacht hat, meine Dissertation gelesen und viele gute Anregungen in diese Arbeit eingebracht hat. Aber ein viel größerer Beitrag ist ihre Liebe und Zuneigung, die mir sehr viel Kraft gegeben hat. Vor allem dafür möchte ich ihr danken.

14. Lebenslauf

Persönliche Daten

Name:	Albrecht Ingo Schmid
geboren am:	13. April 1975 in Wien
Familienstand:	ledig
Bundesheer:	vom Wehrdienst befreit
Wohnsitz:	Paletzgasse 22-24/35, 1160 Wien

Ausbildung

Sep. 1981 – Juni 1989	Volks- und Hauptschule Zinckgasse, 1150 Wien
Sep. 1989 – Juni 1993	Realgymnasium Wenzgasse, 1130 Wien, mit Matura abgeschlossen
Okt. 1993 – Juni 2001	Studium der Technischen Physik an der TU Wien
Okt. 1999 – Juli 2000	Studienaufenthalt in Lissabon, Portugal, am Instituto Superior Técnico der Universidade Técnica de Lisboa
Diplomarbeit	"Colour String Percolation in High Energy Nuclear Collisions", durchgeführt am Atominstitut der österreichischen Universitäten bei Prof. Faber; die Arbeit basiert auf dem in Lissabon durchgeführten Projekt.
Seit April 2003	Dissertation in Medizinischer Physik: "Methods of Multi Nuclear Magnetic Resonance Spectroscopy for Metabolic Research" an der Technischen Universität Wien am Atominstitut der Österreichischen Universitäten in Zusammenarbeit mit dem MR Center of Excellence, Medizinische Universität Wien.

Beruf

Jänner 2002 – März 2003	angestellt bei Mobilkom Austria als Datenbankadministrator.
April 2003 – März 2006	angestellt als wissenschaftlicher Mitarbeiter an der Klinik für Innere Medizin III, Medizinische Universität Wien.
Seit April 2006	angestellt als wissenschaftlicher Mitarbeiter am Karl-Landsteiner Institut für Endokrinologie und Stoffwechsel.

Fremdsprachen

Englisch	verhandlungssicher
Portugiesisch	fließend
Spanisch	fließend

Nov. 2004	"Dynamic and functional MRS" Vortrag und praktsiche Demonstrationen im Rahmen des Graduiertenlehrgangs der Europäischen Diabetesgesellschaft.

Publikationen

A. Brehm, M. Krššák, A. I. Schmid, P. Nowotny, W. Waldäusl, M. Roden. Increased lipid availability impairs insulin-stimulated ATP synthesis in human skeletal muscle. Diabetes 55: pp. 136–140: 2006

J. Szendroedi, A. I. Schmid, M. Chmelik, C. Toth, A. Brehm, M. Krššák, P. Nowotny, M. Wolzt, W. Waldhäusl, M. Roden. Muscle mitochondrial ATP synthesis and glucose transport/phosphorylation in type 2 diabetes. PLoS Med 4: 2007

A. I. Schmid, M. Chmelik, J. Szendroedi, M. Krššák, A. Brehm, E. Moser, M. Roden. Quantitative ATP Synthesis in Human Liver Measured by Localized ^{31}PSpectroscopy Employing the Magnetization Transfer Experiment. NMR Biomed (in press): 2007

Konferenzbeiträge

"Localised ^{13}C Spectroscopy in Humans with Outer Volume Saturation", Poster bei der 14. Jahrestagung der ISMRM, Kyoto, Japan, Mai 2004

"T_1 Relaxation Times of ^{31}P Hepatic Metabolites at 3 T", Poster bei der 21. Jahrestagung der ESMRMB, Kopenhagen, Dänemark. September 2004

"Fully Adiabatic INEPT for ^{1}H/^{13}C MRS in Humans", Poster bei der 46. ENC, Providence, Rhode Island, USA. April 2005

"Hepatic ATP Synthesis Rates in Healthy Humans", Poster bei der 16. Jahrestagung der ISMRM, Seattle, Washington, USA. Mai 2006

"Patients with acromegaly exhibit altered mitochondrial function despite successful treatment", Poster bei der gemeinsamen Jahrestagung der ISMRM und der ESMRMB, Berlin, Deutschland. Mai 2007